ANGLE-RESOLVED PHOTOEMISSION SPECTROSCOPIC PROPERTIES OF QUASI-ONE-DIMENSIONAL CRYSTALS

THÈSE N^{O} 3107 (2004)

PRÉSENTÉE À LA FACULTÉ SCIENCES DE BASE

Institut de physique de la matière complexe

SECTION DE PHYSIQUE

ÉCOLE POLYTECHNIQUE FÉDÉRALE DE LAUSANNE

POUR L'OBTENTION DU GRADE DE DOCTEUR ÈS SCIENCES

PAR

Slobodan MITROVIC

Physicien diplômé de l'Université de Zagreb, Croatie
et de nationalité croate

acceptée sur proposition du jury:

Prof. G. Margaritondo, directeur de thèse
Prof. L. Forro, rapporteur
Dr P. Perfetti, rapporteur
Prof. P. Soukiassian, rapporteur

Lausanne, EPFL
2004

Tatjani i Sretenu

Acknowledgments

I am indebted to many great people that have worked with me, given me support and help along the way.

I have profited greatly from the support of group colleagues that have become my dear friends notably L. Perfetti, A. Reginelli, C. Rojas and C. Søndergaard.

It was a privilege to work with researchers from all around the world and learn from them: M. Abrecht, K. Altman, N. Barišić, D. Cloëtta, M. Falub, P. Fazekas, M. Grioni, H. Höchst, P. Hoffman, I. Kupčić, L. Pathey, M. Shi, F. Wiame.

I would like to thank the technical and support staff of the Institut de Physique des Nanostructures at EPFL; the Synchrotron Radiation Center in Stoughton, Wisconsin; the Swiss Light Source in Villigen, Switzerland; and L.U.R.E. in Orsay, France.

For their outstanding support I am thankful to L. Forró, D. Pavuna and D. Ariosa.

The success of this work critically depended on the talent, effort and support of H. Berger, for which I am grateful.

Special thanks to my thesis advisor G. Margaritondo, for providing the best conditions, opportunities and support.

I am blessed to have a great base in my numerous friends and my family. Thank you.

Abstract

Electronic properties of low-dimensional systems – and particularly quasi-one-dimensional systems – together with related correlated electron phenomena have for quite some time been at the very frontier of condensed matter physics. The interest ranges from purely fundamental reasons, since the reduced dimension offers a unique possibility of direct calculation of many-body problems, to nowadays very intense interest in functional nano-systems.

Angle-resolved photoemission spectroscopy (ARPES) is arguably the most direct probe of the physical properties of solids, which arise from low-energy electronic excitations. With the present state-of-the-art high energy/angle resolution detectors, it allows a direct insight into the most subtle effects of electron correlations. All the results presented in this Thesis are the first ARPES measurements on several inorganic chain-like materials that are, or are related to Peierls conductors. These quasi-one-dimensional correlated materials typically exhibit non-Fermi liquid like properties that are at the same time incompatible with any of the existing singular Fermi liquid scenarios (such as Luttinger liquid). In that respect the aim is twofold: to reveal the new physics arising from direct electronic structure measurements, and secondly, to compare the emerging models for the spectroscopic features with the new findings. More specifically, the Thesis focuses on the influence of the electron-phonon coupling on the observed excitations.

A quasi-one-dimensional insulating compound $K_{0.33}MoO_3$, known as molybdenum red bronze, is closely related to the blue bronze

$K_{0.3}MoO_3$, a 1D Peierls conductor. We disclose the details of the electron structure and reveal the important role of defect induced states. The small mobile polaron scenario describes well the blue bronze, and this picture is further strengthened, as we discuss here, by the spectroscopic similarities with the red bronze.

Then we present measurements on two transition metal trichalcogenides: $ZrTe_3$ and $TaSe_3$. The first is a Peierls compound whose peculiar Fermi surface hides its low-dimensional character. The latter, strikingly, even though it does not exhibit any instability, shows spectroscopic similarities with the Peierls conductors, thereby demonstrating the importance of electron-phonon interactions in this material, as well as the general importance of the particularities of the Fermi surface in setting the conditions for an electronic instability.

Finally, we report the results on one of the most intriguing materials in the field – $BaVS_3$. This correlated electron system demonstrates a wealth of complex, poorly understood phases. Extensive experimental findings cannot easily be put together into a coherent picture. Our direct electronic structure measurements suggest that the puzzling electronic properties are due to the interplay of the 1D states and a narrow localized band. We find supporting evidence for a one-dimensional instability driving the metal-insulator transition at 69 K and propose its realization through a mechanism of interband nesting.

We conclude that there is a direct link between the observed non-Fermi liquid features and the intrinsic characteristics of 1D Peierls conductors and/or one-dimensionality in general. The influence of electron-phonon coupling in conjunction with the reduced dimensionality leads to spectroscopic features that hide the realizations of the singular behavior. However, a detailed modeling of the new data presented here is necessary to place them in the framework of the emerging theories.

Version Abrégée

Les propriétés électroniques des systèmes à basses dimensions – en particulier celles des systèmes quasi-unidimensionnels – et les phénomènes de corrélation électronique qui leur sont associés ont longtemps été à la frontière de la physique de la matière condensée. L'intérêt suscité par de telles structures couvre un ample spectre qui va depuis des questions purement fondamentales, comme le problème à n-corps dont les calculs se verraient simplifiés grâce à la dimension réduite, jusqu'à l'engouement actuel pour les nano-systèmes. La spectroscopie par photoémission en résolution angulaire (ARPES) est sans doute l'outil le plus direct pour sonder les propriétés physiques provenant des excitations électroniques de basse énergie dans les solides. Les détecteurs de dernière génération permettent un accès direct aux effets les plus subtils des corrélations électroniques. Dans cette thèse, je me suis consacré à l'étude de plusieurs matériaux inorganiques à chaînes, qui sont -ou se rapportent à- des conducteurs de Peierls. Les résultats présentés dans ce rapport constituent les premières mesures ARPES jamais obtenues sur ces matériaux corrélés quasi-unidimensionnels, exhibant un comportement contraire à celui d'un "liquide de Fermi". Ces résultats sont, en outre, incompatibles avec tous les scénarios existants invoquant des liquides de Fermi singuliers (tels que le "liquide de Luttinger"). À ce sujet, mon but était double : tout d'abord, révéler la physique nouvelle provenant d'une mesure directe de la structure électronique et, deuxièmement, mettre à l'épreuve les modèles émergeants pour la spectroscopie, en les comparant avec les nou-

velles données. Plus précisément, j'ai surtout porté mon attention à l'influence du couplage électron-phonon sur les excitations observées.

En premier lieu, je vais présenter en détail l'étude d'un composé isolant unidimensionnel, le bronze rouge de Molybdène $K_{0.33}MoO_3$, composé fortement apparenté au conducteur de Peierls 1-D, le bronze bleu $K_{0.3}MoO_3$. Nous y déterminons la structure électronique et mettons en évidence l'importance du rôle joué par les états induits par les défauts. Les similarités spectroscopiques avec le bronze bleu, qui a été bien décrit dans le cadre du scénario des petits polarons mobiles, renforcent cette image. La situation simplifiée dans le bronze rouge, par rapport au bronze bleu, exclue certains des points faibles qui avaient été suggérés pour l'image polaronique.

Le chapitre suivant traite de deux métaux de transition trichalcogenides : le $ZrTe_3$ et le $TaSe_3$. Le premier est un composé de Peierls, mais les particularités de la surface de Fermi masquent son caractère unidimensionnel. Le deuxième, même s'il n'exhibe aucune instabilité, montre des similarités spectroscopiques avec les conducteurs de Peierls, ce qui démontre l'importance du couplage électron-phonon dans ce matériau, ainsi que la pertinence des détails de la vraie surface de Fermi pour déterminer les conditions d'une instabilité électronique.

Enfin, je vais présenter des résultats portant sur le plus intrigant des matériaux dans ce domaine – $BaVS_3$. Ce système électronique corrélé montre une riche variété de phases complexes mal comprises. Les abondantes données expérimentales sur ce matériau sont difficiles à compiler pour en extraire une image cohérente. Nos mesures directes de la structure électronique suggèrent que ces propriétés intrigantes résident dans une interrelation entre les états 1D et une bande étroite localisée. Noustrouvons une évidence attestant de l'existence d'une instabilité unidimensionnelle à la base de la transition métal-isolant observée à 69 K, pour laquelle nous proposons un mécanisme d'emboîtement de bandes (”interband nesting”). Nous concluons à l'existence d'un lien direct entre les propriétés ”non-Fermi liquid” et les caractéristiques intrinsèques des conducteurs de Peierls 1D et/ou unidimensionnels en général. L'influence du couplage électron-phonon en conjonction avec la basse dimensionnalité

confère aux systèmes étudiés des propriétés spectroscopiques qui masquent la réalisation des comportements singuliers. Néanmoins, un traitement détaillé des nouvelles données ici présentées s'avère nécessaire avant de pouvoir les placer dans le cadre des théories émergentes.

Contents

List of Figures

Publications

Submitted papers

Mitrovic S; Søndergaard C; Margaritondo G; Berger H; Barišić N; Cloëtta D; Ariosa D; Pavuna D; Forró L; Fazekas P; Höchst H: *Experimental electronic band structure and interband nesting in $BaVS_3$* Submitted

Refereed papers

Perucchi A; Søndergaard C; **Mitrovic S**; Grioni M; Berger H; Forró L; Degiorgi L *Spectroscopic and dc-transport investigations of the electronic properties of $TaSe_3$* THE EUROPEAN PHYSICAL JOURNAL B 2004, Vol **39**, No 4, pp 433-440

Abrecht M; Ariosa D; Cloëtta D; **Mitrovic S**; Onellion M; Xi XX; Margaritondo G; Pavuna D *Comment on "Strain and high temperature superconductivity: Unexpected results from direct electronic structure measurements in thin films" - Reply* PHYSICAL REVIEW LETTERS 2004, Vol 92, Iss 12, art. no. 129702

Mitrovic S; Perfetti L; Søndergaard C; Margaritondo G; Grioni M; Barišić N; Forró L; Degiorgi L *The electronic structure of a quasi-one-dimensional insulator: The Mo red bronze $K_{0.33}MoO_3$* PHYSICAL REVIEW B 2004, Vol 69, Iss 3, art. no. 035102

Abrecht M; Ariosa D; Cloëtta D; **Mitrovic S**; Onellion M; Xi XX; Margaritondo G; Pavuna D *Strain and high temperature superconductivity: Unexpected results from direct electronic structure measurements in thin films* PHYSICAL REVIEW LETTERS 2003, Vol 91, Iss 5, art. no. 057002

Perfetti L; Georges A; Florens S; Biermann S; **Mitrovic S**; Berger H; Tomm Y; Höchst H; Grioni M *Spectroscopic signatures of a bandwidth-controlled Mott*

transition at the surface of 1T-$TaSe_2$ PHYSICAL REVIEW LETTERS 2003, Vol 90, Iss 16, art. no. 166401

Lovrić D; Vučić Z; Gladić J; Demoli N; **Mitrovic S**; Milas *Refined Fourier-transform method of analysis of full two-dimensional digitized interferograms* APPLIED OPTICS 2003, Vol 42, Iss 8, pp 1477-1484

Grioni M; Berger H; Perfetti L; **Mitrovic S**; Reginelli A; Höchst H *Band features and strong correlations in 1D Peierls systems* JOURNAL DE PHYSIQUE IV 2002, Vol 12, Iss PR9, pp 33-38

Perfetti L; **Mitrovic S**; Grioni M *Fermi liquid and non-Fermi liquid spectral lineshapes in low-dimensional solids* JOURNAL OF ELECTRON SPECTROSCOPY AND RELATED PHENOMENA 2002, Vol 127, Iss 1-2, pp 77-84

Perfetti L; **Mitrovic S**; Margaritondo G; Grioni M; Forró L; Degiorgi L; Höchst H *Mobile small polarons and the Peierls transition in the quasi-one-dimensional conductor $K_{0.3}MoO_3$* PHYSICAL REVIEW B 2002, Vol 66, Iss 7, art. no. 075107

Chapter 1

Introduction

For more than half a century we can precisely describe most properties of normal elemental metals that we encounter and use. These properties are almost entirely linked to the outermost electrons of the constituent atoms. The nature of the electromagnetic force does not allow these electrons to be insensitive to each other or to the ions of the solid. Remarkably, the elementary excitations that fully describe properties of metals can be mapped one-to-one to the actual low-energy electrons and at the same time account for all the particularities [1]. These excitations represent a virtually non-interacting system – a gas of quasi-electrons know as the *Fermi liquid* – but not the actual electrons, so that they were named – quasiparticles. However, if we tried to fabricate a material that would be confined to a plane, or even better, to a single line to constrain the electrons, we could no longer expect them to easily avoid each other, and some sort of collective, correlated behavior should be expected [2]. Such exotic materials do indeed exist. The crystal structures of these compounds are still three-dimensional, but the basic structural units are usually infinite chains that are only weakly interconnected, through the van der Waals force, forming layered (quasi-2D) or even stacked needle-like (quasi-1D) single crystals. The actual electronic states do not have to be necessarily of the same dimensionality.

The technique of angle-resolved photoelectron spectroscopy (ARPES)

provides arguably the most direct way to probe the low-energy excitations [3]. In a typical ARPES experiment, the energy and the parallel momentum of photoemitted electrons are conserved providing us with the dispersion of the observed electronic states E(k) in a selected energy-momentum window. It should be noted that the actual result of an ARPES experiment is the spectral function of the single photohole A(k,ω) that is left after the extraction of the photoelectron, including the particularities of the photoemission process and interactions on the way. Indirectly we can also obtain information about the shape of the Fermi surface. Detector resolution in both energy and momentum that is available today allows detailed measurements of the states close to the Fermi surface where we find the signatures of electronic correlations and interactions with their resulting exotic states.

These correlations lead low-dimensional materials into new forms of electronic behaviors that can no longer be described by the quasiparticles of the Fermi liquid theory. They are often unstable in their metallic phase and below a certain critical temperature will develop curious ground states such as a charge or spin density wave [4], the Mott-Hubbard insulating state [5], or a superconducting state incompatible with the conventional BCS theory [6]. In fact, it is the discovery of high-temperature superconductivity in layered (quasi-2D) cuprates that has played a major role in shifting the center of interest of the condensed matter community to what is generally called *non-Fermi liquids* and thus low-dimensional systems.

The best understood form of a non-Fermi liquid is a Luttinger liquid [2]. Strictly speaking, one-dimensional metallic systems are Luttinger liquids, which is one of the rare exactly solvable many-particle cases in physics [7, 8]. On the other hand, it is known from the work of Peierls [9], that a one-dimensional metallic chain is intrinsically unstable towards a formation of a gapped, i.e. insulating, charge density wave state. The availability of quasi-one-dimensional materials allowed us to test this theory, and indeed a great number of them are Peierls conductors that behave as expected. They also show many non-Fermi liquid characteristics [10, 11, 12], but generally fail to show the spectroscopic characteristics of a Luttinger liquid;

namely the separation of charge and spin degrees of freedom. Luttinger liquid describes only gapless one-dimensional systems, but its aspects are not found in these materials even in the metallic phase far above the transition temperature. So far there are only a few reports [13], albeit controversial [14], on artificial metallic wires that show spectroscopic traits of the Luttinger liquid.

One of the most striking non-Fermi liquid features in ARPES is the *absence* of a clear Fermi surface in the metallic phase [15, 10]. The Fermi surface is a defining feature for metals and in ARPES E(k) dispersion maps it is manifested as a band-crossing of the Fermi level. The investigations of several Peierls compounds that preceded this work ($K_{0.3}MoO_3$, $(TaSe_4)_2I$) [16, 17] offered an alternative to explain these observations considering elementary excitations to be heavy particles – the so-called *polarons* – that arise from the interaction of electrons with phonons. Peierls transitions are driven by the electron-phonon interaction and it would be a natural notion to consider polarons as fundamental excitations. However, to draw more general conclusions we need to build a more extensive database of properties characteristic for these systems and test them against the new as well as established theories.

Even though the non-Fermi liquid spectroscopic characteristics of Peierls conductors and for instance layered cuprates in the underdoped region are similar, they may have different origins such as electron correlations and fluctuations of the order parameter [18]. For this work, we chose materials that are Peierls conductors or are closely related to such materials. One important aspect of this thesis is to find which of the observed spectral properties are linked to low-dimensionality (and possible Luttinger liquid behavior) and which to the particular class of Peierls conductors.

Molybdenum red bronze $K_{0.33}MoO_3$ was selected because it is a sibling material to the blue bronze $K_{0.3}MoO_3$ [19], a Peierls material that was well described within the polaron liquid scenario [17]. This is an insulating at all temperatures, quasi-one-dimensional compound. Interpretations through a Luttinger liquid are therefore excluded here. We find support for the polaronic scenario in the blue bronze, as will be discussed in Chapter 3.

The transition metal di- and trichalcogenides are another class of quasi-one- and two-dimensional compounds that demonstrate various instabilities and rather peculiar ARPES spectral features [20]. We have studied two of them; $ZrTe_3$ and $TaSe_3$. $ZrTe_3$ has a characteristic one-dimensional open Fermi surface which sets the conditions for the charge density wave. There is however a non-one-dimensional part of the Fermi surface that deeply affects the one-dimensional states. The observed excitations do not deviate much from Fermi liquid quasiparticles. $TaSe_3$ is closely related to the much studied double charge density wave system $NbSe_3$. It does not exhibit transport anomalies. In spite of this, spectral properties are quite similar to those that we find in the Peierls systems. In Chapter 4 we discuss the possible reasons behind the observed spectral functions in both compounds.

Despite the large experimental body of work, the last compound studied in this thesis in Chapter 5, $BaVS_3$, is still poorly understood. This quasi-one-dimensional compound is electronically an isotropic conductor of particularly low conductivity. It undergoes three transitions, all of which are poorly understood [21]. The metal-insulator transition has only recently been linked to one-dimensionality [22]. The band structure was at the center of the problematic reconciliation of all available experimental evidence. Our experimental electronic structure resolves many of these problems and offers support for a one-dimensional driving force behind the metal-insulator transition. Moreover, we propose a new possible scenario for the transition through the interband nested charge density wave formation. The spectroscopic features are found to be compatible to those of Peierls conductors. As is customary, the thesis is rounded off with a summary, an outlook for the further work, as well as the list of references.

Chapter 2

ARPES on low-dimensional materials

This chapter gives a brief and rather standard outline of the technique used in this thesis with the emphasis on its application to low-dimensional and in particular one-dimensional systems. Then we briefly treat the quasiparticle theory and a case of a typical Fermi liquid $TiTe_2$ from the perspective of angle-resolved photoemission. In the end the notion of the polaron liquid for Peierls conductors is expained on the example of the blue bronze $K_{0.3}MoO_3$.

2.1 Angle-resolved photoemission spectroscopy

Angle-resolved photoemission (or photoelectron) spectroscopy and several other photoemission techniques are based on the photoeffect: a photon that strikes the surface of a material can transfer its energy to an electron which under certain conditions can escape the surface. These photoelectrons can give us various indirect, yet in comparison to other techniques, probably the most direct information about the electronic structure of a single crystal. Photoelectrons are

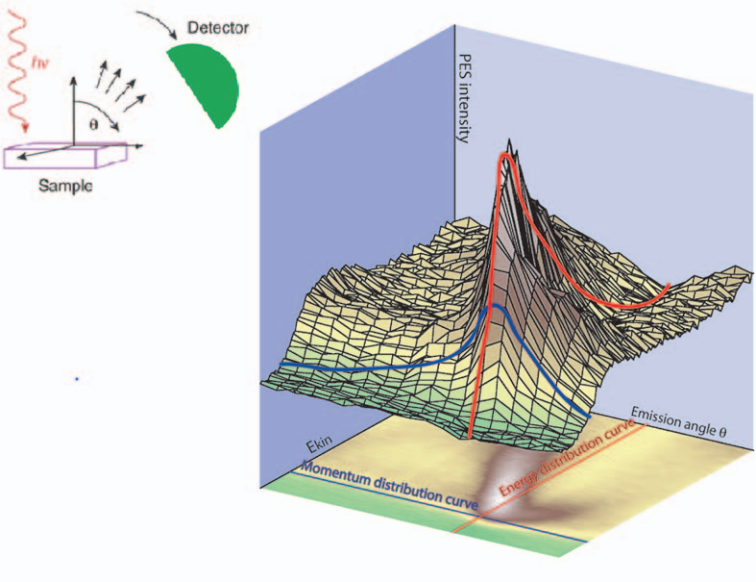

Fig. 2.1: Illustration of an ARPES experiment and its outcome. Photoelectrons are emitted from the surface and collected with an analyzer as a function of the emission angle and kinetic energy. The obtained information is usually summed up in intensity maps as shown here. Spectra can be analyzed in two equivalent representations - as energy distribution curves (EDCs) shown here in red, or as momentum distribution curves (MDCs) represented by the blue line.

collected with a detector that counts them according to their kinetic energy and momentum. If we gather both, we speak of the angle-resolved photoemission spectroscopy (ARPES). Otherwise, we call it angle-integrated PES. Many detailed overviews of photoemission techniques can be found in the literature [3, 23].

A typical outcome of an ARPES experiment and a schematized setup are shown in Fig. 2.1. Photoelectrons ejected by the monochromatic light are collected by the analyzer that gathers them as a function of energy and angle. Single channel analyzers usually collect

intensity as a function of kinetic energy, the so-called energy distribution curves (EDC's), repeatedly for successive angles of emission. Today, however, it is common to have a multi-channel analyzer that can collect I(θ,E_{kin}) maps in a certain energy-angle window.

The electrons that do not scatter inside the solid conserve the energy and parallel momentum in the photoemission process. The perpendicular component is not conserved due to the refraction and complicates angle-momentum relation for the three-dimensional materials. In layered materials we do not have this problem and the angle of emission is easily translated into momentum. The kinetic energy of electron reflects its binding energy while in the solid. The two operational relations are then

$$E_B = h\nu - E_{kin} - \Phi \tag{2.1}$$

$$|k_{\|}| = \frac{\sqrt{2mE_{kin}}}{\hbar} \sin\theta = 0.512\sqrt{E_{kin}} \sin\theta \tag{2.2}$$

(m is electron mass, and $h\nu$ the photon energy) where the last equation gives momentum in Å^{-1} if we enter kinetic energy in eV. The first equation demonstrates that electrons have to overcome a potential Φ to escape from the surface. Operationally, the first equation is simplified for the following reason. The Fermi energy E_F corresponding to $E_B = 0$ is determined by the work function of the analyzer [3]. By measuring the Fermi edge on a polycristaline sample we can calibrate the instrument to take measurements in binding energy directly since it does not depend on the sample. Of course, the sample has to be in electrical contact with the analyzer. Equations 2.1 and 2.2 underline two important requirements on the photoemission experiment. The first equation requires that the sample is grounded, and to the same ground as the analyzer. As photoelectrons leave the surface, there has to be a compensating current of electrons that prevents charging of the surface that could create fields and slow down the photoelectrons. Second equation requires complete absence of magnetic fields as they would interfere with trajectories of photoelectrons. For that purpose all the samples that enter the analyzer chamber have to

be demagnetized and sample holders made from preferably non-magnetic metals (usually aluminum or copper).

The two equations map $I(\theta, E_{kin})$ to $I(k, E_B)$. Notice that equation 2.2 has a non-linear relation of k to the emission angle and is at the same time dependent on the kinetic energy. If we look at the region close to the Fermi level (within around 1 eV) for typical photon energies used (around 20 eV or higher) the square root term can be substituted with the kinetic energy of the electrons from the Fermi level. This range of photon energies is also convenient since we can neglect the momentum of the photons as well. When we measure ARPES maps, we are primarily interested in the electronic states in the material, that is, the initial states of the electrons. Photoemission process involves the transition from the intial state to the available finite state, which may or may not be available, and also depends on their symmetries. What we finally measure in the intensity map are the states of the photohole

$$I(k, E_B) \propto A(k, E_B) f(E_B, T) \tag{2.3}$$

where $A(k, E_B)$ is the single particle spectral function, $f(E_B, T)$ the Fermi-Dirac distribution function. The proportionality factor contains the matrix element of the transition from the initial to the final state. The matrix element determines the probability for a transition from an initial to the final state, and it is only approximately a constant factor for a given photon energy. Obviously, the interpretation of ARPES results is not straightforward for many reasons, from the influence of final state effects to the very applicability of the single-particle interpretation. Also, we assume that the photoelectron extraction and the response of the system happen instantaneously. All theories of photoemission are subject to this so-called *sudden approximation*.

Another important point when considering ARPES determined band structure is its surface sensitivity. The curve of the Figure 2.2 shows that in the range of 10 - 100 eV, which is the usual range of measured kinetic energies for the valence band spectroscopy, the escape depth of electrons is of the order of few Å. The requirement for

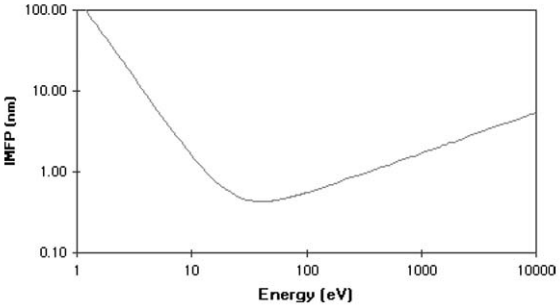

Fig. 2.2: Inelastic mean free path of electrons as a function of electron kinetic energy in a log-log scale. This is a universal curve characterizing the electron escape depth from materials.

ordered, clean surfaces is very strict. The experiments are therefore conducted in the ultra-high vacuum environment (UHV) and the surfaces are specially prepared before the measurements, depending on the sample, by cleaving, annealing, scraping or similar. In the end, the measured electronic states are relevant only for the first few atomic layers of the material. Low-dimensional layered materials with weak bonds between layers – and no surface reconstruction – are therefore particularly suited for the ARPES measurements that are relevant for the bulk properties. If we wanted to do a more bulk-sensitive ARPES, two evident solutions are going to very low or to very high photon energies. Indeed, both types of ARPES are starting to gain momentum recently. There are however many specific problems. For instance, low photon energy region is limited by the work function of the material/analyzer limit (around 4 eV), which leaves a narrow range of several photon energies available. Also, very different final states are probed, and especially in the low-energy range, matrix element becomes a very important factor.

Fig. 2.3: A single crystal of $BaVS_3$ glued on a pin of a sample holder and mounted with a cleaving pin on top.

2.2 A typical ARPES experiment and instrumentation

The basic parts of the instrumentation are the source of light, the UHV chamber and a detector. The source of light for ARPES is a UV lamp or synchrotron light in the UV to soft X-ray range. In our lab in Lausanne, we use two He discharge lamps, a VG lamp and a VUV Gammadata lamp. Synchrotron light, due to its tunability, polarization and intensity, is the most versatile source of photons for photoemission. For the work in this thesis we have used electrostatic analyzers: fixed hemispherical analyzers ESCA-300 in our lab, SES-200 (at SRC, Wisconsin) and SES-2002 (SRC, Wisconsin; SLS, Switzerland) from Gammadata, and a motorized VG analyzer (ASTRID, Denmark). The resolution of the best analyzers today is under ΔE=1 meV and $\Delta\theta$=0.1°. The newest gammadata analyzer also has a larger angular allowance that considerably reduces the time of acquisition.

All the samples in this thesis were prepared for cleaving inside the UHV chamber (see Fig. 2.3). The obvious quasi-one-dimensional structural character of $BaVS_3$ and $TaSe_3$ made the orientation of the crystals trivial. Other samples were oriented by Laue X-ray diffrac-

tion. The sample is cleaved in the UHV chamber and electrically and thermally (for the cooling purposes) connected to the manipulator in front of the analyzer.

The quality of the surface plays a crucial role in the experiment. A "good cleave" that reveals a ordered surface is a prerequisite for each ARPES experiment. Disordered surfaces influence the spectra in two ways: they can change the surface coordination and thus electronic states, or lower the momentum resolution since the angle of emission is not as well defined. The preparation for the cleave as shown in Fig. 2.3 is therefore a critical step. The longer side of the crystal from the figure is 2 mm long and is glued between two aluminum pins, one of which is attached to the sample holder. The lower pin has a smaller surface than the crystal to be out of the focus of the analyzer (this is not important when using small spots of the sychrotron light). The glue is a conducting silver epoxy.

Then, we have to consider the degradation of the surface during the experiment. Two factors that are always present can reduce the surface quality: the exposure to radiation, and the imperfect vacuum. Exposure to the radiation is especially important in the experiments with synchrotron light due to high intensities of the light. The exposure time necessary depends on the sample and the signal that we get from it, and the compromise between good statistics and exposure time often has to be made. This mechanism of surface deterioration is particularly important in the Mo bronzes. In Fig. 2.4 we show how the radiation damage can influence the spectra [24]. The intensity map in (a) is taken with a VG He discharge lamp that has a much lower intensity than the Gammadata VUV lamp that was used for the map in (b). This compound is an oxide, and the oxygen stoichiometry can easily be changed with exposure to radiation. The new conditions on the surface increase the signal in the lower binding energy part of the peak from the surface of "good stoichiometry".

The vacuum is never perfect, usual conditions are of the order of $10^{-10} - 10^{-12}$ mbar, but still during longer measurements, and if the sample allows, annealing is necessary to eliminate the depositions on the surface. Cooling is from that point of view a very critical operation. As we get close to temperatures of liquid helium, the

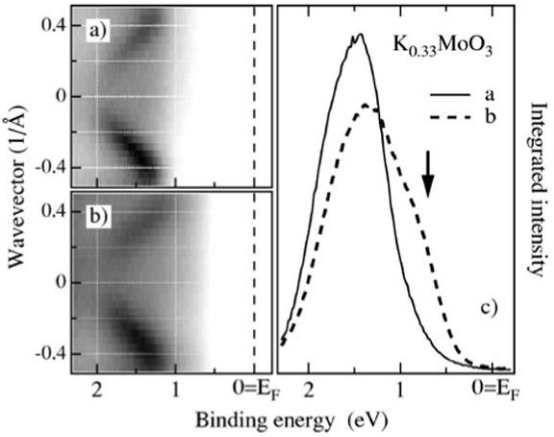

Fig. 2.4: The effects of surface degradation in red bronze $K_{0.33}MoO_3$. The spectra in a) were taken with a much lower intensity VG lamp, and the ones in b) with a Gammadata He lamp. The radiation destroys the oxygen stoichiometry on the surface. The corresponding momentum-integrated spectra are shown alongside.

sample acts as a "cryogenic pump" and attracts particles that are in the chamber.

Another undesirable condition associated with cooling is sample charging. This is particularly important in the semiconducting and poorly conducting materials. The recompensation of the charges on the surface is crucial for ARPES as discussed earlier. In the measurements of the insulating red bronze, we have tried to insure that there is a electrical contact with the surface by putting a graphite film around the visible edges of the non-cleaved (with a pin on top) crystal. After cleaving there is a pool of electrons that is in direct contact with the surface of the crystal from the side of the edges. For each poorly conducting compound we have checked if charging is present. To illustrate this, Fig. 2.5 shows momentum-integrated curves of the valence band close to the Fermi level in $BaVS_3$ at

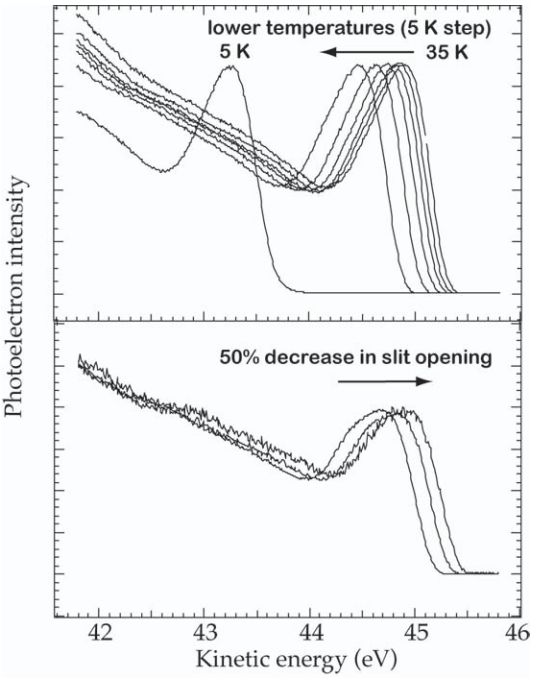

Fig. 2.5: Momentum-integrated curves of the states near the Fermi level in $BaVS_3$ taken at several temperatures below 35 K. The sample starts charging due to its very low conductivity at those temperautres. The spectra shift to lower binding energies. We know that this is the effect of charging since the change in light intensity, by closing the entrance slit opening, brings the spectrum back to the right energy.

temperatures under 35 K. In this temperature region, the sample is in the insulating phase and starts charging as the surface loses the electrical contact with the sample holder. i.e. the ground. In this case, there is a puzzling phase transition at 30 K, and it is important to understand the abrupt spectral changes. We can easily verify that this is indeed a case of charging by closing the entrance slits of beamline, thus lowering the intensity of light. In the lower plot of Fig. 2.5 we see that the spectrum returns to the lower binding energies. Charged

surfaces, even in the case of smallest charging, add a potential that electrons need to overcome to reach the analyzer which lowers their kinetic energies.

2.3 Quasiparticles: Fermi liquids

Before tackling the exotic electronic states, we have to know what are the characteristics of "well behaved" metals. So what are the Fermi liquids, quasiparticles and how do we see them in ARPES spectra is the question that will be addressed in this section in a rather descriptive way.

2.3.1 The Fermi liquid

One of the most remarkable successes of the quantum theory is its application to crystals. This microscopic theory is capable of providing a complete description of "normal" metallic solids (such as Au, Cu, ...) that are basically systems with the order of 10^{23} interacting particles. The Landau's Fermi liquid theory [25, 1] successfully reduced this complicating many-body system into a single-particle picture. The new non-interacting particle – named *quasiparticle* – retains all the quantum numbers of electrons but contains at the same time all the information about the interactions as well.

The starting point for Landau's theory is the gas of free electrons. By applying the Fermi-Dirac statistics and Pauli's exclusion principle we obtain the ground state of the free electron gas – the Fermi sea – characterized by the sharp cutoff of occupied states at the Fermi energy E_F and Fermi momentum $p_F = \hbar k_F$. The Fermi wave vector defines a spherical Fermi surface under which all enclosed states are filled. This picture could not account for some experimental observations, notably specific heat capacity and magnetic susceptibility.

The answer came from Landau who applied a principle of "adiabatic continuity", or "slow" switching on of the interactions between electrons and postulated quasiparticles [1, 26]. They map one-to-one the low-energy eigenstates – and so being relevant only in the

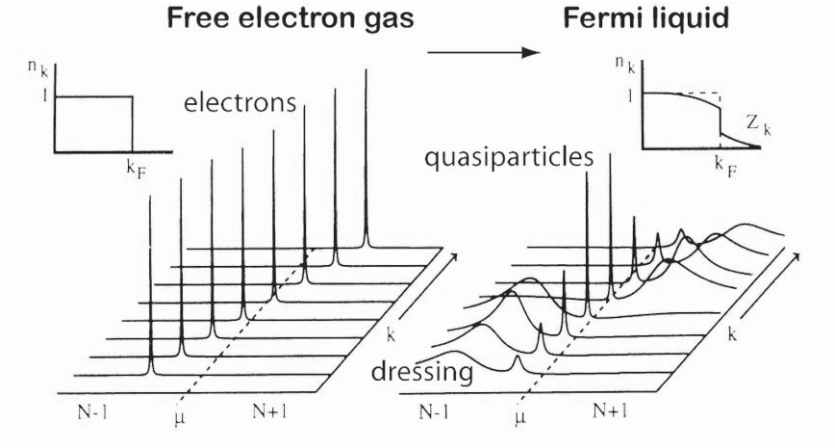

Fig. 2.6: Transition from a free electron gas to a Fermi liquid upon adiabatic switching on of interactions. Corresponding densities of states for T = 0, and dispersion relations for unoccupied and occupied states around the chemical potential. Parameter z_k is known as order parameter of Fermi liquid.

region close to the chemical potential (Fermi level) – to a system of non-interacting fermionic quasiparticles that retain the quantum numbers of electrons/holes but with changed wavefunctions and energies. This is illustrated in Fig. 2.6. The change in energy is reflected in the "dressing" that contains the pushed-out part of the states. Consequently, the mass of the quasiparticle does not correspond to the one of the electron (which could already have a renormalized mass due to the effect of the lattice potential). Fig. 2.6 also demonstrates the changes in the spectral function $A(k, E)$ which represents a probability to find an electron of a wave vector k with the energy E (the same term as in eq. 2.3). The probability function for electrons in a free electron gas is the δ-function. On the other hand, for a quasiparticle it is a function of k and peaks at a different energy that comprises the change in mass. The peak sharpens as k approaches the Fermi level and goes into the δ-function at the Fermi

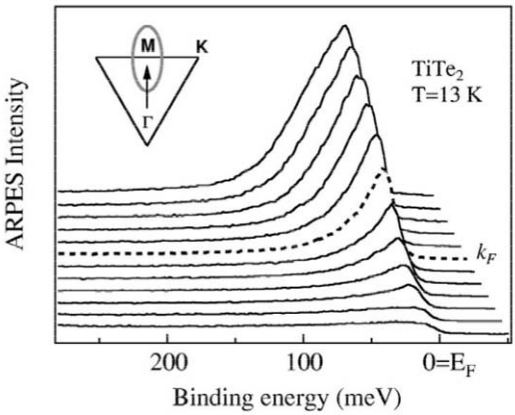

Fig. 2.7: ARPES spectra ($h\nu$=21.2 eV; T=13 K) of the 2D Fermi liquid system $TiTe_2$ near the Fermi surface crossing along the high symmetry ΓM direction in the Brillouin zone. The dashed line is the spectrum measured at the Fermi wavevector (the Fermi level crossing).

energy. The width of the peak is proportional to the scattering rate and inversely to the lifetime. So the long lived quasiparticles near the Fermi surface define the region where the approximation of switching on interactions "slowly", and therefore the Fermi liquid model, works the best.

2.3.2 Seeing quasiparticles in ARPES

The Fermi liquid realizations exist also in 2D systems. Here I present results on 1T-$TiTe_2$, a material that has been previously studied in our group. This material, alongside copper, is one of the perfect examples from photoemission of a "normal" metal that can be described in the Fermi liquid scenario[27]. The reason behind this is a very simple band situation: there is just one band crossing the Fermi level with almost no background.

The following text has been published as a section in *L. Perfetti, S. Mitrovic and M. Grioni, J. Electron Spectroscopy and Related Phenomena*

127 (2002) 77-84:

The proportionality, via energy- and symmetry- dependent transition matrix elements, between the ARPES spectrum and the single-particle spectral function (as in eq. 2.3) is expressed in:

$$A(k, E_B) = \frac{1}{\pi} \frac{Im\Sigma(k, E_B)}{(E_B - E(k) - Re\Sigma(k, E_B))^2 + (Im\Sigma(k, E_B))^2} \tag{2.4}$$

$E(k)$ is the ideal dispersion relation of the electrons in the absence of interactions, and $\Sigma(k, E_B)$ is the selfenergy operator, which includes the many-body effects. The spectral function is a fundamental theoretical quantity which fully characterizes the single-particle properties of a many-body system [4]. Several important quantities, like the momentum distribution function $n(k) = \int A(k, \omega) d\omega$, or the density of states $\rho(\omega) = \int A(k, \omega) dk$, can be directly derived from the knowledge of $A(k, \omega)$.

In ARPES experiments, it is increasingly common to record full $I(k, E)$ maps of the photoelectron intensity over a defined energy-momentum window. In a simple one-band situation, the intensity is distributed along the band dispersion, as schematically illustrated in Fig. 2.1. The data are then presented as energy distribution curves (EDC) $I(k^*, E)$ at constant wavevector, or as momentum distribution curves (MDC) $I(k, E^*)$, at constant energy. In the limit of a complete sampling the two representations are obviously equivalent, and carry the full information of the intensity map. Since the self energy Σ typically depends more strongly on energy than on momen- tum, the MDCs have an essentially lorentzian lineshape, with a width $\Delta k = (1/l)$ equal to the inverse of the quasiparticle correlation length. In a Fermi liquid system, the EDCs have a characteristic and more complex lineshape. The energy width $\Delta E = 2Im\Sigma = \hbar/\tau$, where τ is the quasiparticle lifetime, yields the total quasiparticle scattering rate.

$TiTe_2$ is a layered compound with rather strongly anisotropic properties which justify its classification as a quasi two-dimensional (2D) conductor. The resistivity is metallic, with a large perpendicular versus in-plane ratio $\rho_{out}/\rho_{in} \sim 40$. Previous studies [5] have con-

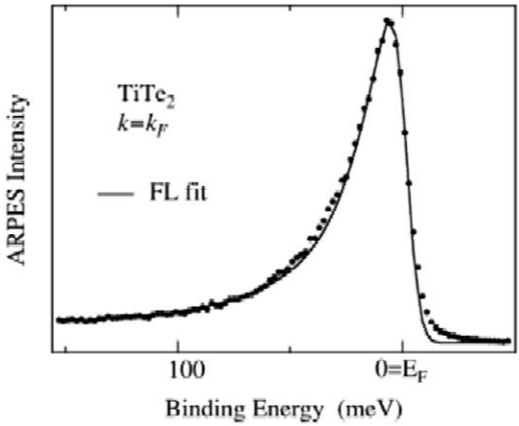

Fig. 2.8: ARPES spectrum of $TiTe_2$ for $k = k_F$ from Fig. 2.7. The solid line is a FL fit which takes into account the experimental energy and momentum resolution.

cluded that its properties are well described by Fermi liquid theory. Its simple band structure, close to an ideal single-band situation, and the 2D character are favourable for an ARPES study of the FL lineshape. Fig. 2.7 illustrates the dispersion of the Ta *d* conduction band along the ΓM direction of the Brillouin zone, at T=13 K. As predicted by band structure calculations, the ARPES peak disperses through E_F, i.e. the ΓM line crosses one portion of the FS, in correspondence of the elliptical electron pocket centered at the M point. The Fermi crossing is evident from the rapid increase in intensity with increasing angle, but determining the Fermi wavevector is not straightforward, due to the perturbing effect of the sharp FermiDirac distribution. A FL fit to the individual spectra, which takes into account the finite experimental energy and momentum resolution [6], is required to extract from the data the QP dispersion – which does not coincide with the peaks maximum in proximity of E_F.

Fig. 2.8 illustrates the fit for $k = k_F$. A fit for the whole series of spectra of Fig. 2.7 is possible by assuming an intrinsic energy-dependent broadening $Im\Sigma = \beta E^2 + \Gamma_0$, with $\beta \sim 1$ eV, and Γ_0=17

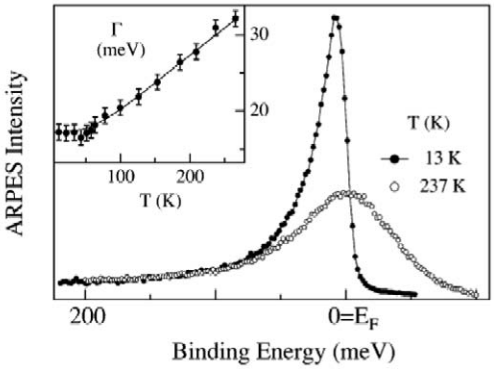

Fig. 2.9: ARPES spectrum of $TiTe_2$ for $k = k_F$ at T=13 K (solid symbols) and T=237 K (open symbols). The temperature-dependent intrinsic linewidth Γ (HWHM) is shown in the inset, together with a theoretical fit (solid line) with an electronphonon coupling constant λ=0.22, and a phenomenological zero-temperature constant Γ_0=17 meV.

meV. The first term, which reflects electron-electron scattering, is actually negligible (a few meV) in the narrow angular range (3°) of the figure, in agreement with transport data [7]. According to FL theory, at T=0 and at the FS, the quasiparticle feature should have zero width, corresponding to an infinite lifetime. The nonzero ARPES width is the result of the finite experimental resolution and temperature, and of additional broadening terms.

The contribution of phonon scattering can be estimated from the temperature dependence of Fig. 2.9. The spectrum is broader at higher temperatures, due to the larger electronphonon scattering. It is also more symmetric as a result of the broadening of the Fermi-Dirac function. This dependence could be analyzed by a standard theoretical treatment of the electron-phonon self energy $\Sigma_{e-ph}(\omega, T)$ [4], but we find that an excellent agreement with experiment is already achieved when the energy dependence is neglected. This is equivalent to the assumption of a lorentzian broadening, with a (half-)width $\Gamma(T)$ (inset) which decreases linearly down to ∼60 K, in

excellent agreement with the electrical resistivity [6], and then saturates to a constant value Γ_0=17 meV. From these data, we can estimate the dimensionless electron-phonon coupling parameter λ=0.22 using the theory of Ref. [4] (solid line) with an added phenomenological constant Γ_0. Alternatively, λ can be estimated from the linear slope of $\Gamma(T)$, considering that $\Gamma = (\hbar/2\tau) = const + \pi\lambda k_B T$ [7]. In both cases, there is good agreement between the spectroscopic and the resistivity values.

The results presented on the model metallic system $TiTe_2$ demonstrate that ARPES with high resolution can indeed probe the dynamical properties of the quasiparticles.

2.4 1D systems: Luttinger liquid and Peierls instability

The physics of electrons in 1D is quite different than the 3D case. The Fermi liquid paradigm theoretically breaks down in 1D where Luttinger liquid scenario takes over as first described by Haldane in 1981 [2]. Luttinger liquid describes a 1D metallic gapless systems of interacting electrons. This is a directly solvable many-body problem for which a direct calculation of spectroscopic properties is possible. Here we will just discuss the spectroscopic realizations of the scenario.

We will have to consider two effects that arise from one-dimensionality: (i) The Luttinger liquid that is a consequence of the forward scattering between electrons, and (ii) spontaneous opening of a gap at E_F and a formation of a charge density wave as a consequence of backward scattering of electrons between nested Fermi surfaces [9].

The most notable aspects of the Luttinger liquid are the following: the absence of fermionic quasiparticle excitations and the separation of spin and charge degrees of freedom; anomalous dimension α of fermions producing the non-universal power-law decay of correlation functions; possibility of evaluation of all correlation functions; universal relations between the coupling constant and the exponents

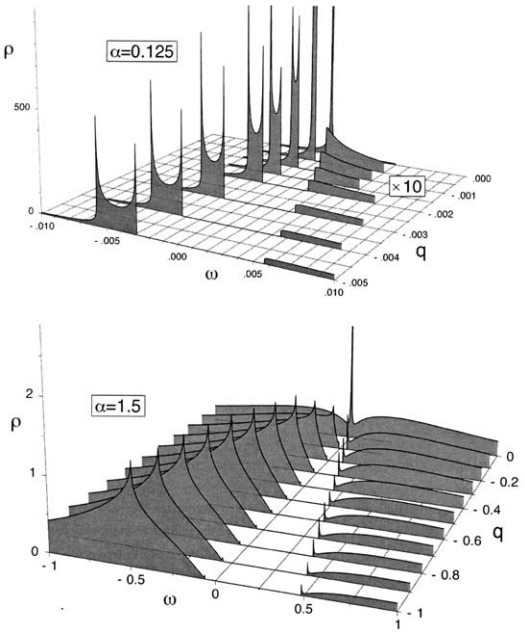

Fig. 2.10: Single particle spectral functions of the Luttinger liquid for two values of the anomalous dimension. ARPES spectra on 1D systems could be compatible with the lower picture, and suggest strong, long-range interactions.

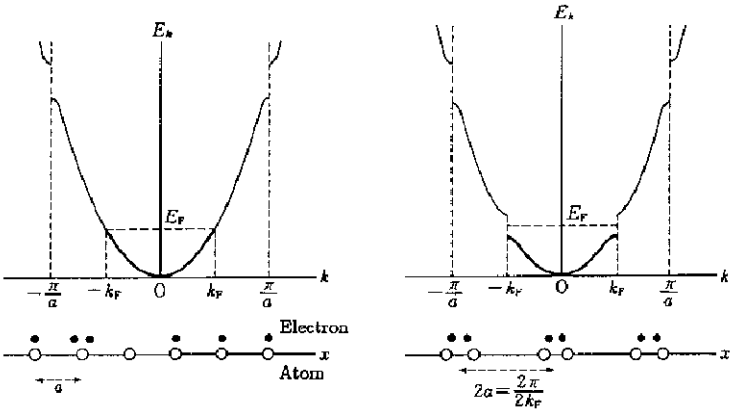

Fig. 2.11: The Peierls instability: the presence of an interaction component with wave vector $q = 2k_F$ in a 1D electron gas hybridizes the two Fermi points at $\pm k_F$, and opens a gap at the Fermi level

of correlation functions and spectral properties; persistent currents determined by $2k_F$. The Luttinger liquids are described within the Tomonaga-Luttinger model [28, 29].

Even though parallels cannot be drawn with the Fermi liquid theory, in a simplified way we can say that instead of the fermionic quasiparticles of the Fermi liquid, in a 1D case valid eigenstates with their energies are the bosonic entities of the density of spin and charge. For detailed treatment please refer to [7, 26].

What are the spectroscopic signatures of these new states? Fig. 2.10 shows the spectral function $A(k, \omega)$ of a 1D Luttinger liquid. We notice two singular features – the holon and spinon – and an incoherent part. Spinon and holon disperse with different velocities and merge at $k = k_F$. Experimental observations of the spin–charge separation have been reported on metallic wires [13], but the results remain controversial. Most of the spectroscopic evidence for the Luttinger liquid comes from characteristic power-laws.

1D systems have parallel open Fermi surfaces. 1D electrons will spontaneously open a gap at the Fermi surface when coupled to

phonons with a wave vector $2k_F$. The ground state of 1D systems is, therefore, an insulating state accompanying the lattice distortion and a modulation of the charge density (a charge density wave, CDW). The same goes for electron-electron coupling and a formation of spin density waves (SDW). In addition, fluctuation effects are very important and a pseudogapped state is often present before the actual transition. From this we draw two conclusions: that 1D systems are in their nature non-Fermi liquids, and secondly, that the Luttinger liquid scenario, valid only for gapless systems, cannot be applied always. If we search for Luttinger liquid signatures in ARPES spectra we have to also bear in mind that the Luttinger liquid is well defined only in the region close to the Fermi level.

So far, several organic compounds and some inorganic ones with highly anisotropic transport, displayed open Fermi surfaces and the realization of a charge density wave ground state [12]. At the same time they display non-Fermi liquid like lineshapes that could be, specifically in the class of Peierls conductors, explained by the electron-phonon interactions. The basic ideas behind the polaronic picture are presented in the following section which is a reproduction of the publication *L. Perfetti, S. Mitrovic, G. Margaritodno et al*, PRB **66** (2002) 075107:

2.4.1 Mobile small polarons in $K_{0.3}MoO_3$

Introduction

Lattice periodicity and band filling determine the behavior of charge carriers, and ultimately the electronic properties of solids, in the limit of vanishing interactions. This is no longer true in strongly interacting systems, where translational symmetry is not necessarily manifest in the wavefunctions of individual carriers. The renormalized single-particle excitations - or quasiparticles (QPs) - postulated by Fermi liquid theory, can be quite different from the bare electrons, and new phases with distinct macroscopic properties may appear.

Quasi one-dimensional (1D) materials exhibit typical electronic instabilities, like the much studied metal-insulator Peierls transition

to a charge-density-wave (CDW) state. Understanding how the QPs evolve into the ordered phase, where the one-to-one correspondence with the non-interacting particles is lost, is of fundamental interest. The accepted picture of the CDW instability emphasizes extended, periodic states and the topology of the 1D Fermi surface, which is perfectly 'nested' on itself by a translation with wavevector $Q_{CDW} = 2k_F$ (k_F is the Fermi wavevector). This weak-coupling theory describes quite successfully the superstructures revealed by scattering experiments, but elements of the opposite strong-coupling scenario [30] may be relevant in materials where the charge density modulations are large.

1D materials are also of current interest for their *normal* phase. Strictly 1D metallic systems are not Fermi liquids, but Luttinger liquids [2], with peculiar properties like spin-charge separation, and correlation functions characterized by non-universal exponents [8]. 1D systems with gaps in the spin sector - especially relevant for the Peierls instability - or in the charge sector are also possible. They are neither Fermi nor Luttinger liquids, but belong to the Luther-Emery of Mott-insulator universality classes [31, 7]. Recent spectroscopic work, namely by optics [32] and photoemission [12], aimed at identifying the unique spectral features of these correlated 1D states. Signatures of spin-charge separation have been reported in 1D Mott insulators [33], while data on conductors, either inorganic like $Li_{0.9}Mo_6O_{17}$ [34] or organic like TTF-TCNQ [35], and on artificial 1D surface nanostructures [13] are still debated. Puzzling, common aspects of the ARPES spectra are the broad lineshapes, and deep pseudogap features.

Strong pre-transitional fluctuations in a broad temperature range between the real (T_P) and the expected mean-field (T_{MF}) transition temperatures, are another typical feature of the physics of 1D Peierls materials. Fluctuations are manifest in the temperature dependence of the CDW correlation length extracted from diffraction data [19]. They also influence the electronic states, causing the opening of a pseudogap at the Fermi level [18, 36, 37]. The spin susceptibility [38], specific heat and optical conductivity [39] of 1D Peierls systems bear signatures of the pseudogap. CDW-related superstructures are also

observed above T_P by ARPES [40, 41].

In this chapter we address the nature of the QP states, and the spectral signatures of the CDW in a typical 1D Peierls material: the Mo blue bronze $K_{0.3}MoO_3$. We find valence states with the symmetry properties predicted by band structure calculations, including a good FS nesting at the CDW wavevector. We also find that the energy of these dispersing features is not related to the low-energy properties of the material. We interpret the peculiar lineshape as the result of strong interactions with the lattice, leading to the formation of small polarons with strongly renormalized masses [16]. This hypothesis is supported by a new analysis of the optical data. From temperature-dependent momentum distribution curves measured at the Fermi surface we identify, within a polaronic scenario, the spectral signatures of the Peierls transition, and of pre-transitional fluctuations. These results suggest that elements of both the weak and strong coupling theories should be included in a description of the metal-insulator transition.

Structural and electronic properties

$K_{0.3}MoO_3$ has a side-centered monoclinic structure, where double chains built from MoO_6 octahedra run along the crystallographic **b** direction, supporting Mo $4d$ - O $2p$ hybrid bands with strong 1D character. The interaction between adjacent double chains splits these bands into bonding (B) and antibonding (AB) subbands which are doped by charge transfer from the K^+ ions [42, 20]. These bands generate two pairs of open Fermi surface sheets, perpendicular to the ΓY direction (**b**), with distinct Fermi wavevectors k_F^B and k_F^{AB}. Due to interchain coupling, the FS are slightly warped, with alternate concavities. Tight-binding calculations [42] and measurements of the transverse CDW correlation length [43] yield a transverse dispersion $4t_\perp \sim 0.1$ eV, where $t_\perp$ is the in-plane hopping matrix element. A more recent *ab initio* band structure calculation, performed with the generalized gradient approximation (GGA) scheme finds nearly flat FS sheets [44].

The metallic state is unstable below T_P = 180 K. The CDW for-

mation has been associated with the alternate nesting of the B and AB FS sheets with a single wavevector $Q_{CDW} = (0, q_b, 1/2)$, where $q_b = (k_F^B + k_F^{AB})$ is incommensurate ($q_b = 0.73b^*; b^* = 2\pi/b$) at T_P, and locks in to the commensurate value $q_b = 0.75b^*$ below 100 K [45]. The saturation value of the Peierls gap is $2\Delta_0 = 100 - 150$ meV, from optics and resistivity [39], consistent with ARPES [15, 11].

Experimental

Single crystals of $K_{0.3}MoO_3$, of typical size $3 \times 1.5 \times 0.5$ mm^3, presented a strongly anisotropic electrical resistivity and semiconducting behavior below T_P = 180 K, in agreement with the literature [45]. We performed ARPES measurements at the PGM beamline and NIM4 beamlines of the Wisconsin Synchrotron Radiation Center (SRC). Photoelectron intensity maps were acquired with a Scienta SES-200 analyzer, with energy and momentum resolution $\Delta E = 15$ meV and $\Delta k = 0.015 \AA^{-1}$ respectively. The samples, mounted at the tip of a closed-cycle He refrigerator, were post-cleaved at T = 60 K at a pressure of 6x10^{-11} mbar, to expose mirror-like $(\bar{2}01)$ surfaces. Special care was taken to minimize radiation exposure, and we did not observe noticeable signs of surface degradation over a period of several hours.

The discussion of the optical properties is based on the original data of Ref. [39], obtained over an extended frequency range (0.1 to 10^5 cm^{-1}) as a function of temperature and employing a wealth of methods as optical reflectivity and resonant cavity techniques. The optical conductivity was determined from the complete absorptivity spectrum by a Kramers-Kronig analysis, as described in Ref. [39].

The symmetry of the bands and the Fermi surface

Figure 2.12(a) shows ARPES spectra measured in the metallic phase (T = 210 K) along the 1D chain direction **b** (ΓY). Photoelectrons excited by linearly π-polarized light were collected in the (horizontal) plane containing the surface normal, the **b** direction, and the photon beam (Fig. 2.12(b)). This geometry selects initial states that are even

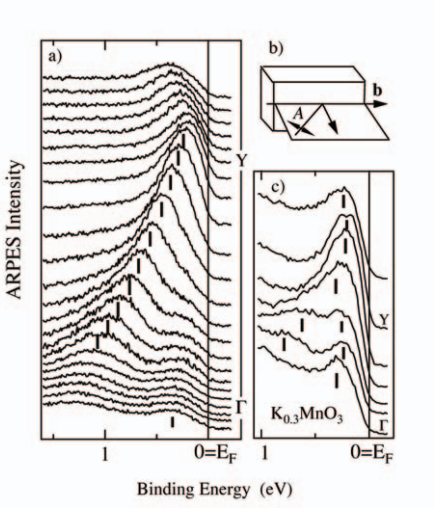

Fig. 2.12: (a) ARPES spectra acquired along the **b** (ΓY) direction (T=210 K, hν=21 eV); (b) Setup of the ARPES experiment. Notice that the polarization plane is perpendicular to the surface and contains the direction of the chains. (c) Spectra measured with unpolarized light (from Ref. [10]).

under a reflection from this plane. A prominent spectral feature disperse from $\sim$ 1.2 eV at Γ, the center of the Brillouin zone (BZ), to a minimum binding energy of 0.2 eV near the zone boundary $Y = (\pi/b) = 0.415\mathring{A}^{-1}$. A second, much weaker feature is observed around Γ at smaller binding energy. They represent the B (at higher binding energy) and AB (closer to E_F) subbands. Their dispersion is well described by the more recent band structure calculation [44]. The spectra are consistent with published ARPES data [11, 46, 47], but there is a remarkable difference with respect to data measured with unpolarized radiation (Fig. 2.12(c), from Ref. [10]), where the AB and B structures have comparable intensities.

The large polarization dependence suggests that the two bands have different symmetries. This is supported by scans above and below the horizontal plane. The acceptance window of the ana-

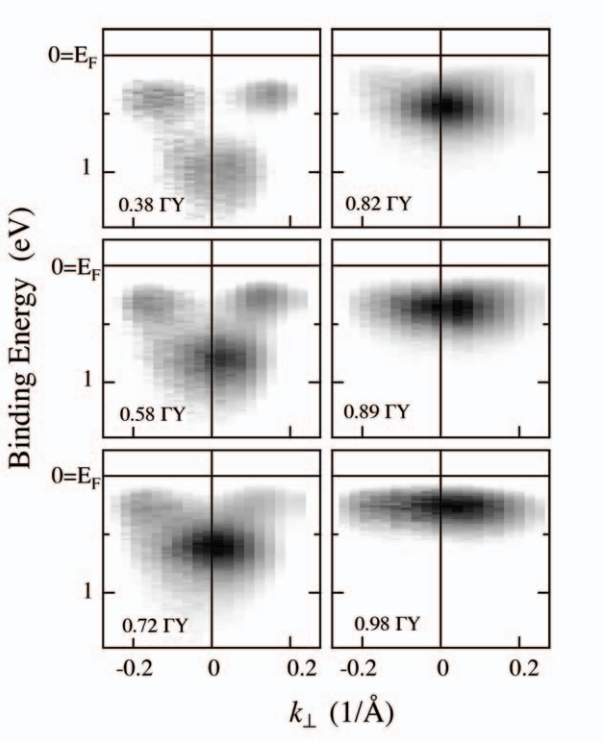

Fig. 2.13: ARPES intensity maps measured perpendicular to the chains, for various values of the wavevector along the chains $k_{\|}$ (T=180 K, $\hbar\omega$=21 eV). Darker regions correspond to larger intensity.

lyzer allowed us to collect photoelectrons within $\pm$ 6 degrees of the plane, or 65% of the BZ in the ΓX direction, perpendicular to the chains. The results are summarized in the intensity maps of Fig. 2.13, for various values of the in-chain wavevector $k_{\|}$. The B and AB bands, both well visible at 0.38 ΓY, move towards the Fermi level as $k_{\|}$ increases, and the AB band disappears altogether as the zone boundary is approached. The perpendicular dispersion is very small ($<$ 0.1 eV) and consistent with an open Fermi surface. On

the horizontal plane ($k_\perp$=0), and for all values of $k_\parallel$, the intensity of band B is maximum and that of band AB is zero. Therefore the two bands have opposite reflection symmetries: *even* for B and *odd* for AB. These are, in the 2D limit, the symmetry properties of the bonding and antibonding combinations of 1D orbitals, discussed in Ref. [48]. Opposite reflection symmetries of the nested FS sheets are also consistent with the observed out-of-phase modulation of the lattice positions in adjacent chains [43, 49].

In order to map both bands along the **b** direction, we integrated the photoelectron signal over the full perpendicular angular window of the analyzer, taking advantage of the negligible perpendicular dispersion (Fig. 2.14(a)).

The B band does not differ from data collected with a narrow perpendicular angular acceptance in the horizontal plane, but in that case the dispersion of band AB could only be monitored when the **b** axis was not exactly horizontal. A remarkable aspect of the data is the absence of a well defined Fermi surface in the metallic phase. The closest approach to the Fermi level is near $\pi/2b$ (AB) and $Y = \pi/b$ (B), and both bands have 'shadow' replicas beyond those points. The replica of the AB band is well visible in the perpendicular cuts (at 0.58 and 0.72 ΓY) of Fig. 2. Strong shadow bands were also observed in 1D Peierls system $(TaSe_4)_2I$ [40] but not as clearly, due to the smaller energy separation between analogous bonding and antibonding conduction bands in that compound.

In the Peierls scenario of the CDW formation in $K_{0.3}MoO_3$, the momentum separation between the nested AB and B Fermi surface sheets determines the CDW wavevector [44]. It is not possible to determine Fermi level crossing points from Fig. 2.14(a). We used instead momentum distribution curves (MDCs), i.e. momentum-dependent constant-energy cuts. The MDC extracted immediately below E_F (Fig. 2.14(b)) shows four distinct peaks connected in pairs, within the experimental accuracy, by $Q_{CDW} = 0.75\pi/b$, consistent with scattering data. Similar values of Q_{CDW} have been reported [11, 47], but the individual Fermi wavevectors - $k_F^{AB} = 0.61\pi/b$; $k_F^B = 0.86\pi/b$ (Ref. [47]) or $k_F^{AB} = 0.59\pi/b$; $k_F^B = 0.89\pi/b$ (Ref. [11]) - are somewhat different. The origin of these differences is not clear.

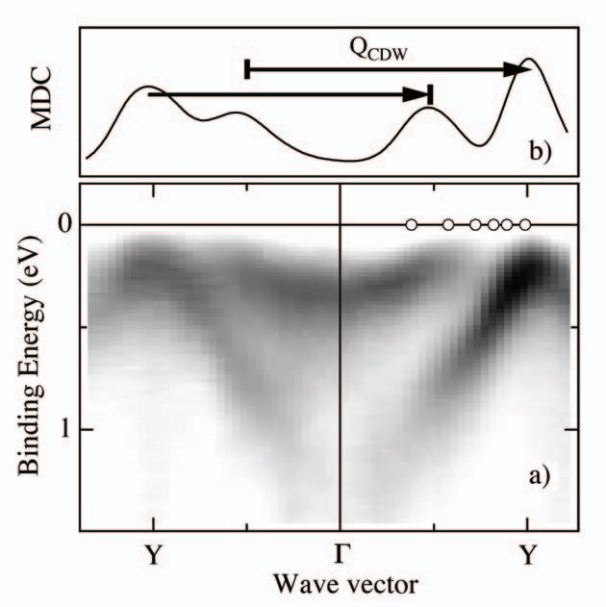

Fig. 2.14: (a) ARPES intensity map showing the band structure along ΓY (T=180 K, $\hbar\omega$=21 eV). The open symbols mark the k locations corresponding to the maps of Fig. 2.13; (b) Momentum distribution curve (MDC) extracted from (a) at ϵ_b=30 meV ($\Delta\epsilon_b$=60 meV), showing the alternate nesting of the FS sheets.

The symmetric intensity distribution (Fig. 2.13) and dispersion (Fig. 2.14(a)) rule out spurious effects, and give us some confidence in the accuracy of our data.

MDCs measured at various binding energies near the zone boundary (Fig. 2.15) show a main peak for $k < \pi/b$, and a weaker one at an approximately symmetric location in the second zone, from the 'shadow' band. Approaching E_F the two features converge towards $k = 0.4\mathring{A}^{-1}$, or $0.96\pi/b$. A detailed analysis of these curves is difficult due to the varying intensities, and the interfering effects of umklapps from the lattice and CDW potentials, acting respectively

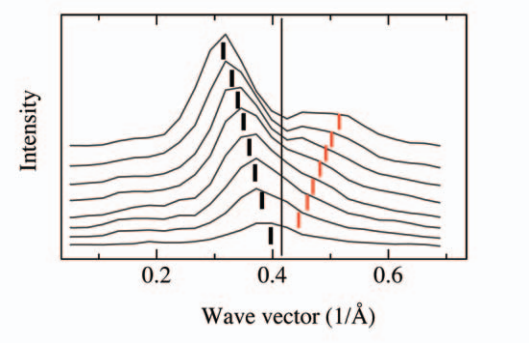

Fig. 2.15: MDCs extracted at different binding energies ($\Delta\epsilon_b$=30 meV) near the Y zone boundary. The dashed lines are guides to the eye (T=180, $\hbar\omega$=21 eV).

at $k = \pi/b = 0.415\mathring{A}^{-1}$, and at k_F^B = 0.4 $\mathring{A}^{-1}$. The existence of a shadow replica of the AB band around k_F^{AB}, clearly unrelated to the lattice periodicity, demonstrates that scattering on the CDW potential is certainly important.

The Peierls transition

In a mean-field theory, the CDW transition removes the entire Fermi surface - or leaves at most small pockets due to imperfect nesting in 2D or 3D - below T_P. This simple description does not apply to the blue bronze. In the metallic phase the dispersing spectral features remain well below the Fermi surface, forming a 'pseudogap', which is broader than the optical pseudogap [39] and whose origin needs to be clarified. A careful analysis reveals a temperature dependence associated with the Peierls transition at the high-energy end of the spectra. This is illustrated in Fig. 2.16(a,b) by ARPES maps collected at 210 K and 75 K, near the maximum of the B band. At 210 K, while the main band feature is at finite binding energy, a very small but finite intensity 'spills over' beyond E_F. The MDC measured at the Fermi level at T_P (Fig. 2.16(c)) exhibits a Lorentzian lineshape, the

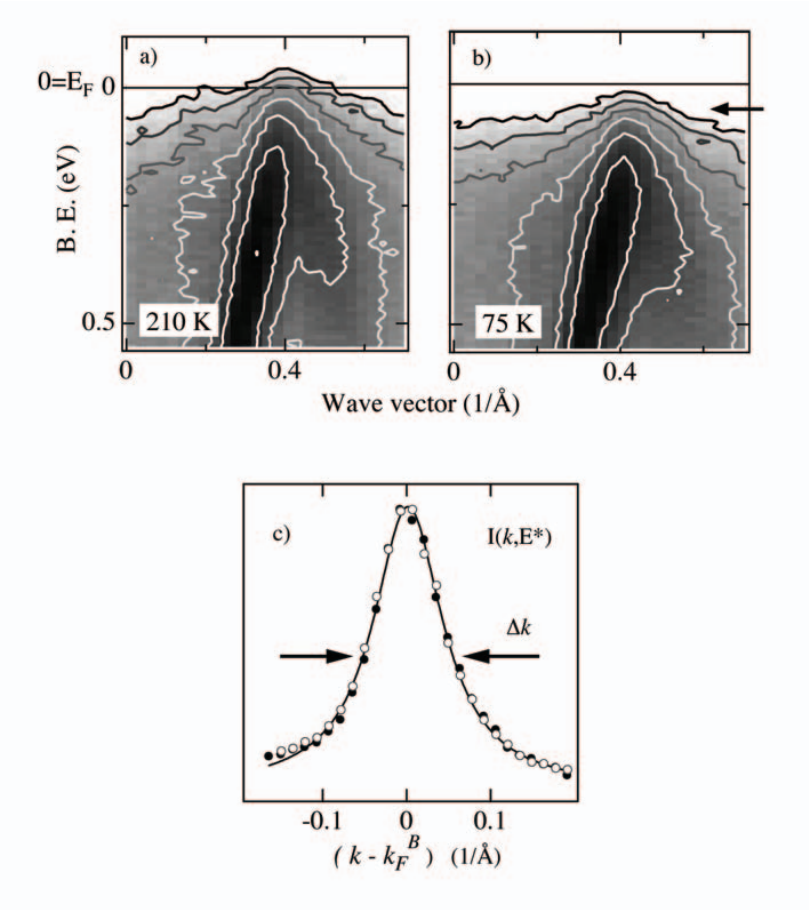

Fig. 2.16: ARPES intensity maps along ΓY at T=210 K (a) and T=75 K (b). A logarithmic intensity scale was chosen to enhance the small signal near the Fermi level. Lines of constant intensity are indicated. (c) MDCs extracted at the Fermi level at T = 180 K (full circles), and at ϵ_b=60 meV (arrow in (b)) at T= 60 K (empty symbols). The solid line is a Lorentzian fit with FWHM=0.1 *Å*

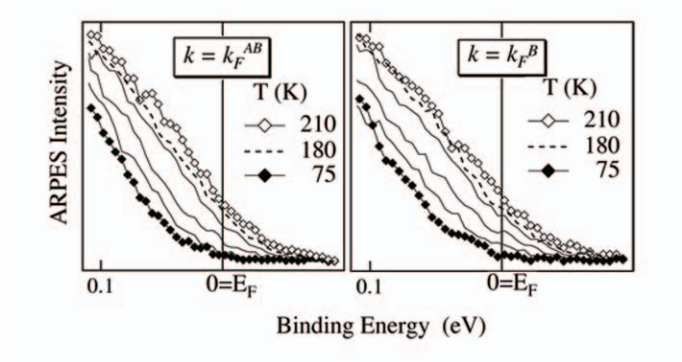

Fig. 2.17: Temperature evolution of the leading edge of spectra measured at k_F^B and at k_F^{AB} between T=210 K and T=75 K.

typical fingerprint of a QP. By analogy with $(TaSe_4)_2I$ [16], we take this as the spectroscopic evidence of a 'hidden' Fermi surface.

The Peierls transition affects both conduction bands, as shown by spectra measured near E_F at both Fermi wavevectors (Fig. 2.17). Below T_P the leading edges of both bands progressively shift to higher binding energies, until a true gap is formed. The temperature evolution of the two bands is consistent with Ref. [11] and substantiates the accepted scenario requiring that both pairs of FS sheets are involved in the formation of the CDW state. It would be difficult to obtain from Fig. 2.17 a quantitative description of the changes occurring through the CDW transition, without making specific assumptions on the lineshape. Following our analysis of the Peierls transition in $(TaSe_4)_2I$ [16] we used instead MDCs measured across the transition. The starting point is the MDC measured at E_F and T_P, which exhibits a Lorentzian lineshape. Below T_P both the intensity and the lineshape of the MDC are preserved if the cut is performed (Fig. 2.16(c)) at a higher binding energy $\Delta(T)$. Fig. 2.18(a) shows that $\Delta(T)$ behaves as a phenomenological order parameter for the transition, and saturates below $T \sim 100$ K to $\Delta_0 = 60$ meV, consistent the Peierls (half-) gap value from transport and optics [39].

Pre-transitional fluctuations have been invoked [50] as a possible origin of the reduced spectral intensity at the Fermi surface in the normal state of Peierls systems. From the BCS relation $2\Delta_0 = 3.57\ T_{MF}$, and from an analysis of the CDW dynamics [43], one obtains $T_{MF} \sim 320$ K in $K_{0.3}MoO_3$. We have already pointed out [16] that fluctuations alone cannot explain the peculiar ARPES lineshape of 1D Peierls systems. In a fluctuating pseudogap scenario, spectral intensity is removed within an energy of the order of the Peierls gap below E_F, and the pseudogap evolves into a real gap below T_P. If fluctuations in the CDW state [51] are neglected, the spectrum merges with the mean-field spectrum in the $T = 0$ limit. This is clearly not the case here, since the ARPES pseudogap scale is much larger than the Peierls gap, but fluctuations do have a measurable effect on the spectrum. This as illustrated in Fig. 2.18(b), where the ARPES intensity at the Fermi surface $I(k_F^B, 0)$ is compared with the spin susceptibility from Ref. [38]. The increase of χ_{spin} above T_P reflects the progressive filling-in of the pseudogap in the metallic phase. Within the experimental uncertainties $I(k_F^B, 0)$ exhibits the same temperature dependence, and therefore also reflects the temperature dependent pseudogap.

This conclusion is not incompatible with the unusual lineshape nor with the opening of a Peierls gap below T_P (Fig. 2.18(a)). As discussed below, the suppression of QP spectral weight is largely a consequence of interactions, but fluctuations above T_P further reduce the intensity at E_F. The QP DOS is therefore pseudogapped, and only when long-range coherence is established below T_P, can a real gap develop.

The spectral lineshape and the nature of the quasiparticles

The results of the previous sections establish the existence of band features and of characteristic fingerprints of the Peierls transition in $K_{0.3}MoO_3$. However, the dispersing peaks fail to cross the Fermi level in the metallic phase, and their minimum binding energies are unrelated to the typical energy scale of the material, the Peierls gap Δ_0. The spectral linewidth ($\sim$ 0.4 eV) is also unusually large.

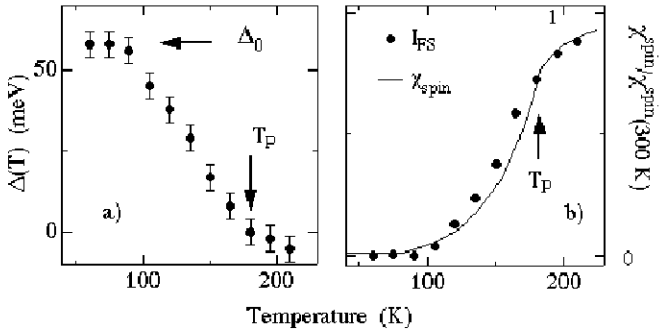

Fig. 2.18: (a) Single particle gap extracted from the MDC analysis. The shifts are measured from T_P=180 K. (b) The ARPES intensity I_{FS} at Fermi surface (ϵ_b=0, k=k_F^B) is superposed on the spin susceptibility from Ref. [38].

In a normal Fermi liquid, the width of a QP peak $\Delta E \sim \hbar/\tau$ is proportional to the inverse of the QP lifetime [52]. The condition for the QPs to be well defined excitations are $\Delta E < E$, and $\Delta \to 0$ at the Fermi surface (for $T \to 0$). Neither of these conditions is verified in $K_{0.3}MoO_3$, if we interpret the whole ARPES peak as a coherent excitation. However, a different interpretation is possible.

Strong interactions - or singular interactions in 1D - considerably modify the QP spectrum. They shift weight from the *coherent* QP peak, to the *incoherent* part of the spectrum, over an energy range which depends on the interactions, and which can be much larger than the intrinsic QP width. Strong, long-range electronic correlations in 1D can produce broad lineshapes compatible with experimental ARPES spectra [53]. This indicates a promising approach to 1D systems with dominant electronic correlations, like some organic Bechgaard salts [54], or the Peierls system TTF-TCNQ [35, 55] where electronic correlations are relevant at least on the TTF chains.

There is no evidence of strong electronic correlations in standard Peierls systems like $K_{0.3}MoO_3$ or $(TaSe_4)_2I$, where the occurrence

of a CDW ground state shows dominant electron-phonon (*e-ph*) interactions. An analysis of the CDW correlation length indicates a 'sizeable' *e-ph* coupling strength in $K_{0.3}MoO_3$. Optics data also point to a large *e-ph* coupling parameter ($\lambda \sim 1.2$) [51]. It is therefore tempting to interpret the broad ARPES lineshapes of $K_{0.3}MoO_3$ - and $(TaSe_4)_2I$ - as the spectra of electrons strongly coupled to the lattice.

We have discussed in a previous section the expected spectral properties, by analogy with the much simpler problem of a single electron coupled with a harmonic oscillator. The spectrum exhibits a 'zero-phonon' (or '0-0') peak and satellites at lower energy, under a common Poissonian envelope. The leading peak (adiabatic limit) corresponds to a transition between the ground states of the neutral and of the ionized system, and the satellites to transitions to vibrationally excited states. This *incoherent* part of the spectrum draws intensity from the '0-0' peak, which is progressively reduced as the coupling strength increases. The maximum of the spectrum occurs at an energy $\epsilon_b^* \sim \langle n \rangle \hbar\Omega$ below the leading peak, where $\langle n \rangle$ is the average number of quanta of vibration 'dressing' the electron in the ground state, and $\hbar\Omega$ is the frequency of the coupled mode. This simple model describes quite accurately the photoemission spectrum of a diatomic molecule like H_2 [6], and in that context the satellites are known as Frank-Condon satellites.

These simple considerations provide a qualitative guideline for the problem of a dense system of interacting electrons coupled to a lattice. Again we expect a progressive transfer of spectral weight from a 'zero-phonon' peak to the vibrational satellites with increasing coupling [56]. In a solid, of course, the interaction with a continuum of vibrational states plus various broadening mechanisms smear out the satellite structure, and only a (Gaussian) envelope will be observed. The weight of the leading peak reflects the progressively smaller overlap of the photohole with the real quasiparticle. For a sufficiently strong coupling the QPs can be described as small polarons, i.e. heavily dressed electrons which move coherently with the local lattice deformation. In this limit, the overlap between the QP and photohole wavefunctions is vanishingly small, and the coherent peak is exponentially reduced [57]. The essentially incoherent spectrum

peaks at $\epsilon_b^* \sim \langle n \rangle \hbar\Omega^*$ below the QP energy, where Ω^* is an average frequency. Guassian lineshapes - one for each valence band - fit well the spectra of the blue bronze.

From the energy separation between the QP energy - the Fermi energy at k_F in the metallic phase - and the maximum of the spectrum ($\epsilon_b^* = 0.2$ eV) we can attempt a rough estimate of the structure of the phonon cloud. Neutron data show a large phonon density in the 10 - 50 meV range [58], which yields $\langle n \rangle \sim 5 - 10$ phonons. A more accurate estimate would require an analysis of the coupling strengths. Namely, the relative importance of the low-frequency mode involved in the Kohn anomaly [43] - the precursor of the Peierls transition - and of the local, higher frequency vibrations, should be assessed. Even with these uncertainties, we conclude that heavily dressed electrons are compatible with the observed small QP weight in ARPES.

Optical data provide independent evidence for heavy QPs in $K_{0.3}MoO_3$. Fig. 2.19 shows the real part of the optical conductivity ($\sigma(\omega)$) for light polarized along the chain axis in the spectral range below 1 eV ($\sim 10^4$ cm^{-1}) at T = 200 K, in the normal metallic phase [39]. We can identify several distinct components, which are well reproduced within the phenomenological Lorentz-Drude approach [59]. The main feature at $2\Delta = 1000$ cm^{-1} ($\sim$120 meV) is associated with the Peierls pseudogap, which is already quite deep at this temperature. At low frequencies, the spectrum displays a rather complex behavior. Besides the peak ascribed to the quasi-pinned collective mode at about 3 cm^{-1}, there are two distinct zero-frequency modes. The first narrow Drude represents the collective contribution of the sliding CDW segments, while the second broad Drude reflects the response of the uncondensed quasiparticles.

The spectral weight of the QP component can be scaled with respect to the total spectral weight up to the threshold of the interband transition [16]. The integral[**?**] of $\sigma(\omega)$ leads to $\Omega_p^{tot} = 25600$ cm^{-1}, while spectral weight arguments applied to the QPs component yield $\Omega_p^{QP} = 4100$ cm^{-1}. From the conductivity sum rule we find:

$$(\Omega_p^{tot}/\Omega_p^{QP})^2 = (n^{tot}/n)(m^*/m_e) = 39. \tag{2.5}$$

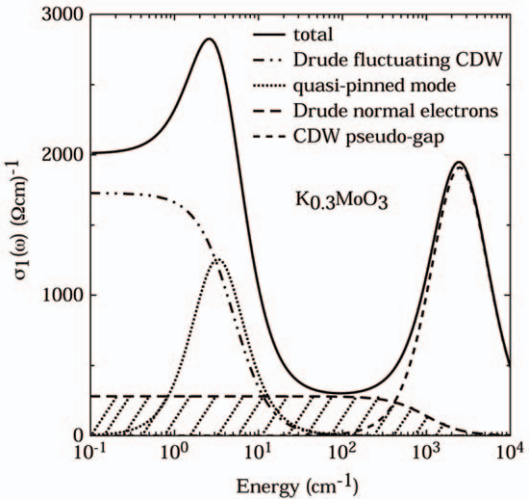

Fig. 2.19: Optical conductivity after the Lorentz-Drude model, based on the classical dispersion theory, reproducing the experimental data at T=200 K, along the chain direction (Ref. [39]). The components of the calculation are shown separately, and the contributions from the polaronic QPs is highlighted as dashed surfaces.

Notice that m^* is the effective mass of the polaronic QPs, and should not be confused with the - much larger - mass of the fluctuating CDW segments. Using $n/n^{tot} \sim 0.7$ at 200 K derived from the spin susceptibility [38], we obtain the polaron effective mass $m^* \sim 28m_e$. A comparison with the GGA band yields $m^*(200K) \sim 40m_{band}$.

In this polaronic scenario - and in a similar approach proposed in a different context in Ref. [60], the ARPES peaks of Fig. 2.12 do not represent the QPs, but the dispersing maxima of the incoherent spectrum. The suddenly created photohole 'sees' a frozen lattice, where it could disperse with a velocity corresponding to the non-interacting band. Therefore ARPES reveals the unperturbed bandwidth, rather than the exponentially narrowed polaronic bands. However, the photohole is rapidly slowed down by the lattice deformation. The result is a 'blurred' band, which can be interpreted as the superposition of narrow polaronic bands, where the spectral weight is concentrated along the frozen lattice dispersion. There is a clear distinction between bands, i.e. the k-dependent energy eigenvalues of the Hamiltonian, which are not directly observable, and the spectral weight which is a physical observable, measured in an ARPES experiment [40].

The MDCs of Fig. 5 indicate that the coherence length of the polaronic QPs is short ($l = 1/\Delta k \sim 11\mathring{A}$ when the experimental momentum resolution is taken into account), much shorter than the typical values (100 - 1000 $\mathring{A}$) for normal metals. A pump-probe experiment [61] which directly measured the QP response in the time domain, found a QP lifetime $\tau = 0.5$ ps. From the relation $l = v_{QP}\tau$, where v_{QP} is the QP group velocity, we obtain $v_{QP} \sim 2 \times 10^2$ ms^{-1}, which is about 2 order of magnitude smaller that the average velocity for the B band. Therefore the underlying polaronic bands are much narrower than the GGA or ARPES bands, consistent with the strong coupling scenario.

We also notice that the QP coherence length is considerably shorter than the in-chain CDW coherence length at 200 K ($\sim 50\mathring{A}$) [43], and temperature independent. On the other hand, the QP coherence length is quite close to the CDW period ($\lambda_{CDW} \sim 9\ \mathring{A}$). Qualitatively, this is what one expects in a local picture of the CDW, which ignores

the $2k_F$ instability and the nesting properties of the FS, and where long-range order is achieved with the condensation of local polaronic carriers. The coexistence of typical features of the weak-coupling Peierls scenario, and of a strong-coupling approach, shows that neither model of the transition is completely satisfactory. Apparently, after three decades of intensive investigation, a crucial issue of the physics of the blue bronze remains open.

Conclusions

We exploited high resolution ARPES to study the band structure, the properties of the quasiparticle states, and the consequences (gap, periodicity) of the CDW instability in the typical 1D Peierls system $K_{0.3}MoO_3$. We find conduction bands with strong 1D character, in good agreement with previous ARPES work and with recent GGA band structure calculations. By examining their symmetry properties, we verified the assignment of the topmost bands to bonding and antibonding combinations of 1D bands on adjacent chains. These bands support a 'hidden' Fermi surface with the nesting properties required by the Peierls model for the CDW transition. The temperature dependence of the spectrum at the estimated Fermi wavevectors exhibits clear signs of the transition. The spectra also exhibit signatures of a fluctuating CDW in the normal metallic phase.

The ARPES and optical spectral properties support strong electron-phonon interactions, and the formation of small polarons, with a large mass and a short ($\sim 10\AA$) coherence length. The similarities between $K_{0.3}MoO_3$ and $(TaSe_4)_2I$ suggest that strong interactions and heavy polaronic QPs could be generic features of 1D Peierls systems, a hypothesis which calls for an experimental verification in other related materials. The coexistence of strong interactions and non-local aspects requires a further scrutiny of the origin of the CDW transition, and a theory that extends the prevailing weak-coupling scenario. Finally, we notice that if the ARPES lineshape of Peierls systems is dominated by the strong *e-ph* coupling, the expected spectral signatures of the Luttinger or Luther-Emery liquid, namely spin-charge separation, would be confined at the leading edge of the broad

spectrum. Their direct observation could be prohibitively difficult due to the vanishingly small intensity.

Chapter 3

Quasi-1D insulator: the Mo red bronze $K_{0.33}MoO_3$

This chapter presents the first ARPES study on the red molybdenum bronze $K_{0.33}MoO_3$ and new optical reflectivity and high - temperature electrical resistivity measurements needed to elucidate the phototemission results. We find quasi-1D states in the insulating red bronze in good qualitative agreement with the available band calculations. Our findings underline the importance of defects which pin the Fermi energy level within the gap. I will present a detailed comparison to the metallic blue bronze $K_{0.3}MoO_3$, a related 1D Peierls conductor. The ARPES lineshape exhibits the same strong-coupling features in both compounds and we speculate that a similar mechanism could be at the origin of the gaps in both materials. Most of the results presented here were published in *Mitrovic et al, Phys. Rev. B,* ***69*** *035102 (2004)*

3.1 Introduction

Structural and electronic character of reduced dimensionality in most transition metal oxide bronzes $A_xM_zO_y$ (where M is a transition metal ion, and A some other metal ion, usually alkali or alkaline rare-earth

metal) sets off a multitude of interesting phenomena in their physical properties [19, 4].

In vanadium bronzes (M = V), 3*d* electrons responsible for the band formation are localized, making vanadium bronzes insulators at all temperatures. Tungsten bronzes (M = W), on the other hand, have delocalized 5*d* electrons making them metals. In molybdenum (M = Mo) bronzes we have a mid situation with the 4*d* electrons, accounting for the intricate differences among molybdenum bronzes. They offer unique opportunities to investigate low-dimensional metallic and insulating systems but with closely related structural and electronic properties.

The blue bronzes $A_{0.3}MoO_3$ (A = K, Rb, Tl) have recently generated a renewal of interest, being quasi-1D or 2D metals demonstrating superconductivity or Peierls instabilities towards low - temperature charge density wave (CDW) insulating state. Optics [39] and photoemission [17, 11, 47] studies of the potassium blue bronze $K_{0.3}MoO_3$ in particular, confirmed various aspects of the weak - coupling Peierls scenario, including the nesting properties of the Fermi surface and the occurence of pretransitional fluctuations, but also provided evidence for strong electron - phonon interactions [17].

The 1D molybdenum red bronzes $A_{0.33}MoO_3$ are insulators at all temperatures. The purple bronzes $A_{0.9}Mo_6O_{17}$ are 2D – with a "hidden" 1D character [20] and nesting [62, 63] – and exhibit metal-to-metal CDW instabilities, with the notable exception of the 1D Li purple bronze.

Photoemission on low-dimensional, and especially quasi-1D systems reveals many peculiarities [12]. In 1D conductors, the absence of the Fermi edge in momentum-integrated (PES) spectra, and unusually broad angle-resolved spectral line shapes, are clearly incompatible with normal 2D or 3D metals [27, 64, 65]. The anomalies observed point out the 1D correlation and possibly the theoretically predicted breakdown of the Fermi liquid paradigm in strictly 1D. In that respect we need to broaden our spectroscopic database on 1D materials. So far, the interest has been focused mostly on 1D conductors. Conventional "1D band insulators" were deemed less interesting, but this is not necessarily the case as seen in $(NbSe_4)_3I$.

Some features of optical and ARPES measurements on this semiconductor, namely the unusually small quasiparticle (QP) scattering rate, cannot be explained by prevailing models [66]. Quasi-1D band insulators are also a useful reference for the metallic systems, since the low-energy electron - hole excitations which destroy the QPs and lead to Luttinger liquid (LL), are "frozen" by the energy gap. The persistance of the peculiar line shapes in the insulators would set new constraints on the interpretation of the electronic properties of 1D materials.

Metallic $K_{0.3}MoO_3$ blue bronze manifests many of these peculiarities. In that respect a closely related insulating $K_{0.33}MoO_3$ red bronze proved to be an interesting study case. We have investigated the electronic structure and discussed spectral similarities of the two materials.

3.2 Structural and electronic properties

Red bronze crystallizes in a monoclinic (space group C2/m) structure, with lattice parameters $\boldsymbol{a}$ = 14.278 Å, $\boldsymbol{b}$ = 7.723 Å, $\boldsymbol{c}$ = 6.387 Å and β = 92.3°. As in all Mo bronzes, the basic building blocks are MoO_6 octahedra. In the case of the red bronze, four of the octahedra form two ReO_3-type chains, and the two more are encased in-between the chains. Such Mo_6O_{18} clusters are linked by corner sharing in [010] direction (along b axis) making one-cluster wide slabs, and along [001] direction in a shear-like manner, as shown in Fig 3.1. Layers that are formed in this way are held together by bonding of the oxygen from the cluster corners and K^+ ions located at the interstitial places between the layers.

The band structure of ReO_3 has been successfully adapted and applied to explain bonding in bronzes (see Fig 3.2). In the case of molybdenum bronzes, Mo 5s and 4d(e_g) orbitals, which result from the splitting of Mo 4d levels in the octahedral potential, combine with O $2p_\sigma$ orbitals to form a pair of sets of antibonding σ^* and bonding σ molecular orbitals. O $2p_\pi$ orbitals hybridize with the second part of Mo 4d split orbitals, the Mo 4d(t_{2g}) orbitals, to create antibonding π^*

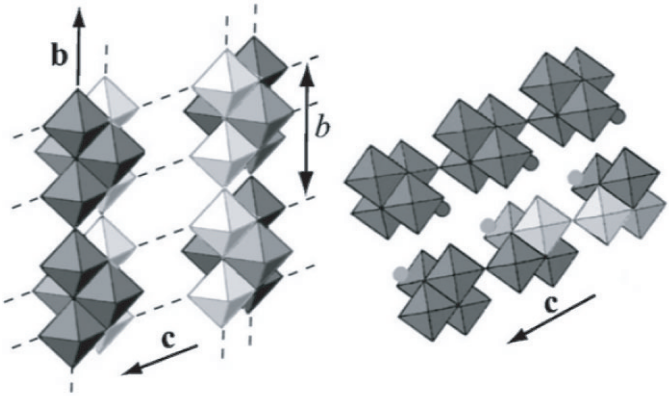

Fig. 3.1: Crystal structure of $K_{0.33}MoO_3$. (Left) Double chains of ideally undistorted MoO_6 octahedra run along the **b** axis. One such double chain (light shade) is shown split for clarity. (Right) View along the **b** axis, showing layers of clusters alternating with K layers along the **a** axis direction.

and bonding π molecular orbitals. The rest of the O $2p_\pi$ orbitals that cannot be bonded to t_{2g} orbitals, produce non-bonding p_π molecular levels. Above depicted molecular orbitals expand into bands when in the lattice of a crystal. Usually, the bonding bands and the non-bonding ones are filled and represent valence bands (called "O $2p$" bands), while π^* can become partially filled and thus may create conduction bands ("Mo $4d$" bands). The alkali atoms that join the layers donate their $4s$ electrons to fill these bands. These cations do not contribute in the band picture, since the empty $4s$ levels are to high in energy. In the case of red bronze, potassium atoms donate 2 electrons per Mo_6O_{18} cluster. One cluster carries two inequivalent sites for molybdenum atoms, the Mo(2) site inside ReO_3-type chains and Mo(1) site on the sides, but only Mo(2) sites have significant electron density.

Despite the essentially 2D structure, dominant intrachain interactions give the electronic structure a pronounced 1D character[67]. An ideal undistorted chain would be semimetallic, with a filled valence

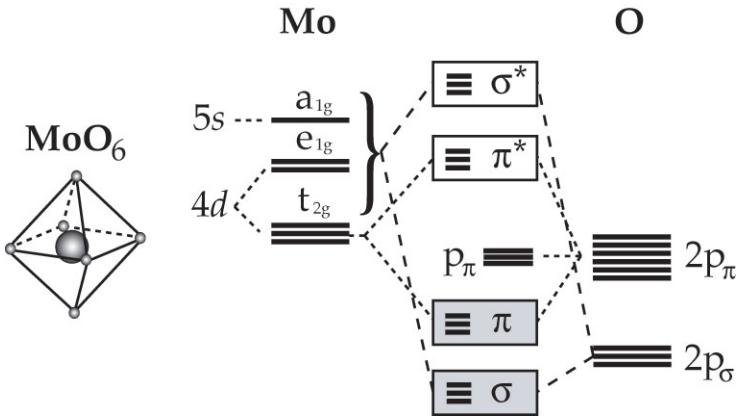

Fig. 3.2: A simple model of the band structure of $K_{0.33}MoO_3$ and $K_{0.3}MoO_3$ starting from the elementary MoO_6 octahedron.

and an empty conduction band degenerate at the zone boundary **Y**. In reality, the MoO_6 octahedra are distorted, with an alternation of long - long - short - short Mo-O bonds along the chain (see Fig 3.3). The distortion which is also periodic with periodicity b lifts the degeneracy, and the real red bronze is predicted to be a semiconductor with an indirect gap $\Delta \sim 0.1$ eV.

This is notably different from the blue bronze where a different arrangement of the MoO_6 octahedra leads to a partially filled bands which share the valence electrons. In this case, basic structural cluster contains two sets of adjecent inequivalent chains, instead of one, whose interaction gives rise to two bands of the opposite symmetry and ultimately opens a way for CDW formation.

$K_{0.33}MoO_3$ is insulating at all temperatures. The reported non-linear transport and a large maximum of the dielectric constant are analogous to CDW - related properties in the blue bronze[68, 69], but there are no structural indications of the CDW instabilities. Early interpretations of the origin of the gap in the red bronze suggested a correlation, Mott - Hubbard rather than a band gap. Slightly londer Mo - O bonds than those in the blue bronze would account for the

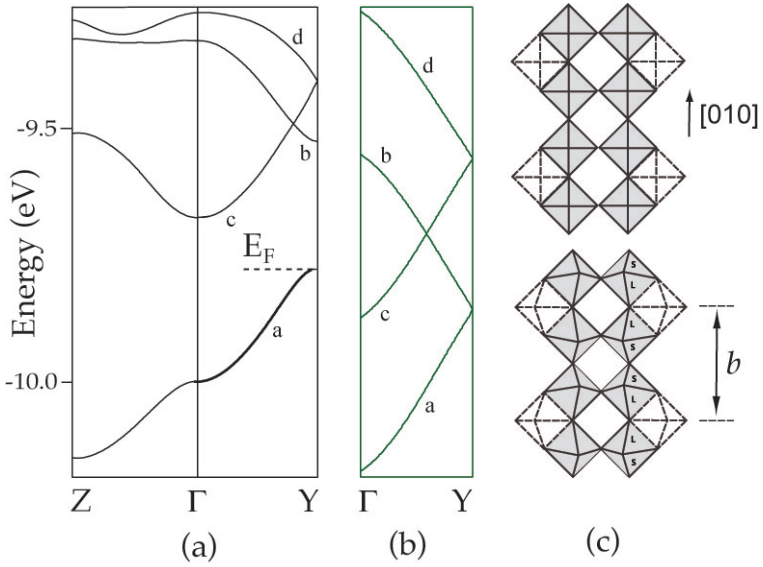

Fig. 3.3: (a) The bottom portion of the t_{2g} - block bands of the Mo_6O_{18}, for the real and (b) the hypothetical ideal undistorted structure. Adapted from Ref. [67] (c) MoO_6 chains with lines representing bond lengths. Top picture shows the ideal undistorted case, and the bottom one the real structure bond length alternation.

existence of a narrow band whose bandwidth would be smaller than the on-site Coulomb repulsion[70]. This picture is not supported by the band structure calculations which give similar bandwidths for the red and the blue bronze [67], nor by magnetic susceptibility and ESR data which indicate a very small spin density [71, 72]. The ARPES data presented definitely rule out the Mott - Hubbard scenario.

3.3 Experimental

Single crystals of $K_{0.33}MoO_3$were grown as described in Ref. [73] in the form of shiny red platelets, less than a millimeter thick, with surfaces of $\sim 3 \times 3$ mm^2 parallel to the crystallographic (100) planes

which contain the 1D chains. The crystals, oriented by Laue diffraction, were cleaved in ultrahigh vacuum at a base pressure of 10^{-11} mbar to expose clean surfaces. We utilized a He discharge lamp ($h\nu$ = 21.2 eV) and a Scienta ESCA 300 hemispherical analyzer with the energy and momentum resolution ΔE = 10 meV and Δk = 0.04 $\AA^{-1}$. The ARPES results were reproduced with repeated cleaves and on different samples. The Fermi level position was determined from the spectrum of a polycrystaline Ag sample, with an accuracy of $\pm$ 0.5 meV. By varying the photon intensity we exclude the possibility of charging effects influencing the spectra, as could be expected for a poorly conducting material. A thin layer of conducting graphite was applied around the edges of the crystal to serve as a pool of electrons for the surface during the irradiation.

The resonant photoemission data were taken at LURE, Super - ACO, at the SU3 Swiss-French beamline. The energy resolution, depending on the photon energy was around 50 meV. Measurements were taken at normal emission angle.

Electrical resistivity measurements were performed by a standard four - point contact technique in the temperature range between 300 and 800 K. The optical reflectivity was measured on a specimen from the same batch, in the spectral range from the far-infrared up to the UV for light polarized along and perpendicular to the chain direction, using the equipment described in Ref. [66]. The Kramers-Kronig transformations were then applied in order to obtain the optical function, namely, the real part $\sigma_1(\omega)$ of the optical conductivity. To this end standard extrapolations, at low and high energies, were employed. Because of the insulating state of the red bronze, the reflectivity was extrapolated to a constant value in the limit of zero frequency. Resistivity measurements were performed by N. Barišić at EPFL, and the optical measurements by L. Degiorgi at ETH Zurich.

3.4 Results and discussion

Longitudinal dc electrical resistivity (Fig 3.4) exhibits a semiconducting temperature dependence with two distinct regions: an activated

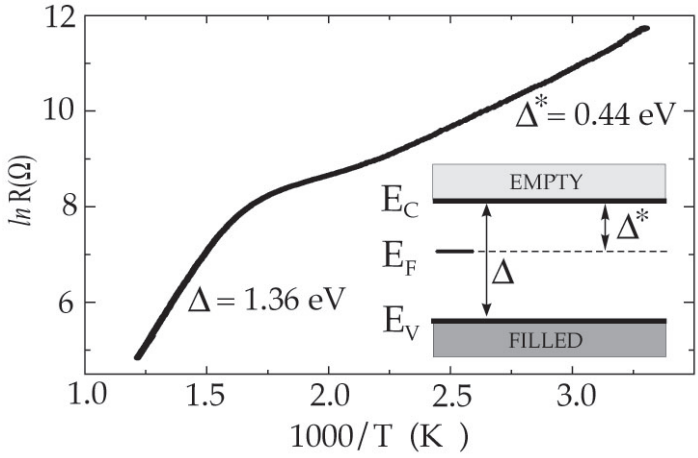

Fig. 3.4: Temperature dependence of the dc electrical resistance measured along the chain direction. The observation of two distinct gaps (Δ and Δ^*) is consistent with midgap states which pin the Fermi level as sketched in the inset.

behavior with a gap Δ = 1.36 eV above ∼600 K, and a region with a smaller gap Δ^* = 0.44 eV below ∼450 K. No simple activated behavior can be defined at intermediate temperatures. We interpret the largest gap value as the full semiconducting gap, and the smaller as evidence for midgap states (see the inset of Fig 3.4). Their contribution is washed out at high temperature, but becomes dominant at lower temperatures, where the number of carriers thermally excited across the fundamental gap rapidly drops. This assignment is supported by the ARPES data discussed below.

Figure 3.5 shows $\sigma_1(\omega)$ at 300 K up to the visible spectral range for light polarized along the chain axis. Our optical data agrees with previous results obtained on samples from a different origin [74]. The dominant feature is the rather broad absorption centered at about 8000 cm^{-1} (∼1 eV), which we ascribe to the optical insulating band gap. Another remarkable feature is the shoulder on the low frequency side of the gap at about 5500 cm^{-1} (∼0.68 eV), which again we

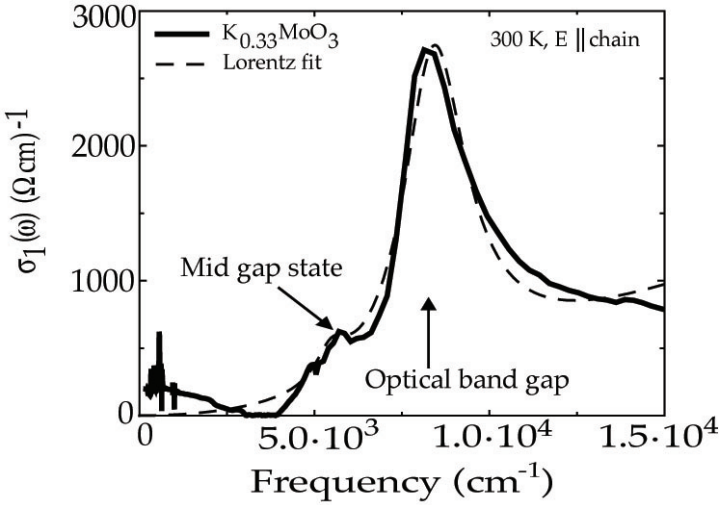

Fig. 3.5: Real part of the optical conductivity measured at room temperature and with the light polarized along the chains.

attribute to 'mid-gap' states. Furthermore, the optical gap absorption comes rather close to the squared root singularity, as expected for a 1D band insulator [66]. On the high frequency tail of the gap feature, $\sigma_1(\omega)$ approximately decays with the $\sigma_1(\omega) \propto \omega^{-3}$ power-law, indicative of a rigid lattice where only Umklapp scattering off the single-period lattice potential is possible. We should however warn that this frequency dependence can be verified only over a limited spectral range, because of the vicinity of overlapping high energy electronic interband transitions.

Resonant photoemission data shown in Fig 3.6 show all valence band features located below 10 eV. The broad part of the spectra from 9 to 4 eV are the "O $2p$" bands while the "Mo $4d$" band is located below just below 2 eV. Excitation photon energy was varied from 20 to 90 eV. We notice, for all molybdenum bronzes inherent enhancement of the "O $2p$" bands, especially in the peak at 6.5 eV, at the energy of Mo $4p \Rightarrow 4d$ absorption edge. The lower-binding energy end of the

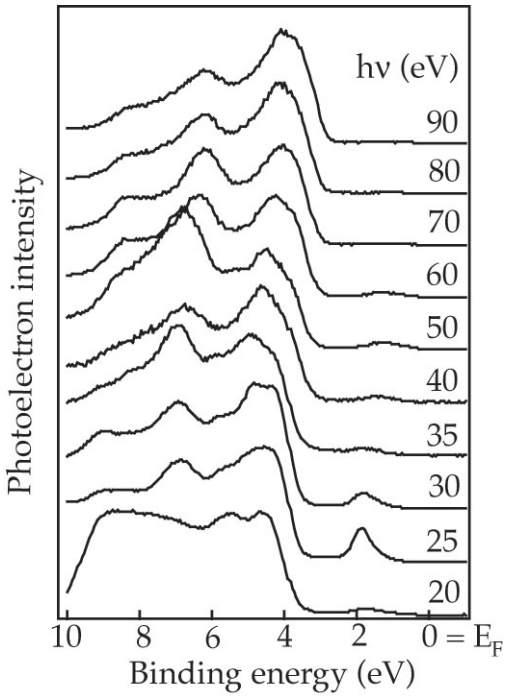

Fig. 3.6: Resonant PES curves measured at room temperature and normal incidence.

"O $2p$" bands is not affected, as could be expected, since it is mainly composed from non-bonding p_π bands. We observed a resonance in the Mo 4d band at about 25 eV. The choice of the He I line for the ARPES measurement is thus well suited. We do not observe the defect-induced peak that appears in molybdenum bronzes around 2 eV.

The ARPES intensity map of Fig 3.7 shows dispersion along the 1D chain direction, with a minimum at Γ (E_B = 2.1 eV) and maxima (E_B = 1.3 eV) at the Brillouine zone boundaries Y($\pm\pi/b$). At with the BB case, there is only one valence band in the red bronze, and its periodicity coincides with the periodicity of the lattice. The shape

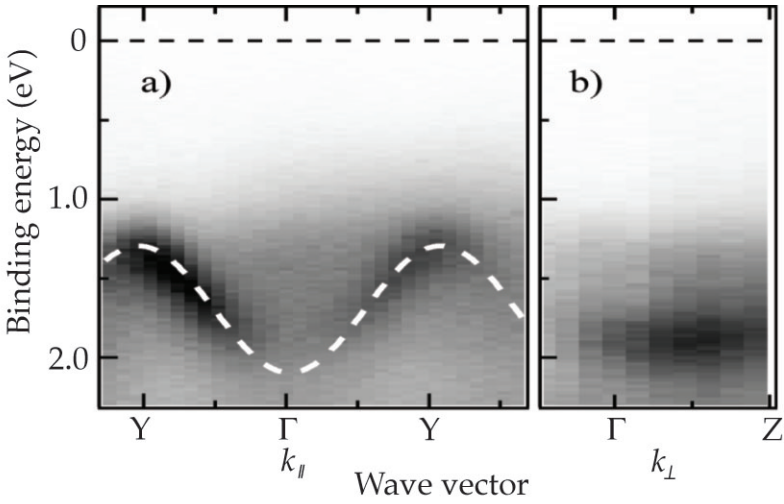

Fig. 3.7: ARPES intensity maps of $K_{0.33}MoO_3$ (a) parallel and (b) perpendicular to the 1D chain direction. The dashed cosine line is a guide to the eye.

of this band, and its total bandwidth ΔE = 0.8 eV are similar to those of the bonding (B) valence band in the blue bronze [17], but the whole band is rigidly shifted by $\sim$1 eV towards higher binding energies. Consequently, the narrow-band Mott scenario of Ref [70] is not confirmed by the experiment. The measured dispersion of 0.8 eV is four times larger than in the tight binding calculation, but we do not consider this discrepancy as serious. A similar difference in the case of blue bronzw was recently eliminated by subsequent first-principle calculations [44], and we expect that improved band calculations would be able to reproduce the ARPES dispersion.

Weaker "shadows" of the main band extend beyond the zone boundaries into the second Brillouin zone. Shadow bands were also observed in the blue bronze and in other 1D Peierls system such as $(TaSe_4)_2I$ [16]. While the periodicity of the bands is a "geometrical" property, simply reflecting the periodicity of the atomic arrangement, the intensity of the ARPES features, and the gap size, depend on

the strength of the periodic – lattice or CDW – potential [40]. In Peierls systems like $(TaSe_4)_2I$ – and possibly also in $(NbSe_4)_3I$ – the broad energy gaps and well visible shadows reflect lattice distortions associated with the CDW. The spectral features of Fig 3.7 bear clear resemblance to those cases. The simple presence of the hump octahedra (Fig 3.1) along the chains doubles the 'geometrical' periodicity and defines the size of the BZ. They also impose strong constraints on the inner octahedra and induce a deformation of the chain, which provides the necessary periodic potential to open a wide gap.

The experimental gap is considerably larger than the calculated value, because tight-binding calculations intrinsically underestimate the Mo '*d*' - O '*p*' antibonding interactions which remove the degeneracy of the perfect chain [75]. This raises questions about the nature of the distortion. Steric considerations are obviously important, but electronic contributions may also play a role. The periodicity of the distortion coincides with that of a hypothetical Peierls distortion ($2k_F = 2\pi/b$), suggesting the possibility of an instability with a very high critical temperature. This hypothesis is appealing because it would help draw a common picture for all 1D Mo bronzes, and justify the transport anomalies [68, 69].

The dispersion perpendicular to chains is extremely small. The map of Fig 3.7(b) refers to a line in *k*-space parallel to the *c* axis, for a fixed wavevector ($k_{||}$ = 0.4 ΓY) along the chains. The dispersion is <0.05 eV, smaller than the calculated value (ΔE∼ 0.1 eV, Ref [67]). Therefore, red bronze appears even more one-dimensional than expected form the tight binding description. This conclusion should be tested against state-of-the-art first principle calculations, and is moderated by the known surface sensitivity of ARPES. The ARPES dispersion correctly follows the bulk periodicity, but small rearrangements (relaxation) at the surface could still influence the overlap of the atomic orbitals, and affect the measured dispersion.

ARPES only probes occupied electronic states, and therefore cannot directly measure the full gap. A further complication comes from the peculiar 1D line shape. ARPES data on related 1D compounds like the blue bronze and $(TaSe_4)_2I$, but especially on insulating $(NbSe_4)_3I$, have shown that identifying the peak position with the QP energy

would lead to a gross overestimation of the energy gaps. Phenomenologically it was found that the spectral leading edge is a good indicator of the QP energy both in metallic and in the insulating phases [17, 16]. This indicates a strong QP renormalization, and strong interactions. We have determined the energy position of the spectral leading edge (Fig 3.8) at the top of the band (Y point), and obtained $E^* \sim 1$ eV. This is then the estimated energy separation between the Fermi energy E_F and the valence band maximum E_V as sketched in Fig 3.4 inset. A similar value is obtained from a comparison with the spectrum of the blue bronze measured at the Fermi wavevector k_F in the metallic phase, where the QP energy coincides with E_F. Still, again an energy shift of $\sim$1 eV would be necessary to superpose the two lineshapes.

ARPES and transport data can be reconciled with the assumption that red bronze is not an intrinsic semiconductor, and that the Fermi level position in the gap is determined by impurity (or defect) states, as sketched in the inset of Fig.1. Impurity states, located at $\sim$0.4 eV below E_C, pin the Fermi level, and define the gap Δ^* seen in resistivity. These states could be associated with oxygen vacancies, off-stoichiometry, or other defects, and specific calculations are required to clarify their nature. Clearly, as seen from repeated experiments they are not confined to the surface region probed by ARPES. A very small density of impurities, well below the limit of detectability by ARPES, would be sufficient to pin the Fermi energy and determine the low-temperature behavior of the resistivity. The only direct effect on ARPES would be the observed shift of the top of the valence band to an energy position (Δ - Δ^*)$\sim$1 eV below E_F. Such a scenario also agrees, at least qualitatively, with the optical spectrum (Fig 3.5). Such a quantitative discrepancy between ARPES and optics in not uncommon for 1D materials, e.g. the organic Bechgaard salts [66]. Somehow more puzzling is the disagreement between optics and transport. In 1D systems with a broken symmetry ground state, the optical gap tends to be larger than the transport gap because of the energy dispersion, which is more and more important with increasing deviations from the perfect nesting [76]. We do not have a firm explanation for the observation an optical gap *smaller* than the

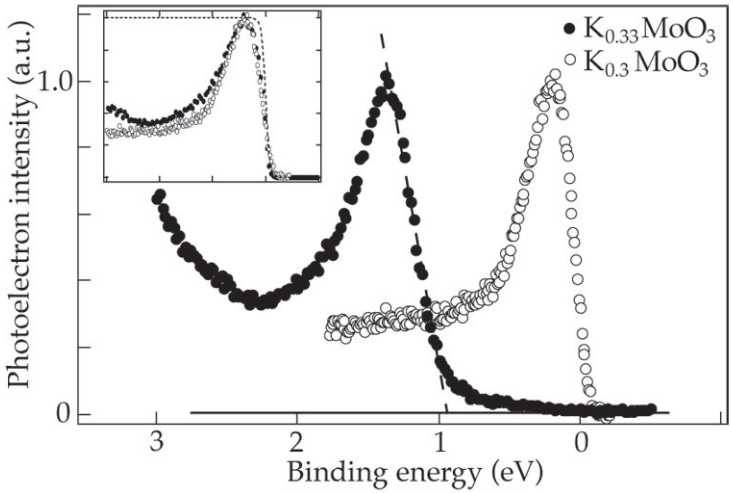

Fig. 3.8: Comparison of the spectral line shapes of the blue bronze (Ref. [17]) and the red bronze measured, respectively, at the Fermi wave vector and at the top of the valence band. The dashed line shows the extrapolation of the leading edge. Inset figure shows the same spectral lines with the red bronze line shifted on top of the blue bronze line and multiplied by the Fermi cutoff function.

transport gap in the red bronze. We might speculate on a general ground that such differences are due to different curvature of the band probed by the two experiments, or due to the different spectral response functions involved. Since only the optical measurements are both sensitive and contactless, we cannot exclude that this discrepancy somehow reflects intrinsic differences between the bulk and the outermost surface layers. On the other hand, the robustness of the position of the pinned Fermi level suggests that the stoichiometry of the cleaved surfaces is well preserved and does not put in question ARPES results. We can at least presume that the charge neutrality is equally preserved at the surfaces of other metallic bronzes.

Finally, we briefly consider the spectral lineshape. The analysis of the experimental ARPES lineshapes is a subject of interest in the

debate on the relevance of the Luttinger liquid (LL) for real 1D compounds. The observation of the spectral consequences of charge-spin separation predicted by theory would strongly support this scenario. Circumstantial evidence for the LL has been obtained from data on the 1D bronzes $Li_{0.9}Mo_6O_{17}$ [34], and on artificial nanostructures [13], but alternative interpretations of the data are possible [14]. In particular, in the presence of strong electron-phonon interactions, the resulting spectral weight renormalization could totally mask the LL features [52]. This might well be the case in Peierls materials such as the blue bronze, where a polaronic (Gaussian) line shape provides a satisfactory description of the spectra. A comparison of the spectra of Fig 3.8 demonstrates that the line shape of the metal and of the insulator are essentially identical, if the high-energy cut by the Fermi function in the BB spectrum is taken into account. Both lineshapes are much too broad ($\Delta E \sim 0.5$ eV) to be interpreted as the spectra of normal QPs. On the other hand, the polaronic scenario provides a rationale for the unusual width and for the discrepancy between peak and leading edge energies in terms of phonon sidebands, representing the dressing of the heavy (polaronic) QP. This is also supported by optical measurements. A detailed analysis of the optical conductivity indicated a large electron - phonon coupling constant $\lambda \sim 1.2$ in the blue bronze [51], and from a comparison we infer a similarly large coupling in the red bronze. In summary, similarities in the spectral properties of the red and the blue bronze ARPES suggest that the dominant factor in both materials is the coupling of electrons to the lattice deformations. This, in turn, lends further support to the interpretation of the nature of the static deformation in terms of an electronic instability.

3.5 Conclusion

We have presented the first ARPES measurement of the insulating red bronze $K_{0.33}MoO_3$. ARPES maps show a strong one-dimensional semiconducting character as we find one band which is significantly dispersive only in the direction of the chains. This dispersion is

comparable to the one of the bonding band in the structurally similar metallic blue bronze $K_{0.3}MoO_3$. The semiconducting gap on the other hand was found to be much larger than expected from previously reported studies.

To clarify the situation, we have performed new optical reflectivity measurements and the DC electrical resistivity measurements in the high-temperature region, i.e. above the room temperature. Transport measurements show two distinct activation regions that we associated with two energy levels. We argue that only at the higher temperatures we depopulate the valence band and see the real semiconducting gap of the RB. At lower temperatures, observed conductivity comes from thermally excited electrons that populate a level within the gap. The existence of a mid-gap state is further confirmed by the optical reflectivity measurement. This density of states within the gap, though small to be seen in the photoemission spectra, is sufficient to pin the Fermi level and in consequence make the ARPES band appear to be at a higher binding energy.

In order to bring together quantitatively ARPES and transport data, we assumed that the mid-gap states represent a donor level. In that case, we find that the leading edge of the ARPES energy distribution curve taken at the Brillouin zone edge is the part of the spectrum that corresponds to the top of the valence band and defines the energy gap. This comes as little surprise since we find that the spectral lineshape is virtually identical to the one taken at the Fermi wavevector in the metallic blue bronze.

We have previously found that QP spectra in blue bronze are renormalized due to the strong interaction between electrons and the lattice. Spectral weight is taken from the QP peak which then falls at the leading edge of the spectrum. In that case it is the leading edge, since it represents the QP, which crosses the Fermi level in the metallic state. Clearly, the same spectral lineshape in RB indicates that the coupling of electrons to the lattice has a similar effect in this material and justifies the leading edge association with the valence band position.

Chapter 4

Transition metal trichalcogenides: $ZrTe_3$ and $TaSe_3$

This chapter presents ARPES results on two transition metal trichalcogenides with quite different electronic properties: $ZrTe_3$ and $TaSe_3$. The $ZrTe_3$ part is in preparation for publication while most of the text on $TaSe_3$ has been published as a part of the paper *Perucchi A, Sondergaard C, Mitrovic S. et al*, Eur. Phys. J. B **39**, 433-440 (2004).

4.1 Introduction

The transition metal trichalcogenide group of materials belongs to a larger group of layered chalcogenide materials that are build from chain-like structures. Different rearrangements of the shared structural units between the closely related compounds often result in radically different electronic properties. Correlation effects in such materials are highly sensitive to the particularities of the material.

Two compounds were selected for this work that have never been previously studied by ARPES, mainly due to the unavailability of good quality samples that are of sufficient size for ARPES experiments. $ZrTe_3$ is one of the the rare materials that exhibit a charge density wave instability and superconductivity. Interestingly, the instability is not correlated with the structural 1D chain. $TaSe_3$ is closely related to $NbSe_3$, a material that undergoes two CDW transitions, yet it does not display any instability. These two materials are an excellent study case for the general spectral properties of Peierls systems, since both differ from a classical 1D Peierls system, but are still closely related.

4.2 Structure and electronic properties

The family of layered transition metal trichalcogenides with MX_3 (M = transition metal; X = S, Se, Te) composition is structurally predominantly one-dimensional in character. The basic structural unit of these materials are chains of transition metal ions surrounded by chalcogen anions in a distorted trigonal prismatic chain. While in group 4 transition metal compounds (M = Ti, Zr, Hf) there exists only one kind of chain in the structure, in the case of group 5 compounds (M = V, Nb, Ta) there exist several [77]. The electronic structures of the 4-MX_3 and 5-MX_3 compounds are also different; the former are mostly semiconductors and the latter conductors. Certainly the most notable member of the metallic group 5 family is $NbSe_3$ which was the first inorganic linear-chain material where CDW transitions were found [4].

This simple categorization fails to demonstrate the complexities of the actual electronic properties of these trichalcogenides. $NbSe_3$ is indeed a metal, but this picture does not make it any different than for instance TaS_3, yet they exhibit very different behaviors. While they both undergo two charge density wave transitions, TaS_3 ends up in an insulating ground phase, and $NbSe_3$ stays a metal. Ionic picture fails in the case of $TaSe_3$ as well, as this compound is actually semimetallic. $ZrTe_3$ is no less puzzling. It is the only 4-MX_3 compound known to be metallic [78]. Also, despite being a linear chain compound, it is rather

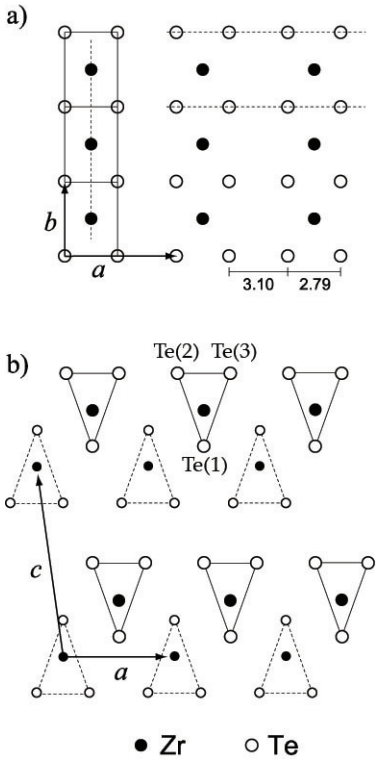

Fig. 4.1: (a) The (001) surface of $ZrTe_3$. Dotted lines follow the Zr and Te chain direction on the left hand side and the right hand side schematics, respectively. (b) Projection view perpendicular to the chains. Two layers of chains (different circle size) are displaced by b/2.

a quasi-2D conductor with only a weak anisotropy in the out-of-plane direction. Obviously, to correctly describe the electronic properties of these materials we have to take into account the orbital overlap and the particularities of the Fermi surface.

Both $ZrTe_3$ and $TaSe_3$ crystalize in the monoclinic space group $P2_{1/m}$. Since there could be different structural variants for the same

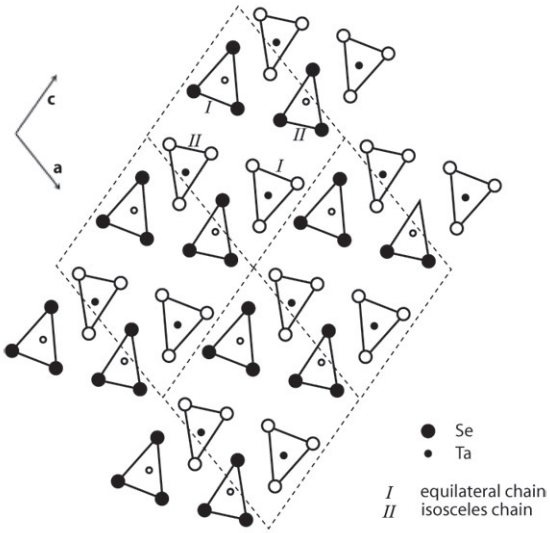

Fig. 4.2: The crystal structure of $TaSe_3$.

symmetry, there was some initial confusion about the structure of $ZrTe_3$. Fig. 4.1 illustrates the crystal structure of $ZrTe_3$. The lattice constants at room temperature are $\mathbf{a} = 5.898$ Å, $\mathbf{b} = 3.927$ Å, $\mathbf{c} = 10.103$ Å, and the monoclinic angle is $\beta = 97.81^\circ$ [79]. The basic structural unit of $ZrTe_3$ are the trigonal prismatic chains spanning along the $\boldsymbol{b}$ direction. There are two chains in the monoclinic unit cell connected by inversion symmetry and separated by $b/2$. These double layers (a-b plane) weakly bond through Van der Waals force, providing easy (001) cleavage planes. The electronic structure of all trichalcogenides depends greatly on the intra- and interchain distances. As can be seen in Fig. 4.1 two of the chalcogen atoms – here denoted Te(2) and Te(3) – in the triangle form a pair, while the intrachain bonding distance to the other chalcogen atom on the neighboring chain is somewhat bigger than the interchain bonding distance giving the oxidation scheme $Zr^{4+}Te^{2-}(Te_2)^{2-}$.

The structure of $TaSe_3$ was first determined by Bjerkelund et al

[80]. There are four chains per unit cell (**a** = 10.4 Å, **b** = 3.5 Å, **c** = 9.8 Å and $\beta = 106^\circ$) that span along the **b** axis. They form a-c layers that define the cleavage plane. Isosceles and equilateral chains alternate within each layer (Fig.4.2). In the ionic picture the oxidation scheme is thus $Ta^{5+}Se^{2-}Se_2^{2-}$.

In both $TaSe_3$ and $ZrTe_3$we can see that the cross-chain links are quite important, and therefore we should expect a more two-dimensional than one-dimensional electronic properties.

4.3 Screening of one-dimensionality in $ZrTe_3$

$ZrTe_3$ is an ideal system to study the coexistence of one-dimensionality and non-one-dimensionality. It is a linear chain conductor with a very low electronic anisotropy contrasted to its structure. $ZrTe_3$ undergoes a charge density wave transition at $T_{CDW} = 63$ K and a superconductivity transition at $T_c = 2$ K. Hence $ZrTe_3$ represents an interesting material to study the interplay between low-dimensionality, electronic structure, superconductivity and charge density wave transitions.

Materials that exhibit both the charge density wave and superconducting low-temperature phases are few and therefore very interesting study cases; other examples are $2H$-$NbSe_2$ [81] and $Lu_5Ir_4Si_{10}$ [82]. Superconductivity in $ZrTe_3$ was first observed by Takahashi et al in 1983 who suggested that the superconductivity was not bulk-like but of filamentary nature [83]. This was confirmed in recent investigation which also found T_c to vanish with increasing pressure [84].

The CDW transition was first proposed by Takahashi et al. after observation of anomalies in components of the electrical resistivity, the Hall coefficient, and Young's modulus at the transition temperature [83, 85]. Resistivity measurements revealed a quasi-2D character with only a weak anisotropy in the out-of-plane direction. Moreover, the anomaly in resistance was only seen in the compenents perpendicular to the chains (see Fig. 4.3) and perpendicular to the surface, indicating a peculiar situation in $ZrTe_3$: that the CDW nesting vector had no component along the chains of Zr ions! Shortly after

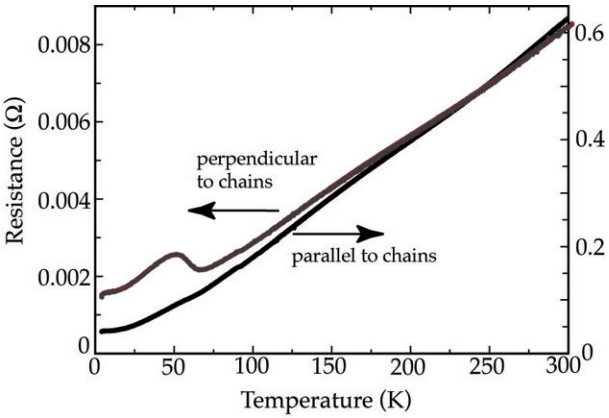

Fig. 4.3: Electrical resistance of $ZrTe_3$ measured in the direction (black) and perpendicular to chains (red). Resistivity measurements were made to check the quality of the crystals.

this scenario was corroborated by an electron diffraction investigation which found at 50 K a superstructure modulation with periodicity [**?**]:

$$\mathbf{q} = 0.93 \cdot \mathbf{a}^* + 0.33 \cdot \mathbf{c}^* \tag{4.1}$$

After the determination of the correct crystal structure [86], some confusion in the interpretation of varous experimental results was lifted. Both Stöwe et al [79] and Felser et al [87] calculate the electronic structure and the Fermi surface in good agreement with each other. Both groups find the optimal nesting conditions to be in agreement with the electron microscopy measurements.

The problems with the CDW picture do not stop there. In a recent (2002) pressure dependent resistivity measurement it was found that T_{CDW} rises with pressure while T_c drops [84]. This is in disagreement with the band structure calculations which would suggest that T_{CDW} should drop with increasing pressure since the interchain Te-Te interaction should increase with the increasing pressure. Additionally, in a neutron diffraction experiment [88] no superstructure was seen

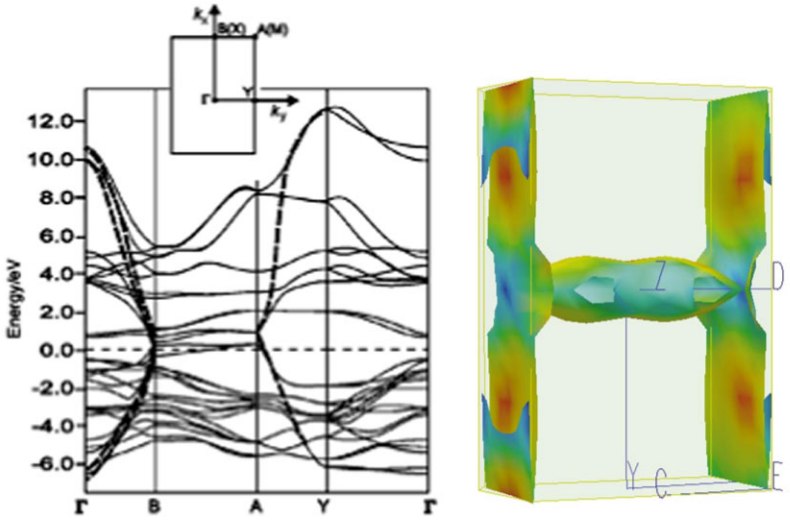

Fig. 4.4: (Left) Band structure in the a*-b* plane. (Right) Fermi surface of $ZrTe_3$. Red regions correspond to high Fermi velocity, and the blue ones to low Fermi velocity., both from Ref. [87]

by the Felser group which they argue is reasonable for the big real space unit cell. Furthermore, they find that the interchain Te-Te distance decreases (and the intrachain Te-Te distance increases) as the temperature is lowered – again in disagreement with the CDW picture where the opposite trend would be expected.

4.3.1 Theoretical electronic structure

Recent electronic structure calculations [79, 87] find that the interchain Te-Te interactions are responsible for the metallicity of $ZrTe_3$. The three bands intersecting the Fermi level give rise to a Fermi surface consisting of three branches: i) a central part around Γ and two planar sheets along the B-D direction (see Fig. 4.8). The combined effect of these branches gives $ZrTe_3$ a rather isotropic in-plane

conductivity and weak inter-layer transport ($\sigma_a = \sigma_b = 10\sigma_c$).

The central part around Γ and along the $\mathbf{a}^*$ direction is a cylinder-shaped branch originating from the intersection of a band with predominantly Te(1)($5p_y$) character along the Γ-Y direction and a Zr($4d_{y^2}$) band along the Γ-Z direction. It is expected that the observed metallic conductivity along the chain direction, is associated with this portion of the FS. A cut through this branch is a cigar-shaped FS for $k_z = 0$

Additionally, two nearly parallel sheets of FS can be found along the B-D direction of the BZ, parallel to the $\mathbf{b}^*$ direction. These two sheets originate from two bands of almost pure Te(2)/Te(3)($5p_x$) character.

4.3.2 Experimental

The $ZrTe_3$ samples, their preparation, structure and the propereties of the transition metal trichalcogenides have been reviewed in Ref. [89] and the phase diagram of the zirconium-tellurium system has been mapped by X-ray powder diffraction and differential thermal analysis [90]. Our samples, prepared by the chemical transport method, appear as shiny platelets of about 2 × 2 mm size. The samples were characterized and oriented by X-ray Laue diffraction. The samples were cleaved at low temperature and under ultra high vacuum conditions.

The photoemission experiments were performed on the NIM-4 beamline at the Synchrotron Radiation Center (SRC). ARPES spectra have been acquired with a Scienta SES-2002 electron energy analyzer. The analyzer was mounted with the entrance slits in the horizontal plane. The overall energy and angular resolution chosen for the experiment were better than 10 meV and 0.5 degrees, respectively. The Fermi surface mapping was performed at the undulator-based SGM-3 beamline at the storage ring ASTRID in Aarhus [91]. In brief, the beamline, which is receiving its light from the undulator of ASTRID, covers an energy range from 14 eV to 140 eV with a resolving power better than 15000. The electron spectrometer is mounted on a goniometer inside the chamber and can be moved in order to map electron distribution curves at various emission

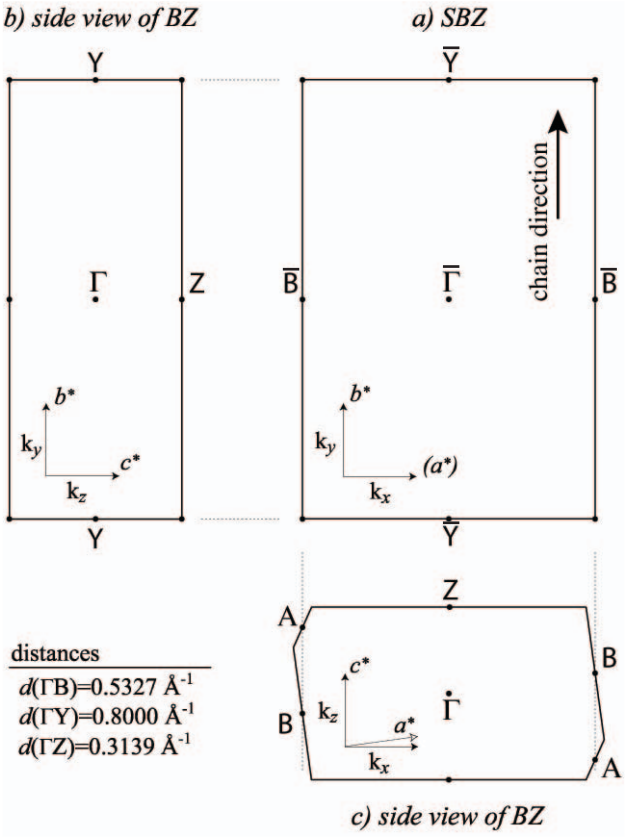

Fig. 4.5: (a) The surface Brillouin zone (SBZ) of $ZrTe_3$ together with views of the bulk Brillouin zones perpendicular to the surface and (b) parallel or (c) perpendicular to the chains.Choosing $\mathbf{a}, \mathbf{b}$ along x, y in a cartesian system the reciprocal lattice is spanned by $\mathbf{a}^* = (2\pi/a, 0, -2\pi/a\frac{1}{\tan\beta})$, $\mathbf{b}^* = (0, 2\pi/b, 0)$ and $\mathbf{c}^* = (0, 0, 2\pi/c\frac{1}{\sin\beta})$. On the other hand, the reciprocal surface lattice is spanned by two perpendicular vectors $\mathbf{g}_1 = (2\pi/a, 0)$ and $\mathbf{g}_2 = (0, 2\pi/b)$.

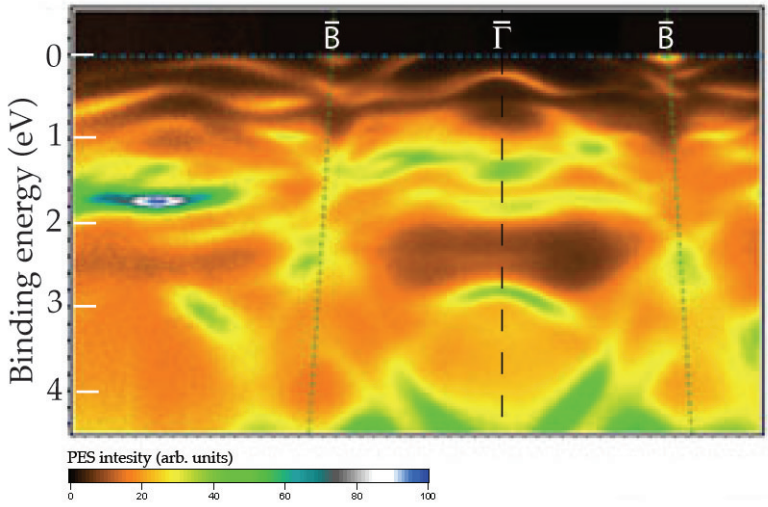

Fig. 4.6: ARPES intensity map of $ZrTe_3$ in the direction perpendicular to chains.

angles. The spectra presented here were measured with a total energy resolution better than 50 meV. The angular resolution was about 0.7°.

4.3.3 Band mapping along high-symmetry directions

Fig. 4.6 shows a map of the photoemission intensity acquired along the direction perpendicular to the chains and in the plane of cleavage. The rich electronic structure is built by Te 5*p* states partially hybridized with Zr 4*d* orbitals. Two of these bands, marked *C* and *B*, intersect the Fermi level. Their origin is dissimilar: band *C*, whose orbitals are mostly Te p_y, generates the cigar-like FS branch, whereas band *B*, rising from Te-Te p_x interactions, sets up the quasi-1D FS. The $2k_F$(B) is close to the zone edges, and supports in part the nesting wavevector (0.93$\mathbf{a}^*$). It turns out that band B is almost flat in the **b** direction and these states could indeed display a good nesting condition for setting up a CDW instability. In various off-

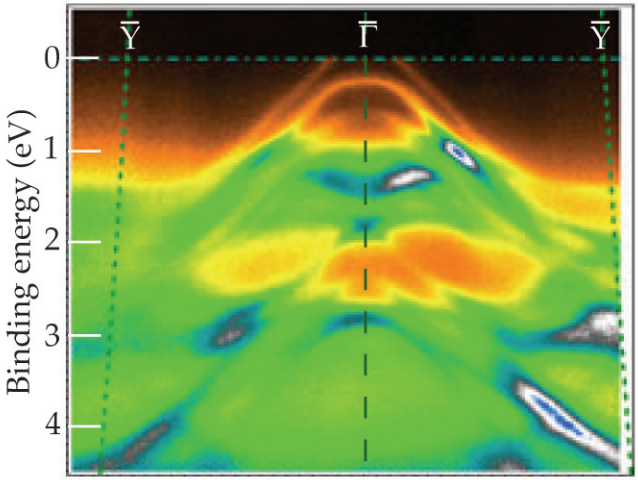

Fig. 4.7: Band mapping of $ZrTe_3$ in the direction of chains.

high-symmetry direction scans we observe that k_F(B) is always very near to the edge of the first Brillouin Zone (BZ). This means that this band is not dispersing much in other directions, supporting the theoretical sheet-like Fermi surface [87], giving strong evidence that the CDW transition is stabilized by the nesting of these highly degenerate states.

Fig. 4.7 displays the map of the photoemission intensity acquired along the direction parallel to the chains. One notices a band with Fermi level crossings at both sides of Γ. This band is the same one which make the 'C'-crossing in the perpendicular direction. In other words: the horizontal cut through the Fermi surface generated by the C band is a circle. The shape of the this inner Fermi surface is discussed in the following. The evident two-/three-dimensionality of the bands requires more detailed investigation to make a more thorough comparison with the theoretical structure.

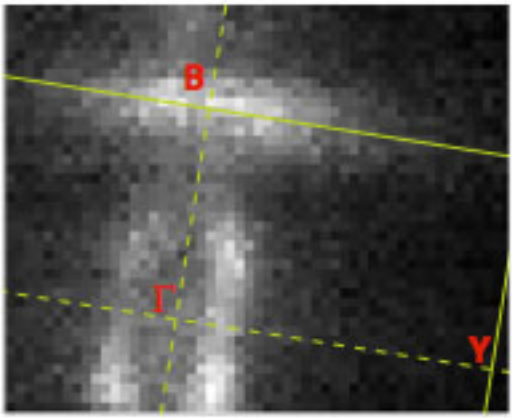

Fig. 4.8: A cut through the Fermi surface in the Γ-Y-B plane. The grayscale shows intensity of the signal with white being the maximum.

4.3.4 The Fermi surface

We have performed several experiments to closely investigate the shape of the Fermi surface. Firstly, we present in Fig. 4.8 the FS taken in the Γ-Y-B plane covering almost one quarter of the surface Brillouin zone. The map was obtained in the following way. A grid of 2279 evenly distributed points covering an irreducible quartet of the surface Brillouin zone was defined. From this set of points in *k*-space, the corresponding angles in real space were calculated, and then 2279 EDC's were measured (motorized and automatized movement of the analyzer) in those directions. The EDC's covered the region of the Fermi level, and hence a photoemission map of the Fermi surface could be constructed by mapping only the intensity at the Fermi level onto the grid in the surface Brillouin zone. In this case the energy window was E=[E_F-0.05,E_F+0.05] eV, the photon energy was 24 eV, and the temperature was -150°C. The grayscale representation of intensity has white as maximum and black as zero intensity. The figure shows both the cigar-like part and the sheet through the B point

in agreement with theory. The map details the inner Fermi surface shape, specifically its predicted "8"-like shape in the Γ-Y-B plane. The regions of high intensity in certain spots on the inner surface and near the B point shows the regions with low Fermi velocity in qualitative agreement with Fig. 4.4 (Right).

For the purpose of completeness, we mention that we have also taken photon energy dependent measurements of the inner Fermi surface parallel to chains. In this way we hoped to determine its shape around the Γ point and in the Y-Γ-C plane. While theory describes it as a circle, our measurements, though not conclusive, do not see the change in the Fermi momentum for different photon energies. This suggests that the Fermi surface is more a 2D tube-like rather than a 3D surface.

In the limited portion of the spanned reciprocal space investigated, we did not observe the gap formation. A more dense sampling of the FS will be necessary to monitor the occurrence of imperfect nesting. Such a delicate issue calls for future investigations on this material.

4.3.5 Spectral line shape and electron-phonon coupling

The strength of the electron-phonon coupling, which is the driving force for the formation of the charge density wave ground state, can be determined from the spectral line width of the quasiparticle at the Fermi level as discussed earlier in this thesis.

A strong peak of emission is seen in the vicinity of the B point (Fig. 4.9 (Left)). A closer inspection reveals that this peak is in fact a small electron pocket which is symmetric around the B point. We have verified this by symmetrizing spectra (not shown here). Its bandwidth is around 50 meV. The limited resolution (angular and energy) of the spectrometer and the relative broadness of the peak make this small band difficult to resolve. In the Fig. 4.9 we have compared the line shapes at the B point at two temperatures - below and above the CDW transition. One notices immmediately that the EDC acquired at 100 Kelvin is somewhat broader than the EDC acquired at 20 Kelvin. We also notice that this conductor shows properties that are not typical

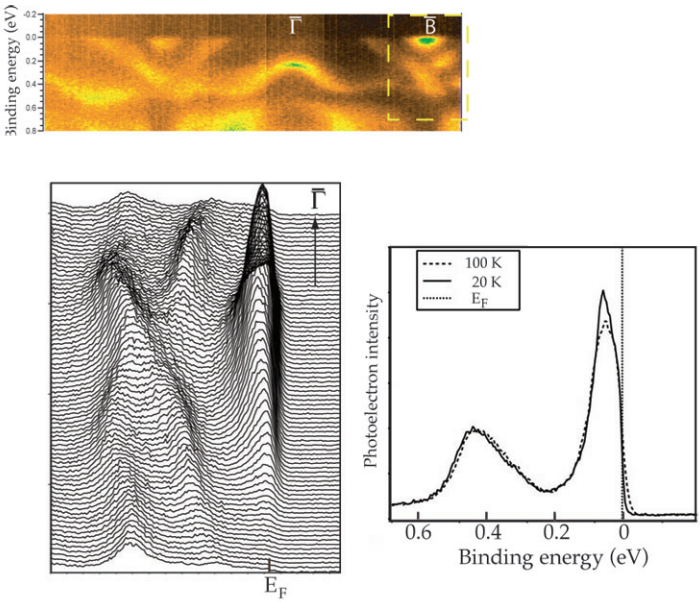

Fig. 4.9: (Left) EDCs around B point in a region marked on the intensity map above the plot. (Right) Comparison of spectra obtained at 20K and 100 K at the B point.

of other Peierls compounds. In contrast with $(TaSe_4)_2I$ and $K_{0.3}MoO_3$ (see introductory chapters), the line shape of $ZrTe_3$ spectra reflect the presence of 'well behaved', light quasiparticles. This apparent contradiction is explained by the evidence that $ZrTe_3$ is not a truly quasi-1D system. It holds both quasi-1D and quasi-2D electronic states. The 1D sheets are not decoupled and the cigar-like part of the Fermi surface between the sheets affects deeply the electronic properties, screening the one-dimensional character.

For a quantitative determination of the line width a Shirley background was subtracted from each spectrum and then a lineshape function was fitted. In the simple picture one would expect the lineshape to be a Lorentzian. However, due to the small electron

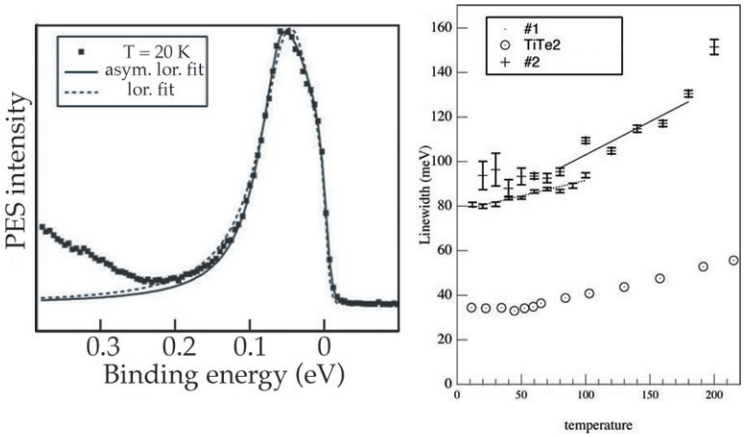

Fig. 4.10: Comparison of different line shape fits. Asymmetric lorentzian fit was chosen to determine the linewidth ploted on the left. Two different sets of measurements show similar behavior, linear at higher, and leveling off at lower temperatures. The same is ploted for $TiTe_2$, a model Fermi liquid, for comparison.

pocket and *k*-parallel sampling the lineshape is broadend towards the low binding energy side. In order to simulate this situation we fit the spectra with an asymmetric Lorentzian. At the bottom of the band the higher binding energy part of this function is a good measure of the intrinsic line width. A comparison of the fits is shown in Fig. 4.10.

In Fig. 4.10 the extracted values of Γ (FWHM) are shown as a function of temperature. Data for the model Fermi liquid 1T-$TiTe_2$ [52] is included in the figure for comparison.

In the case of $ZrTe_3$ the linewidth decreases with decreasing temperature and there seems to a linear relationship. The temperature evolution of the linewidth shows that the excitations in $ZrTe_3$ can be described as "well-behaved" quasiparticles. An estimation of the coupling parameter in the linear region gives $\lambda = 0.50 \pm 0.05$. Further investigation is necessary, however, to confirm the relevance

of this value for the material. More specifically, the realization of a nesting vector uncorrelated with the chains indicates a possibility of an anisotropic electron-phonon coupling constant [92]. The same measurements and analysis should therefore be done at other points on the Fermi surface to make a more general statement on the coupling.

4.3.6 Conclusion

Our measurements confirm the theoretical Fermi surface. It consists of parallel 1D sheets and a cigar-like surface in-between. The actual CDW nesting vector is difficult to determine for its specific 3D orientation uncorrelated with the 1D chain. The position of the 1D sheets corresponds to the predicted vector. We do not see any signs of the metal-insulator transition. There are two possible explanations: either there is a mechanism similar to the one in some transition metal dichalcogenides that prevents the observation of the instability, or we need to make a more thorough investigation of the Fermi surface to find the part of the Fermi surface where the gap opens.

Spectral characteristics are not typical for Peierls conductors. Fermi level crossings are present and the excitations fit in the light quasiparticle description. The particularities of the Fermi surface obviously provide for the good electron-phonon coupling screening.

4.4 Quasi-1D semimetallic $TaSe_3$

4.4.1 Electronic properties

$TaSe_3$ is a layered 5-MX_3 compound. Like in other trichalcogenides, the low-dimensional structure comes from the basic strucutral units – prismatic chains containing the transition metal (see Fig. 4.2). The band structure was calculated in 1979 by Bullett [94] and in 1990 by Canadell [93] (see Fig. 4.11). In $NbSe_3$, a closely related material, valence electrons fill up the bands in such a way that there are four bands left crossing the Fermi level. These bands are almost dispersionless in the directions perpendicular to chains, but due to

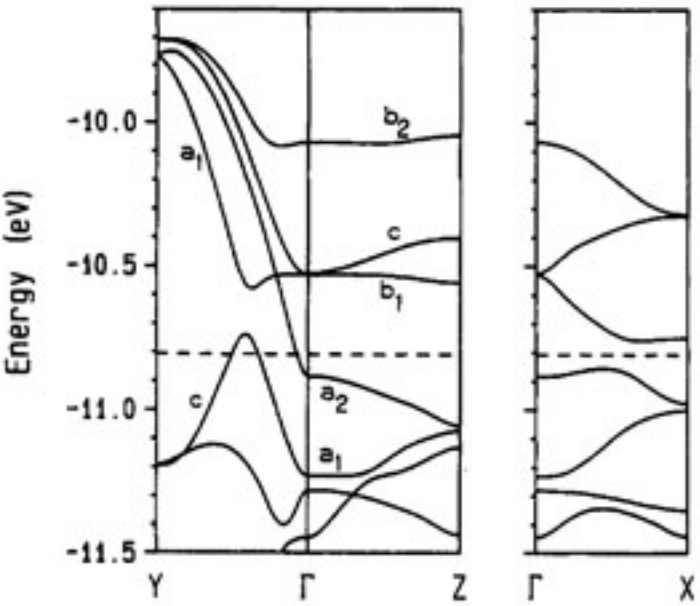

Fig. 4.11: Band electronic structure for the 3D lattice of $TaSe_3$ from Ref. [93]. The dashed line refers to the Fermi level.

large in-chain d_{z^2} overlap, they disperse considerably along the chain direction. A one-dimensional instability is therefore expected in this material. In $TaSe_3$, on the other hand, the valence electrons fill up completely available bands, and a semiconducting behavior is expected. However, the orbital overlap of Ta $5d$ and Se $4p$ accounts for the final semimetallic character. $TaSe_3$ is thus an anisotropic conductor, of very low conductivity (see Fig. 4.12) and falls into the category of poorly understood conductors named "bad metals" [95]. Transport properties are summarized in [96]. Optical properties are also anisotropic, but as expected, do not show the signatures of a CDW transition [97]. However, short range fluctuating CDW segments are detected in the electrodynamic response as well as in the dc-transport.

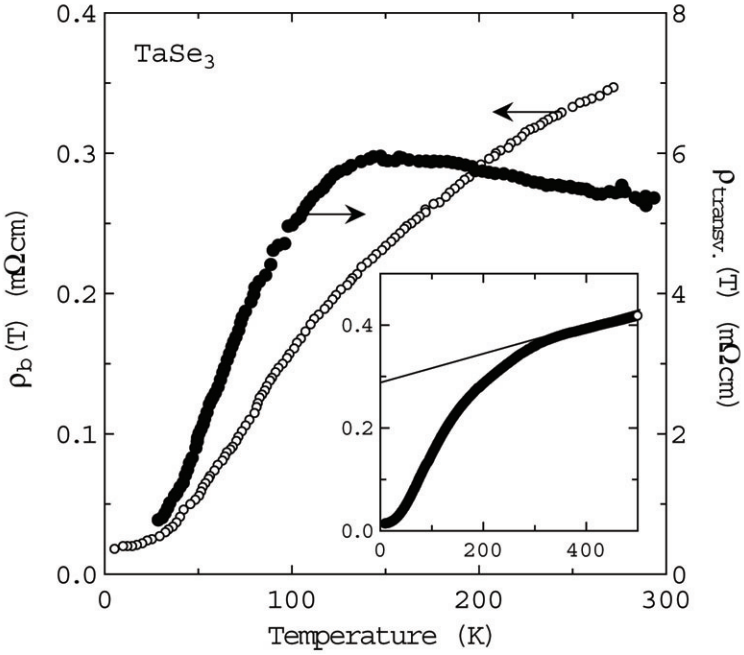

Fig. 4.12: Temperature dependence of the resistivity along the transverse and chain b-axis. The inset emphasizes the hightemperature linear behaviour of ρ_b(T).

4.4.2 Experimental

The key to the successful photoemission experiments was the growth of sufficiently large crystals of $TaSe_3$. The crystals were grown in our laboratory by direct sublimation of elemental Ta and Se with a slight excess of Se closed in an evacuated quartz ampoule between 660° C and 700° C for a period of ten weeks [98]. Photoemission measurements were performed in Lausanne and at the Wisconsin Synchrotron Radiation Center (SRC), with total experimental energy resolution ΔE = 15 meV, and momentum resolution Δk = 0.015 $\mathring{A}^{-1}$. The single crystal samples were cleaved in situ in ultra-high vacuum

(10^{-11} mbar range) to expose clean a-c planes containing Ta - Se chains. Scanning tunneling microscopy measurements [99] have shown that cleavage produces atomically ordered surfaces. However, the thickness of the sample is very small which, with best care, regularly produces a "wavy" surface with a tendency to brake along the chains that lowers the overall momentum resolution. The results of band mapping were highly reproducible.

4.4.3 Core level results

First, we will take a look at the core level spectra. The XPS technique is particularly sensitive to the chemical environment. The Se 3*d* core level spectrum (Fig. 4.13(Above)) indicates the presence of inequivalent sites. It exhibits 3 distinct peaks instead of the expected spin-orbit split (j = 3/2; 5/2) doublet. After subtraction of a standard Shirley background, we decomposed it into the sum of a main spin-orbit doublet and a shifted and attenuated replica. Rather than using a standard analytical expression with free parameters (width, asymmetry) [3] we self-consistently determined the lineshape from the data. The common lineshape of each spin-orbit component was forced to fit the leading and trailing edges of the experimental spectrum, where the overlap with other components is small. The spin-orbit doublet was then constructed using the statistical branching ratio $BR = 2/3$ and an energy separation Δ_{SO} compatible with tabulated values (0.8–0.9 eV) of the Se 3*d* spin-orbit splitting. The fit was performed by varying Δ_{SO}, BR as well as the energy shift ΔE and intensity ratio R of the main doublet and replica. An excellent fit is obtained for the following set of parameters: BR = 0.65, Δ_{SO} = 0.85 eV, ΔE = 0.73 eV and R = 0.5. The latter value supports the proposed bonding conguration for the Se ions: $3(Se)^{2-}$ in the equilateral chain and $(Se)^{2-}$ + $(Se_2)^{2-}$ in the isosceles chains, with an overall 2:1 ratio between the two different sites. Notice also that the signal from the minority $(Se_2)^{2-}$ sites correctly appears at higher binding energy, as a consequence of the smaller local electron density. Similarly, the Ta 4*f* core level spectrum (Fig. 4.13(Below)) does not exhibit a simple (Lorentzian, Voigt or Doniach-Sunjic) [17] lineshape, suggesting the

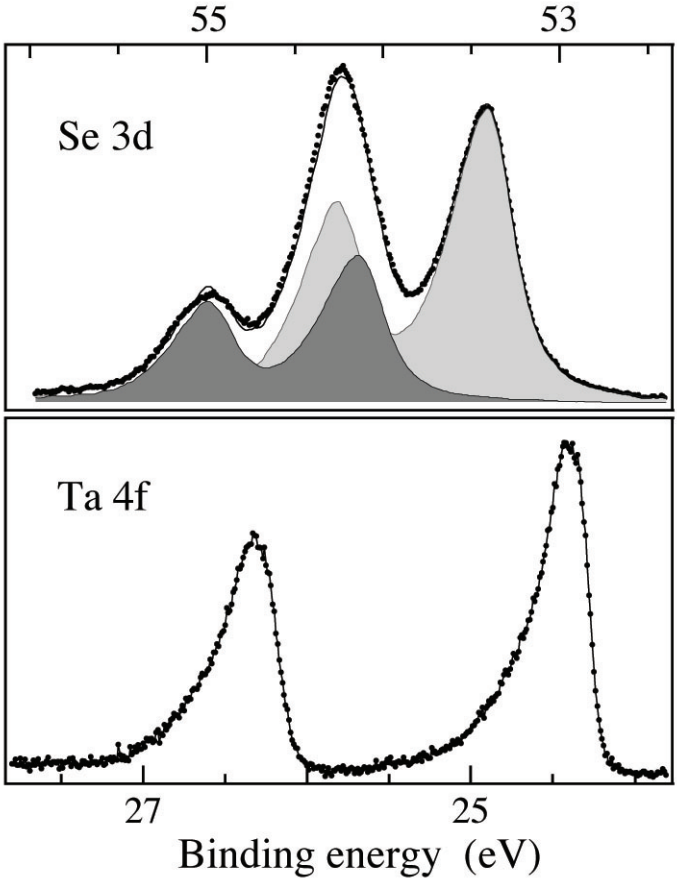

Fig. 4.13: (Above) Se $3d$ core levels (hν = 80 eV) after subtraction of a Shirley background. The complex line shape is reproduced by the sum of two (j = 5/2; 3/2) doublets, with identical line shapes, 2:1 relative intensities, and shifted by 0.73 eV. They correspond to the inequivalent Se sites in the $TaSe_3$ structure. (Below) Ta $4f$ levels showing the typical asymmetric metallic line shape.

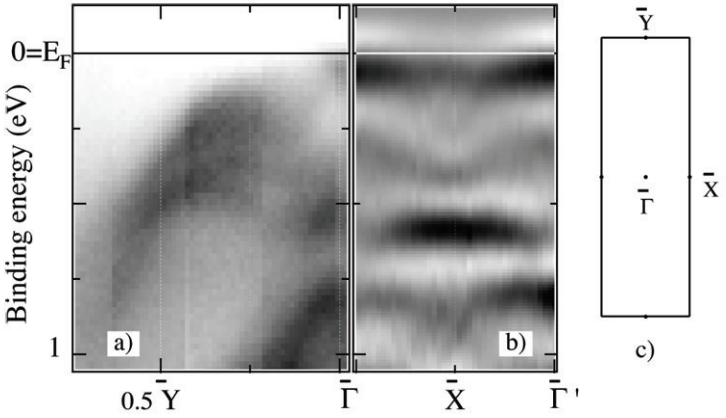

Fig. 4.14: Grey-scale ARPES intensity maps (white is lowest, black is largest intensity) (a) Along the b ($\overline{\Gamma} - \overline{Y}$) chain direction ($h\nu$ = 25 eV; T = 100 K). The main dispersing feature with a maximum at $k \sim 0.3\overline{\Gamma} - \overline{Y}$ is a hybrid Ta 5d - Se 4p band predicted by band structure calculations. Further band features are seen near Γ at $\sim$0.1, 0.5 and 0.8 eV; (b) Along the ($\overline{\Gamma} - \overline{X}$) direction perpendicular to the chains. In order to enhance the weaker band signatures the second derivative of the ARPES signal is shown. (c) Scheme of the surface Brillouin zone.

possibility of inequivalent, albeit not resolved, Ta sites.

4.4.4 The band structure

Fig. 4.14 summarizes the ARPES results for the directions parallel to the chains ($\overline{\Gamma} - \overline{Y}$), and perpendicular, along the ($\overline{\Gamma} - \overline{X}$) direction of the surface Brillouin zone. In the grey-scale images white corresponds to the lowest, and black to the largest ARPES intensity. The prominent maximum at $\sim 0.3\overline{\Gamma} - \overline{Y}$ is due to the overlap of Ta d_{z^2} and Se 4p bands dispersing upwards from their minima at $\overline{\Gamma}$ (at $\sim$0.5 eV) and $\overline{Y}$, respectively [93]. In the calculation [93] the Fermi level cuts this band, yielding a hole pocket. The intensity plot and

a careful analysis of the individual spectra around the maximum at $0.3\overline{\Gamma} - \overline{X}$ (not shown) do not confirm the existence of a hole Fermi surface. We cannot however totally exclude that the band maximum actually crosses E_F elsewhere in the Brillouin zone. A full band mapping, including the direction perpendicular to the layers, would be necessary to clarify this point. Moreover, the possibility that the bands are modified near E_F by an underlying CDW instability must be taken into account (see below). Additional features are visible near $\overline{\Gamma}$ at $\sim$1 eV and close to E_F.

The dispersion along the perpendicular ($\overline{\Gamma} - \overline{X} - \overline{\Gamma}$) direction is small (¡0.15 eV) for all features, providing a microscopic justification for the definition of $TaSe_3$ as a 1D compound. The second derivative of the ARPES intensity map is shown in the figure, in order to enhance the visibility of the weaker features. The experimental band structure – periodicity and intensity – reflects the symmetry of the (a+c) layer, and attests to the good crystalline order of the cleaved surface.

The calculated bands for the 3D structure [93] exhibit a small electron pocket near $\overline{\Gamma}$, where the Fermi level intersects the bottom of a distinct Ta d_{z^2} band. However, the robustness of this prediction is not clear, since the pocket is not present for an isolated (a + c) layer, and it is also affected by dispersion perpendicular to the chains [94]. Careful measurements within a narrow portion of the BZ near Γ (Fig. 4.15), do not show the expected pocket, but rather a fast dispersing band with a maximum at Γ, very close to the Fermi level (E_B = 60meV). The overall shape of the band is well described by a parabola with a maximum slightly above E_F , but the dispersion is suddenly truncated just before the actual crossing, as indicated by the arrow. The striking narrow ($\Delta k \sim 0.1$ Å) flat region is confirmed by the series of spectra (Fig. 4.15(b)) extracted from the central part of the map. A parabolic band with a maximum at Γ is predicted well below (0.35 eV) E_F for an isolated (a+c) layer, but the maximum apparently moves above E_F for a smaller structural unit consisting of two coupled chains. The experimental ARPES result is closer to the latter situation, suggesting that the tight-binding calculation may overestimate in-plane interactions.

The spectra of Fig. 4.16, measured at 20 and 160 K, are repre-

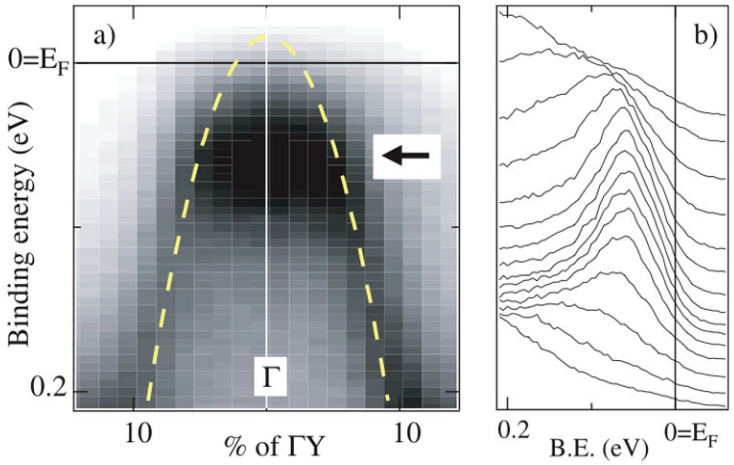

Fig. 4.15: (a) ARPES intensity map showing a close-up of the valence band ($h\nu$ = 25 eV). The band is well described by a parabola (dashed line), except for a at region (arrow) around $\bar{\Gamma}$. (b) ARPES spectra extracted from the center of the map of (a), showing the flat band region.

sentative of the ARPES data for the whole at region around Γ. The 20 K spectrum exhibits both a broad peak at E = 60 meV, and a clear Fermi edge, whose width is determined by the experimental resolution and temperature. It is interesting to notice that at both temperatures the spectral weight at E_F is clearly nonzero. At 160 K the peak position remains constant; the leading edge is broader but, within the experimental accuracy in the Fermi level position, the 160 and 20 K spectra are identical, including the intensity at E_F , if thermal broadening is explicitly taken into account.

4.4.5 Conclusion

Undoubtedly, the unusual flat portion of the band observed just below E_F around Γ (Fig. 4.15), almost certainly plays an important

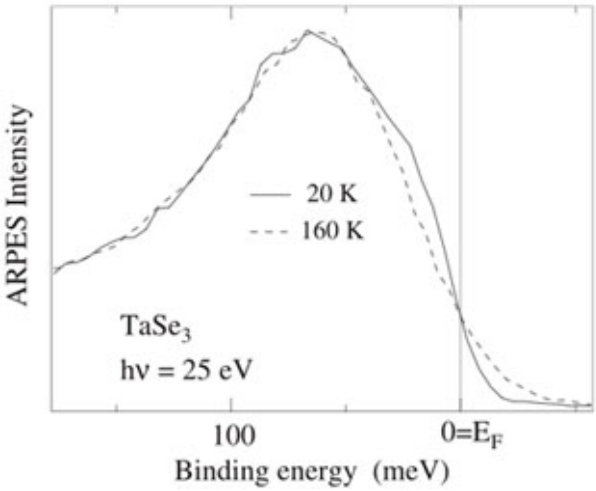

Fig. 4.16: ARPES spectra measured at two temperatures (160 and 20 K) from the flat region at the top of the band of Fig. 4.15. The line shape of the T = 160 K spectrum is compatible with that of the T = 20 K spectrum after thermal broadening.

role in determining the electronic properties of $TaSe_3$. It is therefore important to consider the implications of this observation, even if its origin cannot be conclusively determined from the spectroscopic data.

One of the highly probable scenarios, and in concurrence with band calculation would be a band-structure effect. A shallow electron pocket, not resolved in ARPES due to low momentum resolution induced by the surface "waviness", could be hybridized with the visible occupied band. The band calculations show a mostly unoccupied band that for certain points of the Brillouin zone crosses the E_F. The existing band structure calculations are, however, of limited help, since they do not describe properly the energy position of the parabolic band. At least two unoccupied bands, with Ta d_{z^2} character, disperse upwards from minima at Γ in proximity of E_F, and the energy separation between the top of the hole-like and the

bottom of one of the electron-like bands could be smaller than in the calculation. Hybridization would then yield a delimited region in *k*-space with a high density of states (DOS), favoring the development of a CDW instability, in the spirit of the saddlepoint picture of Ref. [**?**]. The CDW wavevector would span the small flat-band region, so that the corresponding diffraction satellites would be quite close to Bragg peaks, and diffcult to resolve. The resulting gap energy, estimated from the ARPES spectra to be $\sim$0.1 eV, coincides with the peak in the transverse optical conductivity as reported in Ref. [97]. A difficulty with this scenario is the metallic dc resistivity and the finite ARPES intensity at E_F.

Alternatively, we could assume that the ARPES spectra reflect an underlying instability, and interpret the peak energy as the half-width of an associated pseudogap. This would be consistent with the $\sim$0.1 eV energy scale from optics, but also with the metallic character in the fluctuation regime [100, 50]. We would however expect a reduction of the spectral intensity at E_F with decreasing temperature, following the opening of a real gap, which is not experimentally observed. Consistency with the data then requires some other mechanism (e.g., disorder) opposing the development of long-range coherence and hence the opening of a real gap.

4.5 Conclusion

We have studied two transition metal trichalcogenides; $ZrTe_3$and $TaSe_3$. Both show metallic conductivity, although the latter is considered a "bad metal". The electronic properties of these layered compounds are quite intriguing. We find the evidence for the parallel quasi-1D sheets in $ZrTe_3$ that could set the conditions for the charge density wave insulating ground state. However, this modulation is not correlated with the chains and the electronic properties are closer to quasi-2D or even 3D situation. In $TaSe_3$we do not see any instability even though the quasi-one-dimensionality is more pronounced and there are several indications of the underlying instability that fails to condense into a macroscopic state as discusses in Ref. [97].

Spectroscopic features of $ZrTe_3$, even though it is a Peierls conductor, do not show similarities to other Peierls compounds studied previously. This material does not fall far from the light quasiparticle scheme, presumably due to its electronic non-one-dimensionality. The peculiar flat band around the Γ point in $TaSe_3$ (Fig. 4.15, could be explained if we assume that it reflects strongly interacting carriers. In that respect (as discussed in the theoretical chapter of this thesis), electron-phonon coupling could be poorly screened and the excitations we measure are very different from the quasiparticles. In this scenario, flat bands created through hybridization, pin the Fermi level, and this is reflected in the finite intensity at the E_F. The strong peak at 60 meV is then related to the polaronic sideband. If this is indeed the case, the coupling is much weaker than in $K_{0.3}MoO_3$ or $(TaSe_4)_2I$, our reference systems, where almost the whole spectral weight is suppressed.

Chapter 5

One-dimensional instability in $BaVS_3$

$BaVS_3$ has stimulated great interest because of many different properties which show characteristics of both one-dimensionality and non one- dimensionality. In this case, reconciling such properties seems to be a hard challenge. Theory remains highly controversial being unable to explain all experimental evidence available. Exact electronic structure is necessary to provide any headway in the subject and here we present its first experimental determination. The results are submitted for publication: *Mitrovic S, Fazekas P, Søndergaard C. et al*, Experimental electronic structure and metal-insulator transition in $BaVS_3$.

5.1 Introduction

$BaVS_3$ displays a wealth of electron-correlated phenomena. The crystal structure of $BaVS_3$ is strongly one-dimensional, yet the transport is quite isotropic. There exist three different phase transitions none of which is well understood. In particular, the mechanism of a metal-insulator transition at 69 K is still elusive [21].

The main problem in explaining such phenomena was so far the lack of a reliable picture for the electronic structure near the Fermi level. Theoretical calculations [101, 102] were only helpful in part since, as we demonstrate here, they could not predict the correct filling of the corresponding states.

For many years, angle-resolved photoemission has been used to experimentally probe the electronic band structure of different materials. This powerful approach, however, requires high quality single crystals of reasonable size. We were able to grow suitable crystals for $BaVS_3$ to experimentally determine the band structure and therefore to provide a solid background for the understanding of this compound. The most relevant result is the indication that a metal-insulator transition is due to interband nesting.

The interplay between one-dimensional and non-one-dimensional properties finds its correspondence in the character of the electronic states near the Fermi level. The investigation of the electronic structure was thus targeted to the $V^{4+} \rightarrow 3d^1 \rightarrow t_{2g}^1 \rightarrow \{e_g \otimes a_{1g}\}$ occupied orbitals. The wide a_{1g} band would give quasi-one-dimensionality, while the e_g doublet leads to orbital order/fluctuations in a narrow non-one-dimensional band of strongly correlated electrons. The issue is: what is the occupancy of these two types of states? Our results indicate that both types of occupied orbitals are present and should be considered to build a coherent theoretical picture.

The crystal structure can be envisaged as a triangular lattice of chains of face-sharing VS_6 octahedra. Quasi-one-dimensionality is apparent from the fact that V–V distances in the a–b plane are almost 2.4 times as large as in the c-direction of chains [103]. Naively, one would expect good metallic conduction along the chains, and poor conduction in the perpendicular directions. Indeed, this was the prevalent view of the nature of $BaVS_3$ as long as only polycrystalline samples were available [104, 105, 106, 107]. The first resistivity measurements on single crystal samples [108] showed that in a wide range of temperatures, conductivity is essentially isotropic ($\sigma_c/\sigma_a \sim 3$). This required a re-examination of the effective dimensionality of $BaVS_3$, and its relationship to the correlation phenomena displayed by the system.

A salient feature of $BaVS_3$ is the second-order metal–insulator transition (MIT) at T_{MI}=69K, which is manifested also in a strong susceptibility cusp. In most two- or three-dimensional transition metal compounds, the metal–insulator transition is accompanied by a magnetic, or a structural transition. However, $BaVS_3$ is exceptional. The phase on the low-T side of the MIT is non-magnetic, and the structural aspect of the MIT was long overlooked until the recent discovery of tetramerization (doubling of the unit cell in the c-direction) [109, 22].

5.2 Structural and electronic properties

At room temperature, $BaVS_3$ has a chain-like crystal structure formed by face sharing VS_6 octahedra, arranged in a hexagonal structure that would be of the perovskite type if it were not for the elongation of the octahedra in the direction of chains. Separation of the V^{4+} ions within the octahedra of 2.84 Å – interestingly, just about the lattice constant of the metallic vanadium – is much smaller than the interchain distance of 6.72 Å rendering it structurally quasi-one-dimensional[103]. It undergoes three successive phase transitions. Below $T_S \sim 250$ K linear chains gradually distort into zig-zag chains and the crystal symmetry is reduced to the orthorhombic structure. The c cell parameter stays unchanged all the way down to at least 5 K, while a and b change continuously before saturating at 20 K with a noticeable jump, implying a rapid volume change, at around 70 K [110, 111]. This finding inspired some interpretations of volume change as the order parameter.

Resistivity reaches a minimum at 130 K, and then then starts to slightly rise as it approaches the T_{MI} (see Fig. 5.2). A sharp increase in the resistivity marks the metal-insulator transition at $T_{MI} = 69$ K (e.g. see Ref. [107, 108]) and a transition marking the onset of the antiferromagnetic long-range order occurs at $T_\chi \sim 30$ K.

The ground state of $BaVS_3$ is, however, quite controversial: conflicting claims have been put forward based on the results of microscopic probes such as NMR/NQR [112], muon-spin relaxation

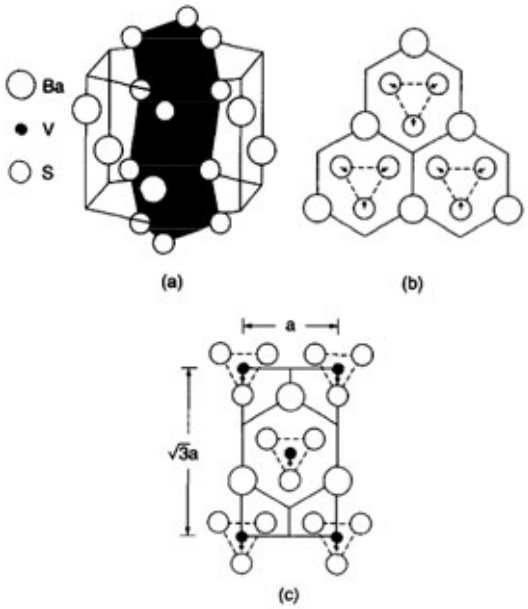

Fig. 5.1: Crystal structure from Ref. [101] (a) Primitive unit cell for hexagonal $BaVS_3$ illustrating the linear c-axis chains that are formed via face-sharing VS_6 octahedra with Ba spacers; (b) an "idealized" (0001) plane showing S displacements when $x < x_{ideal}$; (c) basal-plane projection of the orthorhombic O($\sqrt{3} \times 1$) phase, including the central-plane V displacements that produce zigzag chains.

(μSR) [113] and inelastic neutron scattering (INS) [114]. While the NMR/NQR experiments suggested a non-magnetic ground state, the same authors (Nakamura and co-workers) found static magnetic fields by μSR and INS implying an antiferromagnetic ordering at 30 K.

The electronic band calculations in the vicinity of the chemical potential show bands originating from the V^{4+} ($3d^1$) and S ($3p$) levels [102]. In the presence of the octahedral potential, V^{4+} ($3d^1$) level is split into the e_g doublet and the $e(t_{2g})$ triplet. The elongation

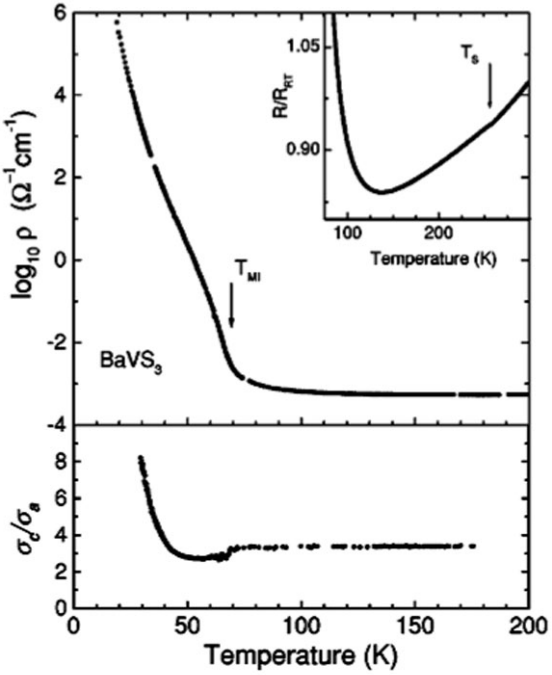

Fig. 5.2: Temperature dependence of the resistivity $\rho_c(T)$, and the conduction anisotropy σ_c/σ_a in $BaVS_3$, with arrows indicating T_S, T_{MI} and $T\chi$. Figure taken from Ref. [108]

of the octahedra along the chain axis direction induces a splitting of the triplet into the e_g doublet and a a_{1g} singlet. The latter is a consequence of the large overlap of the along-chain axis orbitals, thus one-dimensional in character and of a large bandwidth. The e_g doublet loses degeneracy upon the hexagonal to orthorhombic symmetry reduction. These are narrow Mott-localized bands. All three bands are found to cross the Fermi level. The a_{1g} band is predicted to almost reach the end of the Brillouin zone with the Fermi level crossing at $k_F = 0.47c^*$.

The question of band occupancy is crucial to give the correct

description of the insulating state. If only the a_{1g} band counts, the insulating phases of $BaVS_3$ must be describable in terms of atomic displacements and spins. If only e_g states are occupied, spin and orbital ordering must be considered on an equal footing (a preliminary discussion of this scenario was given in [108]). If both a_{1g} and e_g electrons are present, complicated scenarios can arise.

Choosing the orthorhombic c-axis as the z axis, the a_{1g} orbital has z^2 character, with strong overlap in the c-direction. The a_{1g} band is wide and almost one-dimensional. If only the a_{1g} band were filled, $BaVS_3$ could be an ordinary semiconductor or a weakly correlated metal, without the possibility of localized moment formation. This is obviously not the case. There must be also e_g electrons. In fact, all band structure calculations [101, 102] agree that the Fermi level is lying in the region of the crossing of a_{1g}-like and e_g-like bands. However, the status of these predictions is somewhat uncertain because neither of the calculations yields the possibility of a non-magnetic insulating state. It is important to have experimental results about the filling of the e_g and a_{1g} bands, and the nature of the electronic structure in the intermediate ($T_\chi < T < T_{\mathrm{MI}}$) insulating phase.

5.3 Experimental

We have performed ARPES on fairly large ($\approx 0.25 \times 0.25 \times 3$ mm^3) single crystals of $BaVS_3$ grown by the slow cooling technique in melted Tellurium [115]. The quality of the crystals was controlled by resistivity measurements under ambient and higher pressure [108]. The data were collected at the PGM beamline of the Synchrotron Radiation Center (SRC), Stoughton (WI), USA, and with a Scienta-2002 analyzer. The spectra presented were measured with a total energy and momentum resolution of ΔE = 15 meV and Δk = 0.04 Å^{-1}. Clean surfaces were exposed in UHV conditions of the analyzer chamber being in the 10^{-11} mbar range. The temperature of the sample could be controlled in the range from 5 K to 150 K.

Due to the pronounced one-dimensional structure, samples were rather fractured than cleaved. With no existing preferred plane of

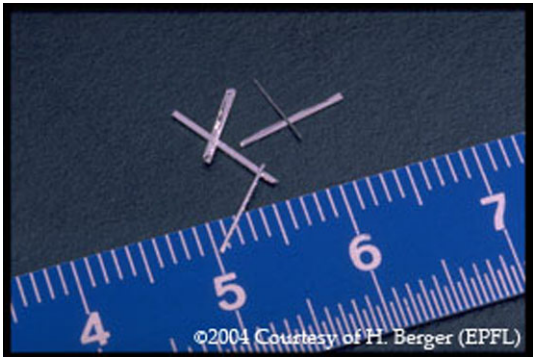

Fig. 5.3: Photograph of $BaVS_3$ single crystals. The crystals are black with a metallic shine. Unlike other crystals studied in this thesis that appear as platelets, $BaVS_3$ reflects its one-dimensional crystal structure in the appearance. Upon cleaving it can be seen that the crystal consists of tiny fibers held together, very similar to $(TaSe_4)_2I$.

cleavage, the always stepped surface in the direction perpendicular to structural chains, makes momenta of electrons poorly defined, and the observed essential flatness of the bands in this direction cannot be taken as an ARPES proof of their one-dimensionality. The measurements in the parallel-to-chain direction, however, were successfully reproduced with each attempt. Possible spectral shifts from charging due to broken chains and poor conductivity were not observed as we checked by changing the intensity of light. However, charging starts to develop below 30 K and the spectra below this temperature are not reported here.

5.4 Experimental electronic structure

Figure 5.4 shows the ARPES intensity map taken in the Γ–Z direction parallel to the chains. For best resolution, measurements were taken at T = 40K, and with a photon energy of 50eV, where we found all features close to the Fermi level E_F distinctly resolved. A correspond-

ing part of the *ab initio* calculation for the orthorhombic phase by Mattheiss [101] is displayed next to the map. The measured intensity maps are essentially unchanged from 40K to 150K, except for the temperature broadening of the features and the shift of the leading edge close to the Fermi level as discussed later.

The theoretical ***k***-space periodicity in the extended zone scheme is well reproduced in Fig. 5.4, indicating that the measured surface gives a good probe for the bulk states. We read off the period $2z$ where $z = \overline{\Gamma Z} \approx \pi/c_0 = 0.56\text{Å}^{-1}$, $c_0 = 5.61$Å being the c-axis lattice constant for the two-atomic unit cell. Given the momentum resolution of our measurement, this is compatible with the value obtained from structure determination.

We find that both the positions and the widths of the bands at energies above 1eV - originating from the S($3p$) orbitals - are in agreement with the calculations [101].

Details of the electronic states just below the E_F are shown in the $-d^2I/dE^2$ intensity map of Figure 5.5(c). The second derivative clearly reveals two bands: a dispersive band with approx. 1eV bandwidth, which we identify as a one-dimensional a_{1g} band; and a rather non-dispersive band located at $\sim$0.4eV, which we associate with e_g states. Selected raw measured energy distribution curves (EDCs) presented in the Figure 2(d) also demonstrate both features. Clearly, the transport should be influenced by both bands. This should account for the observed low anisotropy. Indeed, the estimate obtained from the ratio of the averaged Fermi velocities $\langle v_\parallel^2 \rangle / \langle v_\perp^2 \rangle \propto \sigma_c/\sigma_a \sim 3.8$ by Mattheiss [101], closely agrees with the experimental result [108]. In addition, our data show that the a_{1g} band is hybridized with one of the sulphur π bands, which should play a role in reducing the macroscopic manifestation of the quasi-1D crystal structure. The flat e_g bands give a high density of states at the Fermi level E_F.

We cannot see the higher-lying folded-back part of the a_{1g} band but its overall width must approach the theoretical value $W(a_{1g}) \sim$ 2eV. On the other hand, we estimate $W(e_g) < 0.4$eV. We conclude that the intriguing behavior of $BaVS_3$ results from the fact that two kinds of d-states: strongly correlated narrow-band e_g-states, and weakly correlated wide-band a_{1g}-states, coexist at the Fermi level. We

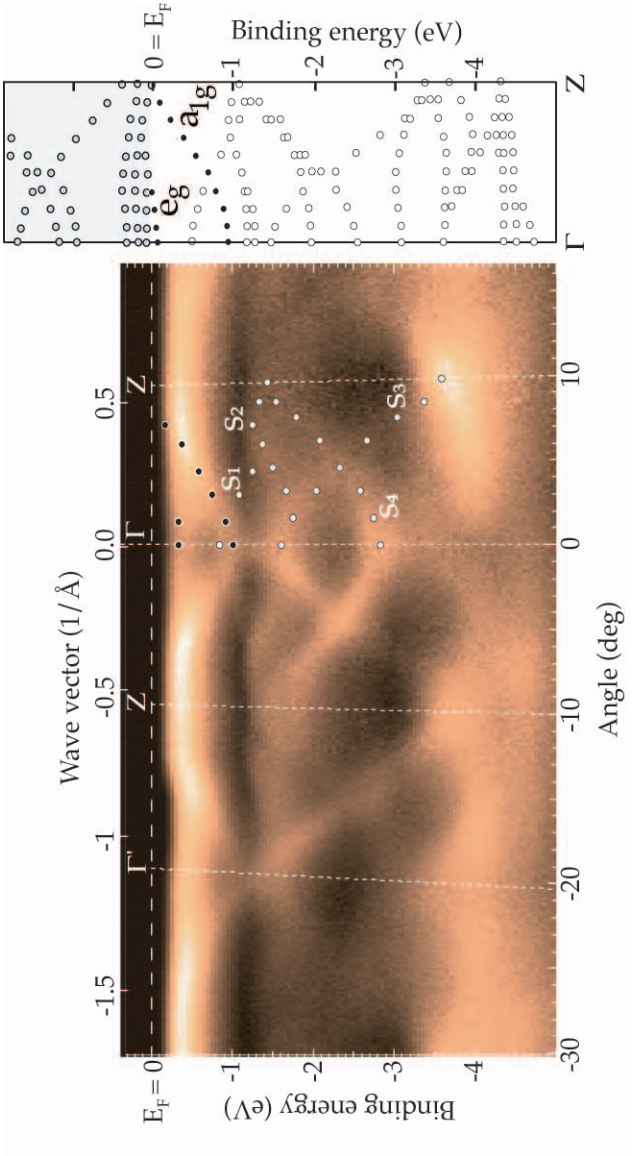

Fig. 5.4: (Left) ARPES intensity map taken in the direction parallel to structural chains and at 40 K. Brighter color signifies higher intensity. Bands arising from the V (3*d*) level are followed with black circles, and the S (3*p*) bands with the white ones. The zone boundaries were plotted from the calculated value. (Right) Corresponding band calculation adapted from Ref. [101]

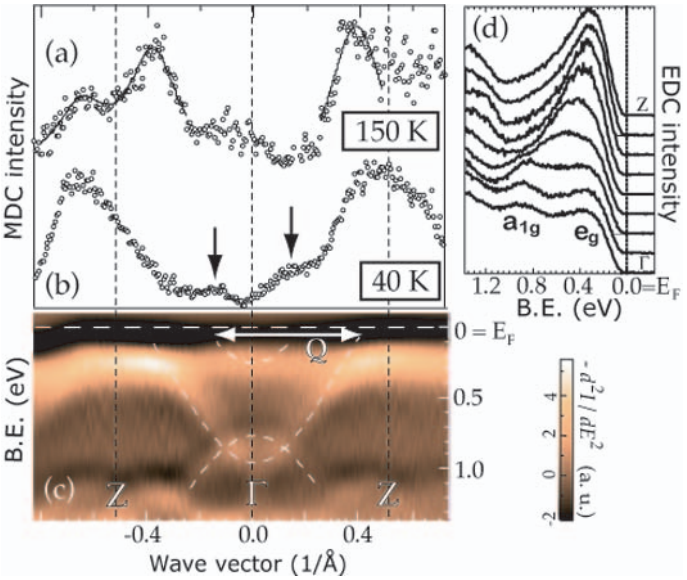

Fig. 5.5: (a) An MDC of 50meV wide integrated region just below the Fermi energy ($E_B^* = 50$meV) from an ARPES map at 150K. The fit is a double Lorentzian. (b) The equivalent MDC plot ($E_B = E_B^* - 80$meV) from a map at 40K. The arrows indicate the positions of k_{F_2}. (c)$-d^2I/dE^2$ plot of the ARPES map at 40K. The dashed lines serve as guides to the eye. (d) Selected raw EDC's in equidistant steps from Γ to Z point.

ascribe the Curie-like susceptibility, and the bad metallic character of the $T > T_{\mathrm{MI}}$ phase, to e_g electrons, and to e_g–a_{1g} scattering. As to the symmetry breaking aspect of the MIT, the orbital degrees of freedom of the e_g electrons are expected to give an electronic order parameter complementary to the structurally defined tetramerization amplitude. Spin–orbital models have the capacity to describe the development of a spin gap, which is known to accompany the MIT of $BaVS_3$ [116].

A previous photoemission study reported the results of angle-integrated measurements on polycrystalline samples [117]. Our angle-resolved results on good single crystals confirm the previous findings about the lack of a Fermi edge in a temperature range above T_{MI}. In our ARPES maps, peaks of all bands fail to cross the Fermi level even in the metallic state. This was previously attributed to Luttinger-liquid behavior. However, the electronic properties of $BaVS_3$ are too far from being quasi-1D to permit such an interpretation. On the other hand, we note that such spectroscopic features are not unusual in correlated electron systems. Spectral weight, which is the only observable of an ARPES experiment, is often renormalized by strong interactions which can shift the spectral weight to higher binding energy masking the real quasiparticle peak. Fermi level crossing is often still observable with careful analysis. For that purpose we took a momentum distribution curve (MDC) from an ARPES map taken at 150K with a 50meV wide window of integration around the Fermi level. The obtained MDC shown in Figure 2(a) reveals peaks marking the crossings of the a_{1g} band within the first and the second Brillouin zone. The crossing determined from Lorentzian peak fits, takes place at the wave vector $k_{F_1} = (0.40 \pm 0.05)\ \text{Å}^{-1}$. The symmetry of the crossings from both sides of the BZ positions the Z point at $\mathrm{Z} = (0.56 \pm 0.05)\ \text{Å}^{-1}$, in agreement with the theoretical value.

The e_g-band is not so well resolved. However, the increase in intensity not far from the Γ point in Figure 2(a) indicates the possibility of a Fermi level crossing, creating a shallow electron pocket. If we look at the equivalent MDC in the low temperature map (Figure 2(b)) that accounts for the spectral changes due to the gap opening, the

electron pocket shape of the band is clearer. The band should cross E_F at $k_{F_2} = (0.15 \pm 0.05)$ Å^{-1}. The electron pocket shape is in agreement with the theoretical predictions.

The apparent bending of the e_g band towards the a_{1g} band is a consequence of the resolution and back-folding of *shadow* bands – the signature of lattice distortions [17]. Equally, the a_{1g} band folds into shadow bands, which is the reason behind the high intensity around the Z point since the signals from both sides of the Brillouin zone boundary overlap.

5.5 One-dimensional instability

Strong one-dimensional structural fluctuations are observed in a wide temperature range above the MIT in diffraction experiments [22]. Such observations are common in quasi-1D charge density wave (CDW)-bearing systems. However, $BaVS_3$ is not thought to have a CDW. Nevertheless, as in CDW systems, the 1D fluctuations ought to have a relation to $\boldsymbol{k}$-space features. We examined our experimentally determined band structure to check if we can identify a Fermi surface instability which can introduce a gap into the wide a_{1g} band.

We find that the a_{1g} band alone cannot satisfy the nesting condition, thus we exclude intra-band nesting. We can also exclude a $4k_F$ instability, or the possibility of the e_g band supporting nesting in itself. On the other hand, our results are consistent with an instability involving both bands, since our data are in agreement with a condition $k_{F_1} + k_{F_2} = 0.5c^* = Q_{\mathrm{CDW}}$. The mechanism of interband nesting leading to a CDW insulating state is known in low-dimensional systems such as quasi-1D organic conductors and $K_{0.3}MoO_3$ blue bronze. However, the nature of the $T_\chi < T < T_{\mathrm{MI}}$ phase of $BaVS_3$ is not yet clear, and the precise mechanism of the instability involving both kinds of bands remains to be identified.

We have monitored the spectral changes with temperature through the metal–insulator transition. The position of the peak in the EDCs of our intensity maps (Fig. 5.6) stays at the same position but the leading edge moves to higher binding energies. If we plot the po-

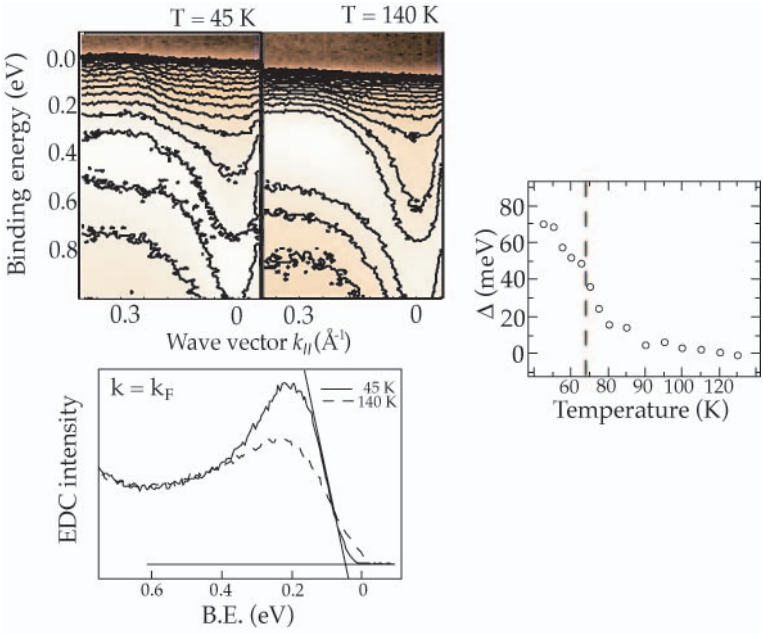

Fig. 5.6: (Up Left) Intensity maps at 45 and 140 K with contour plots of same intensity regions. Notice the shift of the contour line at the Fermi level. (Down Left) EDC's taken at 140 and 45K at the E_F crossing of the a_{1g} band. The method of leading edge position extraction is shown on the low-temperature EDC and (Right) is its dependence on the temperature. The dashed line in (right) marks the MIT temperature.

sition of the leading edge versus temperature, we see a monotonic shift of the leading edge - that most probably started above 150K - and a noticeable non-linear increase in the shift below 90K. This is consistent with the results of Ref. [117] and indicative of the opening of a charge gap. We do not see a clear transition associated with the $T_{MI} = 69K$. This is not unusual, particularly when pre-transitional fluctuations are present. The gap as seen in photoemission spectra develops in the same range of temperature where resistivity [108, 118] and thermopower [119] measurements identify a "precursor" to the insulating phase, and where X-Ray diffraction detects large 1D fluctuations [22]. The saturation of the leading edge shift indicates a charge gap of $\Delta_{ch} = 60 - 70meV$. This is in good agreement with the value obtained from transport measurements in the temperature range where the Arrhenius law applies [107, 117, 108].

In transport, it is difficult to identify the charge gap from Arrhenius plots since the measured resistivity depends on sample purity, but it is agreed that it lies in the range $2\Delta_{ch} = 50 - 100$ meV [107, 117, 108].

We point it out that the gap opening can be seen for any choice of k vector (see up left of Fig.-5.6), as should be expected if the complete Fermi surface participates and if we take into account that the closeness of the bands and surface-defined momentum resolution smear out signals from both bands across the Brillouin zone.

The broad, pseudogapped spectral features are incompatible with a standard quasiparticle picture. Recently, it was argued that in Peierls systems they are a signature of polaronic carriers (for details see Chapter 2.4.1). The strong case for this scenario was found in the studies on $K_{0.3}MoO_3$ blue bronze [17]. Analogous considerations may hold for $BaVS_3$, where the MIT has certain aspects of a spin-Peierls transition, and the coupling of the e_g electrons to the local Jahn–Teller modes is important. Interpretation of spectra in terms of Luttinger liquid or signal overlap from multiple bands is unlikely, since similar consideration for blue bronze were eliminated through studies on the related insulating, "one-band" system $K_{0.33}MoO_3$ (red bronze) [24].

5.6 Conclusion

To conclude, we derived the structure of the bands close to the Fermi level from ARPES measurements in a wide range of temperatures on both sides of the metal–insulator transition at $T_{\mathrm{MI}} = 69\mathrm{K}$. We found that the physics of $BaVS_3$ is governed by the coexistence of weakly correlated wide-band a_{1g} electrons and strongly correlated narrow-band e_g electrons near the Fermi level. Our results are consistent with the a_{1g}–e_g interband nesting condition and we propose it as a plausible mechanism for the metal–insulator transition.

Chapter 6

Conclusions and outlook

Real materials with quasi-1D structure are a prominent class of solids and perfect candidates for non-Fermi liquid behavior. They provide us with the opportunity to take a closer look at many of the theoretically predicted exotic states related to low-dimensionality and electron correlations. These properties offer a range of potential applications such as in the high-temperature superconductors and for the switching devices that utilize the abrupt change in electronic and magnetic properties. Furthermore, a very active field of nanotechnology also depends on the understanding of correlated electrons.

This thesis presented ARPES studies on several inorganic materials with a quasi-1D crystal structure. The selected materials are for the first time studied by ARPES, mainly due to the successful efforts in our Institute to produce high quality crystals of a suitable size for photoemission experiments. The goal of this work was to (i) experimentally determine the electronic structure of these materials and compare it to the available first-principles calculations and (ii) to investigate non-Fermi liquid aspects, precisely the non-Fermi liquid spectral lineshapes.

Red bronze $K_{0.33}MoO_3$ is an insulating compound with a very simple band structure where the material properties are determined by one band that is dispersive only in one direction along the struc-

tural chains. We have found that defects play an important role for the physics of this material, which is not an intrinsic semiconductor, but contains intragap states that pin the Fermi level. The spectral lineshapes bear remarkable resemblance to the ones found in the related blue bronze $K_{0.3}MoO_3$.

We have found that the topology of the Fermi surface (FS) plays an important role on the electronic properties in transition metal trichalcogenides. We have determined the electronic structure and the details of the FS in $ZrTe_3$ and $TaSe_3$. $ZrTe_3$ shows 1D sheets in the FS that provide the conditions for the Peierls instability, which is indeed realized but uncorrelated with the 1D chains. $TaSe_3$, on the other hand shows no instabilities due to unavailability of favorable conditions in the FS topology.

$BaVS_3$ is a complex system that displays many features of strong one-dimensionality at the same time as electron localization. Of special interest is the metal-insulator transition at 69 K with a puzzling origin. Our study determines the electronic structure that can provide a solid framework for reconciliation of many conflicting experimental results. We have experimentally determined the controversial orbital population. The electronic properties are a consequence of the interplay between a 1D band from d_{z^2} orbitals along the chain, and a narrow Mott-localized band from the $e(t_{2g})$ states. Furthermore, we propose a scenario of interband nesting for the metal-insulator transition, in support of observed one-dimensional fluctuations and superlattice formation.

Non-Fermi liquid lineshapes in low-dimensional materials have several possible origins. The chosen systems fall into the same class of materials that go through the charge density wave (CDW) transition or are closely related to such materials. The extrinsic effects [120] that are linked to poorly conducting solids and broken chains in 1D systems are systematically ruled out in our case. Also, the fluctuation effects that accompany the Peierls transition and induce a pseudogapped state [18] do not account for the observed effects as discussed in the theoretical chapter of this thesis. The non-Fermi liquid lineshapes are thus linked to the predictions of a Luttinger liquid (LL), the CDW, the electron correlations and interactions, or

their combination. In Peierls conductors it has been suggested recently that the non-Fermi liquid lineshape is a consequence of the electron-phonon interaction (the so-called polaronic lineshape). The motivation for the work comes from the recent studies on two such compounds – $K_{0.3}MoO_3$ [17] and $(TaSe_4)_2I$ [16]. These compounds undergo a CDW transition due to their nested open Fermi surfaces, i.e. as a consequence of quasi-1D character. However, they do not display any signs of a Luttinger liquid, the prevailing theory for 1D metals. The two studies suggest that the realizations of a Luttinger liquid (LL) may not be seen in this class of compounds as a result of a strong electron–phonon coupling. It should be noted, however, that LL lineshape is not entirely incompatible with the experiment [11], but we would have to suppose a large anomalous dimension $\alpha \sim 1$, suggesting strong, long-range interactions.

Theoretically, we do not expect realizations of a LL in a gapped or pseudogapped state. In that respect, the Mo red bronze surely cannot fit into the LL framework. The striking correspondence with the lineshape in blue bronze eliminates LL as a mechanism behind the peculiar features. Also, particular simplicity of a single band in red bronze suggests that the lineshape of the blue bronze is not a band effect due to two close bands near the Fermi level. On the other hand, the common parameter – the lattice that is almost identical in two materials – reinforces the electron-phonon interaction induced renormalization as a reason behind the characteristic broad EDC lineshapes. Indeed, only by applying the predictions of the polaronic scenario we were able to extract the gap size that is consistent with transport measurements.

We find the spectral characteristics of the polaronic lineshape in $BaVS_3$ as well. Despite the macroscopic localized electronic appearance, the underlying 1D electronic nature is reflected in 1D fluctuations and in the possible realization of the CDW state. Further investigation is necessary to link the lineshape to the electron–phonon coupling.

More extensive experiments and studies on these and related materials are needed to separate, or create a conjunction of the effects of electronic one-dimensionality and realizations of a LL with the

electronic correlations and instabilities to find the nature of the non-Fermi liquid lineshapes in ARPES. Our results show that even though these lineshapes do not demonstrate the singular behaviors expected for 1D systems, due to electron-phonon interaction or some other mechanism, their realization is strongly dependent on the actual 1D electronic character.

References

[1] L. D. Landau. *Sov Phys Jetp-Ussr*, 3(6):920–925, 1957.

[2] F. D. M. Haldane. *J Phys C Solid State*, 14(19):2585–2609, 1981.

[3] Stefan Hufner. *Photoelectron spectroscopy : principles and applications*. Springer series in solid-state sciences. Springer-Verlag, Berlin ; New York, 2003. Stefan Hfner. ill. ; 24 cm.

[4] G. Gruner. *Density Waves in Solids*. Addison-Wesley, Reading, MA, 1994.

[5] N. F. Mott. *Metal-Insulator Transitions*. Taylor and Francis, London/Philadelphia, 1990.

[6] G. A. Sawatzky. *Nature*, 342(6249):480–481, 1989.

[7] J. Voit. *J. Phys.-Condes. Matter*, 5(44):8305–8336, 1993.

[8] J. Voit. *Rep. Prog. Phys.*, 58(9):977–1116, 1995.

[9] R. E. Peierls, A. Salam, P. T. Matthews, and G. Feldman. *Rep. Prog. Phys.*, 18:423–477, 1955.

[10] M. Grioni, H. Berger, M. Garnier, F. Bommeli, L. Degiorgi, and C. Schlenker. *Phys. Scr.*, T66:172–176, 1996.

[11] G. H. Gweon, J. D. Denlinger, J. W. Allen, R. Claessen, C. G. Olson, H. Hochst, J. Marcus, C. Schlenker, and L. F. Schneemeyer. *J. Electron Spectrosc. Relat. Phenom.*, 117:481–502, 2001.

[12] M. Grioni and J. Voit. *Electron Spectroscopies Applied to Low-Dimensional Structures*, volume 24 of *Physics and Chemistry of Materials with Low-Dimensional Structures*. Kluwer Academic Publishers, 2000.

[13] P. Segovia, D. Purdie, M. Hengsberger, and Y. Baer. *Nature*, 402(6761):504–507, 1999.

[14] F. J. Himpsel, K. N. Altmann, J. N. Crain, A. Kirakosian, J. L. Lin, and A. Liebsch. *J. Electron Spectrosc. Relat. Phenom.*, 126(1-3):89–99, 2002.

[15] B. Dardel, D. Malterre, M. Grioni, P. Weibel, Y. Baer, C. Schlenker, and Y. Petroff. *Europhys. Lett.*, 19(6):525–530, 1992.

[16] L. Perfetti, H. Berger, A. Reginelli, L. Degiorgi, H. Hochst, J. Voit, G. Margaritondo, and M. Grioni. *Phys. Rev. Lett.*, 8721(21):art. no.–216404, 2001.

[17] L. Perfetti, S. Mitrovic, G. Margaritondo, M. Grioni, L. Forro, L. Degiorgi, and H. Hochst. *Phys. Rev. B*, 66(7):art. no.–075107, 2002.

[18] P. A. Lee, T. M. Rice, and P. W. Anderson. *Phys. Rev. Lett.*, 31(7):462–465, 1973.

[19] C. Schlenker. *Low-dimensional Electronic Properties of Molybdenum Bronzes and Oxides*, volume II. Kluwer Academic Publishers, 1989.

[20] M. H. Whangbo, E. Canadell, P. Foury, and J. P. Pouget. *Science*, 252(5002):96–98, 1991.

[21] M. H. Whangbo, H. J. Koo, D. Dai, and A. Villesuzanne. *J Solid State Chem*, 175(2):384–388, 2003.

[22] S. Fagot, P. Foury-Leylekian, S. Ravy, J. P. Pouget, and H. Berger. *Phys. Rev. Lett.*, 90(19):–, 2003.

[23] W. Schattke and M.A Van Hiove. *Solid-State Photoemission and Related Methods Theory and experiment*. Wiley-VCH, 2003.

[24] S. Mitrovic, L. Perfetti, C. Sondergaard, G. Margaritondo, M. Grioni, N. Barisic, L. Forro, and L. Degiorgi. *Phys. Rev. B*, 69(3):art. no.–035102, 2004.

[25] L. D. Landau and I. M. Khalatnikov. *Sov Phys Jetp-Ussr*, 2(1):69–72, 1956.

[26] A. J. Schofield. *Contemp Phys*, 40(2):95–115, 1999.

[27] R. Claessen, R. O. Anderson, G. H. Gweon, J. W. Allen, W. P. Ellis, C. Janowitz, C. G. Olson, Z. X. Shen, V. Eyert, M. Skibowski, K. Friemelt, E. Bucher, and S. Hufner. *Phys. Rev. B*, 54(4):2453–2465, 1996.

[28] S. Tomonaga. *Prog Theor Phys*, 5(4):544–569, 1950.

[29] J. M. Luttinger. *J Math Phys*, 4(9):1154, 1963.

[30] P. Y. Ledaeron and S. Aubry. *J Phys C Solid State*, 16(24):4827–4838, 1983.

[31] A. Luther and V. J. Emery. *Phys. Rev. Lett.*, 33(10):589–592, 1974.

[32] V. Vescoli, L. Degiorgi, W. Henderson, C. Gruner, K. P. Starkey, and L. K. Montgomery. *Science*, 281(5380):1181–1184, 1998.

[33] C. Kim, A. Y. Matsuura, Z. X. Shen, N. Motoyama, H. Eisaki, S. Uchida, T. Tohyama, and S. Maekawa. *Phys. Rev. Lett.*, 77(19):4054–4057, 1996.

[34] J. D. Denlinger, G. H. Gweon, J. W. Allen, C. G. Olson, J. Marcus, C. Schlenker, and L. S. Hsu. *Phys. Rev. Lett.*, 82(12):2540–2543, 1999.

[35] R. Claessen, M. Sing, U. Schwingenschlogl, P. Blaha, M. Dressel, and C. S. Jacobsen. *Phys. Rev. Lett.*, 88(9):art. no.–096402, 2002.

[36] L. Bartosch and P. Kopietz. *Phys. Rev. B*, 62(24):R16223–R16226, 2000.

[37] H. Monien. *Phys. Rev. Lett.*, 8712(12):art. no.–126402, 2001.

[38] D. C. Johnston. *Phys. Rev. Lett.*, 52(23):2049–2052, 1984.

[39] A. Schwartz, M. Dressel, B. Alavi, A. Blank, S. Dubois, G. Gruner, B. P. Gorshunov, A. A. Volkov, G. V. Kozlov, S. Thieme, L. Degiorgi, and F. Levy. *Phys. Rev. B*, 52(8):5643–5652, 1995.

[40] J. Voit, L. Perfetti, F. Zwick, H. Berger, G. Margaritondo, G. Gruner, H. Hochst, and M. Grioni. *Science*, 290(5491):501–503, 2000.

[41] J. Schafer, E. Rotenberg, S. D. Kevan, P. Blaha, R. Claessen, and R. E. Thorne. *Phys. Rev. Lett.*, 8719(19):art. no.–196403, 2001.

[42] M. H. Whangbo and L. F. Schneemeyer. *Inorg. Chem.*, 25(14):2424–2429, 1986.

[43] J. P. Pouget, S. Girault, A. H. Moudden, B. Hennion, C. Escribefilippini, and M. Sato. *Phys. Scr.*, T25:58–62, 1989.

[44] J. L. Mozos, P. Ordejon, and E. Canadell. *Phys. Rev. B*, 65(23):art. no.–233105, 2002.

[45] J. Dumas and C. Schlenker. *Int. J. Mod. Phys. B*, 7(23-24):4045–4108, 1993.

[46] G. H. Gweon, J. W. Allen, R. Claessen, J. A. Clack, D. M. Poirier, P. J. Benning, C. G. Olson, W. P. Ellis, Y. X. Zhang, L. F. Schneemeyer, J. Marcus, and C. Schlenker. *J. Phys.-Condes. Matter*, 8(48):9923–9938, 1996.

[47] A. V. Fedorov, S. A. Brazovskii, V. N. Muthukumar, P. D. Johnson, J. Xue, L. C. Duda, K. E. Smith, W. H. McCarroll, M. Greenblatt, and S. L. Hulbert. *J. Phys.-Condes. Matter*, 12(9):L191–L198, 2000.

[48] E. Canadell and M. H. Whangbo. *Chem. Rev.*, 91(5):965–1034, 1991.

[49] C. Noguera. *J Phys C Solid State*, 18(8):1647–1664, 1985.

[50] N. Shannon and R. Joynt. *J. Phys.-Condes. Matter*, 8(49):10493–10509, 1996.

[51] L. Degiorgi, Stthieme, B. Alavi, G. Gruner, R. H. McKenzie, K. Kim, and F. Levy. *Phys. Rev. B*, 52(8):5603–5610, 1995.

[52] L. Perfetti, C. Rojas, A. Reginelli, L. Gavioli, H. Berger, G. Margaritondo, M. Grioni, R. Gaal, L. Forro, and F. R. Albenque. *Phys. Rev. B*, 6411(11):art. no.–115102, 2001.

[53] P. Kopietz, V. Meden, and K. Schonhammer. *Phys. Rev. Lett.*, 74(15):2997–3000, 1995.

[54] F. Zwick, H. Berger, I. Vobornik, G. Margaritondo, L. Forro, C. Beeli, M. Onellion, G. Panaccione, A. Taleb-Ibrahimi, and M. Grioni. *Phys. Rev. Lett.*, 81(5):1058–1061, 1998.

[55] F. Zwick, D. Jerome, G. Margaritondo, M. Onellion, J. Voit, and M. Grioni. *Phys. Rev. Lett.*, 81(14):2974–2977, 1998.

[56] J. M. Robin. *Phys. Rev. B*, 56(21):13634–13637, 1997.

[57] A. S. Mishchenko, N. V. Prokof'ev, A. Sakamoto, and B. V. Svistunov. *Phys. Rev. B*, 62(10):6317–6336, 2000.

[58] H. Requardt, R. Currat, P. Monceau, J. E. Lorenzo, A. J. Dianoux, J. C. Lasjaunias, and J. Marcus. *J. Phys.-Condes. Matter*, 9(41):8639–8655, 1997.

[59] F. Wooten. *Optical Properties of Solids*. Academic Press, New York, 1972.

[60] D. S. Dessau, T. Saitoh, C. H. Park, Z. X. Shen, P. Villella, N. Hamada, Y. Moritomo, and Y. Tokura. *Phys. Rev. Lett.*, 81(1):192–195, 1998.

[61] J. Demsar, K. Biljakovic, and D. Mihailovic. *Phys. Rev. Lett.*, 83(4):800–803, 1999.

[62] G. H. Gweon, J. W. Allen, J. A. Clack, Y. X. Zhang, D. M. Poirier, P. J. Benning, C. G. Olson, J. Marcus, and C. Schlenker. *Phys. Rev. B*, 55(20):13353–13356, 1997.

[63] K. Breuer, C. Stagerescu, K. E. Smith, M. Greenblatt, and K. Ramanujachary. *Phys. Rev. Lett.*, 76(17):3172–3175, 1996.

[64] J. J. Paggel, T. Miller, and T. C. Chiang. *Science*, 283(5408):1709–1711, 1999.

[65] T. Valla, A. V. Fedorov, P. D. Johnson, and S. L. Hulbert. *Phys. Rev. Lett.*, 83(10):2085–2088, 1999.

[66] V. Vescoli, F. Zwick, J. Voit, H. Berger, M. Zacchigna, L. Degiorgi, M. Grioni, and G. Gruner. *Phys. Rev. Lett.*, 84(6):1272–1275, 2000.

[67] M. H. Whangbo, M. Evain, E. Canadell, and M. Ganne. *Inorg. Chem.*, 28(2):267–271, 1989.

[68] B. Zawilski, J. Richard, and J. Marcus. *Solid State Commun.*, 109(1):41–44, 1999.

[69] B. Zawilski, T. Klein, and J. Marcus. *Solid State Commun.*, 124(1-2):39–44, 2002.

[70] G. Travaglini and P. Wachter. *Solid State Commun.*, 47(4):217–221, 1983.

[71] R. Xiong, J. Shi, Q. M. Xiao, W. F. Tang, H. L. Liu, and D. C. Tian. *J. Mater. Sci.*, 36(22):5511–5514, 2001.

[72] G. H. Bouchard, Perlstei.J, and M. J. Sienko. *Inorg. Chem.*, 6(9):1682, 1967.

[73] A. Wold, W. Kunnmann, A. Ferretti, and R. J. Arnott. *Inorg. Chem.*, 3(4):545, 1964.

[74] G. Travaglini, P. Wachter, J. Marcus, and C. Schlenker. *Solid State Commun.*, 42(6):407–410, 1982.

[75] E. Canadell. Personal Communication.

[76] G. Mihaly, A. Virosztek, and G. Gruner. *Phys. Rev. B*, 55(20):13456–13459, 1997.

[77] J.A. Wilson. *Phys. Rev. B*, 19:6456, 1979.

[78] E. Canadell, Y. Mathey, and M. H. Whangbo. *J. Am. Chem. Soc.*, 110(1):104–108, 1988.

[79] K. Stowe and F. R. Wagner. *J Solid State Chem*, 138(1):160–168, 1998.

[80] Bjerkelu.E, J. H. Fermor, and A. Kjekshus. *Acta Chem Scand*, 20(7):1836, 1966.

[81] T. Yokoya, T. Kiss, A. Chainani, S. Shin, M. Nohara, and H. Takagi. *Science*, 294(5551):2518–2520, 2001.

[82] B. Becker, N. G. Patil, S. Ramakrishnan, A. A. Menovsky, G. J. Nieuwenhuys, and J. A. Mydosh. *Phys. Rev. B*, 59(11):7266–7269, 1999.

[83] S. Takahashi, T. Sambongi, and S. Okada. *Journal De Physique*, 44(NC-3):1733–1736, 1983.

[84] K. Yamaya, M. Yoneda, S. Yasuzuka, Y. Okajima, and S. Tanda. *J. Phys.-Condes. Matter*, 14(44):10767–10770, 2002.

[85] S. Takahashi, T. Sambongi, J. W. Brill, and W. Roark. *Solid State Commun.*, 49(11):1031–1033, 1984.

[86] S. Furuseth and H. Fjellvag. *Acta Chem Scand*, 45(7):694–697, 1991.

[87] C. Felser, E. W. Finckh, H. Kleinke, F. Rocker, and W. Tremel. *J. Mater. Chem.*, 8(8):1787–1798, 1998.

[88] R. Seshadri, E. Suard, C. Felser, E. W. Finckh, A. Maignan, and W. Tremel. *J. Mater. Chem.*, 8(12):2869–2874, 1998.

[89] S. K. Srivastava and B. N. Avasthi. *J. Mater. Sci.*, 27(14):3693–3705, 1992.

[90] R. deBoer and E. H. P. Cordfunke. *J. Alloy. Compd.*, 259(1-2):115–121, 1997.

[91] S.V. Hoffmann, Ch. Sndergaard, Ch. Schultz, Z. Li, and Ph. Hofmann. *Nuclear Instruments and Methods in Physics Research Section A: Accelerators, Spectrometers, Detectors and Associated Equipment*, 523(3):441–453, 2004.

[92] T. Valla, A. V. Fedorov, P. D. Johnson, P-A. Glans, C. McGuinness, K. E. Smith, E.Y. Andrei, and H. Berger. *Phys. Rev. Lett.*, 92:086401, 2004.

[93] E. Canadell, I. E. I. Rachidi, J. P. Pouget, P. Gressier, A. Meerschaut, J. Rouxel, D. Jung, M. Evain, and M. H. Whangbo. *Inorg. Chem.*, 29(7):1401–1407, 1990.

[94] D. W. Bullett. *J Phys C Solid State*, 12(2):277–281, 1979.

[95] V. J. Emery and S. A. Kivelson. *Phys. Rev. Lett.*, 74(16):3253–3256, 1995.

[96] B. Fisher and M. Fibich. *Phys. Rev. B*, 37(6):2820–2825, 1988.

[97] A. Perucchi, Ch. Sndergaard, S. Mitrovic, M. Grioni, N. Barisic, H. Berger, L. Forro, and L. Degiorgi. *Eur. Phys. J. B*, 39:433–440, 2004.

[98] E. N. Dolgov, Y. I. Latyshev, and V. E. Minakova. *Fiz Tverd Tela+*, 26(11):3472–3474, 1984.

[99] C. G. Slough, B. Giambattista, W. W. Mcnairy, and R. V. Coleman. *J Vac Sci Technol A*, 8(1):490–494, 1990.

[100] P.A. Lee, T.M. Rice, and P.W. Anderson. *Solid State Commun.*, 14:703, 1974.

[101] L. F. Mattheiss. *Solid State Commun.*, 93(10):791–795, 1995.

[102] M. H. Whangbo, H. J. Koo, D. Dai, and A. Villesuzanne. *J Solid State Chem*, 165(2):345–358, 2002.

[103] R. A. Gardner, M. Vlasse, and A. Wold. *Am Ceram Soc Bull*, 47(4):383, 1968.

[104] M. Takano, H. Kosugi, N. Nakanishi, M. Shimada, T. Wada, and M. Koizumi. *J Phys Soc Jpn*, 43(3):1101–1102, 1977.

[105] O. Massenet, J. J. Since, J. Mercier, M. Avignon, R. Buder, V. D. Nguyen, and J. Kelber. *J Phys Chem Solids*, 40(8):573–577, 1979.

[106] K. Matsuura, T. Wada, T. Nakamizo, H. Yamauchi, and S. Tanaka. *Phys. Rev. B*, 43(16):13118–13123, 1991.

[107] T. Graf, D. Mandrus, J. M. Lawrence, J. D. Thompson, P. C. Canfield, S. W. Cheong, and L. W. Rupp. *Phys. Rev. B*, 51(4):2037–2044, 1995.

[108] G. Mihaly, I. Kezsmarki, F. Zamborszky, M. Miljak, K. Penc, P. Fazekas, H. Berger, and L. Forro. *Phys. Rev. B*, 61(12):R7831–R7834, 2000.

[109] T. Inami, K. Ohwada, H. Kimura, M. Watanabe, Y. Noda, H. Nakamura, T. Yamasaki, M. Shiga, N. Ikeda, and Y. Murakami. *Phys. Rev. B*, 66(7):–, 2002.

[110] F. Sayetat, M. Ghedira, J. Chenavas, and M. Marezio. *J Phys C Solid State*, 15(8):1627–1635, 1982.

[111] M. Ghedira, M. Anne, J. Chenavas, M. Marezio, and F. Sayetat. *J Phys C Solid State*, 19(33):6489–6503, 1986.

[112] H. Nakamura, H. Tanahashi, H. Imai, M. Shiga, K. Kojima, K. Kakurai, and M. Nishi. *J Phys Chem Solids*, 60(8-9):1137–1140, 1999.

[113] W. Higemoto, A. Koda, G. Maruta, K. Nishiyama, H. Nakamura, S. Giri, and M. Shiga. *J Phys Soc Jpn*, 71(10):2361–2364, 2002.

[114] H. Nakamura, T. Yamasaki, S. Giri, H. Imai, M. Shiga, K. Kojima, M. Nishi, K. Kakurai, and N. Metoki. *J Phys Soc Jpn*, 69(9):2763–2766, 2000.

[115] H. Kuriyaki, H. Berger, S. Nishioka, H. Kawakami, K. Hirakawa, and F. A. Lvy. *Synthetic Metals*, 71(1-3):2049–2050, 1995.

[116] I. Kezsmarki, S. Csonka, H. Berger, L. Forro, P. Fazekas, and G. Mihaly. *Phys. Rev. B*, 6308(8):art. no.–081106, 2001.

[117] M. Nakamura, A. Sekiyama, H. Namatame, A. Fujimori, H. Yoshihara, T. Ohtani, A. Misu, and M. Takano. *Phys. Rev. B*, 49(23):16191–16201, 1994.

[118] L. Forro, R. Gaal, H. Berger, P. Fazekas, K. Penc, I. Kezsmarki, and G. Mihaly. *Phys. Rev. Lett.*, 85(9):1938–1941, 2000.

[119] N. Barisic. to be published.

[120] R. Joynt. *Science*, 284(5415):777–779, 1999.

Curriculum Vitæ

Slobodan Mitrovic, a citizen of the Republic of Croatia, was born on May 11, 1975 in the Croatian capital of Zagreb. After finishing the V. Gymnasium high school in Zagreb, he pursued a degree in Physics at the Department of Physics, Faculty of Science of the University of Zagreb. He earned his B.Sc. developing a laboratory for interferometric studies of crystal growth under equilibrium conditions at the Institute of Physics, Zagreb. His diploma work, under the supervision of Dr. Zlatko Vučić, was entitled "2-D Fourier analysis refined digital optical interferometric investigations of near-equilibrium shaped cuprous-selenide monocrystals". He was awarded Rector's award for the best student project in 1997. In 2000 he started his PhD work at the Swiss Federal Institute of Technology in Lausanne (EPFL) in the group of Prof. Giorgio Margaritondo. His reasearch interests focused on the field of strongly correlated electronic systems investigated by angle-resolved photoemission spectroscopy. At the same time he was a teaching assistant for the courses of General Physics for Informatics and Chemistry students.